



Reconfigurable microwave components made using Field Programmable Microwave Substrate

Aarefa Saifee

► To cite this version:

Aarefa Saifee. Reconfigurable microwave components made using Field Programmable Microwave Substrate. Electronics. Université de Limoges, 2023. English. NNT : 2023LIMO0034 . tel-04211544

HAL Id: tel-04211544

<https://theses.hal.science/tel-04211544>

Submitted on 19 Sep 2023

HAL is a multi-disciplinary open access archive for the deposit and dissemination of scientific research documents, whether they are published or not. The documents may come from teaching and research institutions in France or abroad, or from public or private research centers.

L'archive ouverte pluridisciplinaire **HAL**, est destinée au dépôt et à la diffusion de documents scientifiques de niveau recherche, publiés ou non, émanant des établissements d'enseignement et de recherche français ou étrangers, des laboratoires publics ou privés.

University of Limoges

**ED 653 – Sciences et Ingénierie
Faculty of Sciences and Techniques – XLIM Research Institute**

A thesis submitted to University of Limoges
in partial fulfillment of the requirements of the degree of

Doctor of Philosophy

High Frequency Electronics, Photonics and Systems

Presented and defended by
Aarefa SAIFEE

On July 12, 2023

Reconfigurable Microwave Components made using Field Programmable Microwave Substrate

Thesis supervisor: Nicolas DELHOTE and Stéphane BILA

JURY:

President of jury

M. Olivier Lafond, Professor, École supérieure d'ingénieurs de Rennes

Reporters

M. Erwan Fourn, Associate Professor, HDR, INSA Rennes

M. Philippe Ferrari, Professor, HDR, TIMA

Examiner

M. Langis Roy, Professor, Ontario Tech University

Guests

M. Aurelien Perigaud, Engineer – XLIM – University of Limoges

M. Christophe Dourousseau, Enseignant à 3iL - XLIM– University of Limoges

M. Mohamed Himdi, Professeur à l'Université de Rennes – laboratoire IETR



Indeed, the completion of faith lies in seeking knowledge and acting in accordance with it.

Maulana Ali

Acknowledgements

I would like to express my sincerest gratitude to all those who have supported me throughout my PhD journey. I would like to extend a special thanks to my thesis supervisor, Dr. Stéphane Bila and Dr. Nicolas Delhote who has been an inspiration and a source of guidance and support. Their insights, encouragement, and expertise have been invaluable in shaping this work.

I would also like to thank the members of my thesis committee, for their time, expertise, and constructive feedback. Their valuable contributions have helped me to significantly improve this thesis.

I would also like to extend my appreciation to the research team, especially to Dr. Aurelien Perigaud and Dr. Christophe Duroisseau for the continuous support, their insightful advice, and their exceptional qualities as professionals and kind individuals.

I am grateful to my colleagues and friends in the MACAO team for providing a supportive and intellectually stimulating environment. A special thanks to Mrs. Marie Claude Lerouge for all the help with the administrative formalities of the University.

I would like to acknowledge to Prof. Langis Roy and Prof. Ying Wang from Ontario Tech University, Canada without whose support I would not have been able to develop this work. Thank you so much for the wonderful time I had spent there.

Finally, I would like to express my love and gratitude to my family, especially my parents, sister and brother who have supported me throughout this journey with love, encouragement, and unwavering belief in my abilities. This thesis is dedicated to them.

Thank you all for your support and encouragement.

Rights

This creation is available under a Creative Commons contract:

« **Attribution-Non Commercial-No Derivatives 4.0 International** »

online at <https://creativecommons.org/licenses/by-nc-nd/4.0/>



Table of Contents

Introduction	15
Chapter 1. Reconfigurable Microwave Devices.....	18
1.1. Introduction	18
1.2. Tunable Mechanisms.....	18
1.2.1. Ferrite and Ferroelectric	19
1.2.2. MEMS	22
1.2.3. Phase Change Materials	25
1.2.4. Varactor Diodes.....	27
1.2.5. Microfluidics Tuning.....	30
1.2.6. Summary	32
1.3. Reconfigurable Devices.....	33
1.3.1. Programmable Microwave Function Array PROMFA	33
1.3.2. Microstrip Square Patch Resonator	35
1.3.3. Reconfigurable Circuit using PCM	38
1.3.4. Programmable Bridged T-Coil Array.....	42
1.3.5. Reconfigurable Microwave Components using software.....	46
1.3.6. Filtenuator	47
1.4. Conclusion.....	49
1.5. References	51
Chapter 2. Field Programmable Microwave Substrate	57
2.1. Introduction	57
2.2. Unit Cell	58
2.3. FPMS.....	63
2.3.1. Programmable Waveguides.....	64
2.3.2. FPMS Robustness.....	66
2.3.3. FPMS Filter	67
2.4. FPMS Equivalent Model Optimization	69
2.4.1. ADS-MATLAB Interface.....	70
2.4.2. MATLAB Graphical Interface	72
2.4.3. Optimization Algorithms.....	73
2.5. FPMS Devices.....	75
2.5.1. 3-Port Power Divider.....	75
2.5.2. Phase Shifter.....	77
2.5.3. Tunable Notch	78
2.6. Conclusion.....	79
2.7. References	81
Chapter 3. Optimized FPMS Devices	83
3.1. Introduction	83
3.2. Live Optimization on FPMS	84
3.2.1. MATLAB Graphical Interface	85
3.2.2. Coarse and Fine Optimization	86

3.3. Power Divider.....	89
3.3.1. Even Power Distribution	90
3.3.2. Balanced Power Distribution.....	91
3.3.3. Unbalanced Power Distribution	93
3.4. Tunable Notch	95
3.5. Mixing Signal Routing and Other Functions.....	96
3.5.1. Switch.....	96
3.5.2. Signal Routing and Phase Shifting	98
3.5.3. Signal Routing and Programmable Attenuator.....	104
3.6. Discussions on FPMS.....	106
3.7. Conclusion.....	107
3.8. References	109
 Chapter 4. FPMS 2.0	 113
4.1. Introduction	113
4.2. Unit cell of FPMS 2.0.....	113
4.3. FPMS 2.0.....	117
4.4. Different Microwave Functions using FPMS 2.0.....	120
4.5. New Components from FPMS 2.0	125
4.6. Comparison of FPMS 2.0 with previous devices	131
4.7. Conclusion.....	132
4.8. References	134
 Conclusion.....	 137
 Appendices	 140

List of Figures

Figure 1.1: Cross section of the two-layered microstrip structure for resonator	19
Figure 1.2 : Microstripline side-coupled 25Ω -ring resonator.....	20
Figure 1.3 : Measured results for ring resonator	21
Figure 1.4 : . Ka-Band tunable bandpass filters using ferroelectric capacitors	22
Figure 1.5 : Tunable capacitive-post loaded resonant cavity	23
Figure 1.6 : Measured reflection coefficient with different DC bias.....	23
Figure 1.7 : Schematic view of a third-order bandpass filter	24
Figure 1.8 : 3D model of the integrated MEMS filter	24
Figure 1.9 : Measured insertion loss and return loss of the MEMS filter	25
Figure 1.10 : Cross section of phase change switch.....	26
Figure 1.11 : Insertion loss (on state) and isolation (off state) of PCM switch.....	26
Figure 1.12 : CPW filter layout	26
Figure 1.13 : Simulated filter response in the On and Off states.....	27
Figure 1.14 : Equivalent circuit of varactor diode.....	28
Figure 1.15 : Proposed SMT SISL	29
Figure 1.16 : Tunable filter based on SMT SISL technolgy	29
Figure 1.17 : Measured results of tunable filter based on SMT SISL technolgy	29
Figure 1.18 : Two pole bandpass filter loaded by varactor	30
Figure 1.19 : Liquid-Metal based Tunable Bandpass Filter	31
Figure 1.20 : Measured reults of Liquid-Metal based Tunable Bandpass Filter	32
Figure 1.21 : Block diagram of the PROMFA	34
Figure 1.22 : Block diagram of a single PROMFA cell	34
Figure 1.23 : Block diagram of power splitter	35
Figure 1.24 : Structure of the BBE.....	36
Figure 1.25 : Hard-wired devices operating in (a) filter mode and (b) antenna mode	36
Figure 1.26 : S- parameters for (a) filter mode and (b) antenna mode	37
Figure 1.27 : Single BBE incorporating p-i-n diode switches.....	37
Figure 1.28 : S- parameters for (a) filter mode and (b) antenna mode	38
Figure 1.29 : VO_2 film on a microwave substrate with metallic and insulating layers	39
Figure 1.30 : Unit-cell of a CPW transmission line comprising a VO_2 film	39
Figure 1.31 : S-parameters for CPW structure	40
Figure 1.32 : Dipoles: metal and VO_2	41

Figure 1.33 : Simulated S-parameters of metal and VO ₂ dipole	42
Figure 1.34 : Circuit structure of programmable bridged-T coil array	43
Figure 1.35 : Fabricated chip	43
Figure 1.36 : Power Divider configuration and its S-parameters	44
Figure 1.37 : Bandstop filter configuration and its S-parameters	45
Figure 1.38 : Bandpass filter configuration and its S-parameters	46
Figure 1.39 : Functional Programmable Microwave Component (FPMC)	47
Figure 1.40 : Measured and EM simulated results for the FPMC	48
Figure 1.41 : Filtenuator schematic and S-parameters	48
Figure 2.1 : Schematic of a Unit Cell of FPMS	60
Figure 2.2 : Simulated effective dielectric constant of unit cell	61
Figure 2.3 : Simulated effective dielectric loss tangent of unit cell	61
Figure 2.4 : Simulated effective magnetic constant of unit cell	61
Figure 2.5 : Simulated effective magnetic loss tangent of unit cell	62
Figure 2.6 : Simulated effective properties of unit cell when biased at 0 V	62
Figure 2.7 : HFSS model of FPMS	63
Figure 2.8 : FPMS circuit board	64
Figure 2.9 : FPMS waveguide	65
Figure 2.10 : Measurement results of six cells wide FPMS waveguide	65
Figure 2.11 : Measured insertion loss for different width and biasing voltage of waveguide	65
Figure 2.12 : Random failure in FPMS waveguide	66
Figure 2.13 : Measured Insertion loss in case of random failures	67
Figure 2.14 : FPMS waveguide band pass filter	68
Figure 2.15 : Measured results of the FPMS waveguide bandpass filter	68
Figure 2.16 : Measurement results of tunable center frequency	69
Figure 2.17 : Measurement results of tunable bandwidth	69
Figure 2.18 : Different blocks of ADS/MATLAB Interface	71
Figure 2.19 : Simulated Power Divider with equal power distribution	76
Figure 2.20 : Simulated Power Divider with 1:2 dividing ratio	77
Figure 2.21 : Simulated Phase Shifter	78
Figure 2.22 : Simulated Tunable notch	79
Figure 3.1 : Measurement set-up for the Live Optimization	85
Figure 3.2 : Steps for live optimization on FPMS	85
Figure 3.3 : 16x16 FPMS matrix converted into 8x8 FPMS matrix	86

Figure 3.4 : Coarse optimization: Waveguide	87
Figure 3.5 : Coarse optimization: Power divider.....	88
Figure 3.6 : Fine optimization: Power divider.....	89
Figure 3.7 : Initial configuration for the 3 ports power divider.....	90
Figure 3.8 : Even power distribution.....	91
Figure 3.9 : Balanced power distribution with same phase.....	92
Figure 3.10 : Balanced power distribution with distinct phase	93
Figure 3.11 : Unequal power distribution.....	94
Figure 3.12 : Straight waveguide based tunable notch.....	95
Figure 3.13 : Curved waveguide based tunable notch.....	96
Figure 3.14 : Switch	97
Figure 3.15 : Phase shifter obtained by optimization for straight waveguide	99
Figure 3.16 : Phase shifter obtained by optimization for bended waveguide.....	100
Figure 3.17 : Insertion loss for the optimization based phase shifter	100
Figure 3.18 : Insertion loss for the variations in voltage based phase shifter.....	101
Figure 3.19 : Phase shifter obtained by changing the bias for straight waveguide	102
Figure 3.20 : Phase shifter obtained by changing the bias for bended waveguide	103
Figure 3.21 : Straight waveguide based programmable attenuator	104
Figure 3.22 : Bended waveguide based programmable attenuator.....	105
Figure 3.23 : Isolation v/s number of columns of OFF unit cells.....	105
Figure 4.1 : New Unit Cell design.....	114
Figure 4.2 : Characteristics of varactor diode	115
Figure 4.3: Extracted dielectric and magnetic constant for different capacitance values.....	116
Figure 4.4 : Six cells wide waveguide and simulated S-parameters	117
Figure 4.5 : CST Model of FPMS2.0	117
Figure 4.6 : Bended waveguide.....	118
Figure 4.7 : E-field distribution for FPMS 2.0 straight waveguide.....	119
Figure 4.8 : CST and ADS results comparison	119
Figure 4.9 : Straight waveguide with different widths	120
Figure 4.10 : Phase Shifter	123
Figure 4.11 : Straight waveguide based attenuator	124
Figure 4.12 : Two bended waveguide at the same time	125
Figure 4.13 : Band stop filter with one pole.....	126
Figure 4.14 : Band stop filter with two poles	127

Figure 4.15 : Band stop filter with two poles and increased reflectivity	129
Figure 4.16 : Band stop filter with three poles	129
Figure 4.17 : 4-Port Power Divider initial configuration	130
Figure 4.18 : 4-Port Power Divider manually optimized configuration.....	130

List of Tables

Table 1.1: Pros and Cons of different tuning methods	32
Table 1.2: Reconfigurable Multi-Functional Microwave Components.....	49
Table 2.1: Comparison of different optimization algorithms	75
Table 3.1: Performance of phase shifters using FPMS	103
Table 3.2: Reconfigurable Multi-Functional Microwave Components.....	107
Table 4.1: Power divider configuration and simulated results	122
Table 4.2: Band stop filter with two poles	128
Table 4.3: Reconfigurable Multi-Functional Microwave Components.....	132

Introduction

Billions of individuals can now access the Internet, take advantage of the modern digital economy, and can use mobile phones anywhere in the world largely due to wireless communications. Wireless communication is increasingly vital to almost every sector of the economy, from banking and agriculture to transportation and healthcare [1]. 5G, artificial intelligence, and the Internet of Things are some of the effective new technologies that rely on strong wireless communication networks. 5G will enable the flow of a huge amount of data much faster, reliably connecting an extremely large number of devices and processing very high volumes of data with minimal delay. It is expected to support applications such as smart homes and buildings, smart cities, 3D video, work and play in the cloud, remote medical surgery, virtual and augmented reality, and massive machine-to-machine communications for industry automation and self-driving cars. It holds immense promises to transform lives at a pace and scale that has never been seen before.

RF or microwave signals, typically in the UHF to millimeter wave frequency range, provide the basis for the majority of existing wireless systems. Most of the wireless systems currently operates at frequencies ranging from roughly 800 MHz to a few gigahertz due to spectrum crowding and the requirement for increased data rates [2]. Wide bandwidths are a feature of RF and microwave signals, and they also have the benefit of having some degree of penetration through objects like buildings and cars as well as through fog, dust, and foliage. The theoretical work of Maxwell, the experimental validation of the propagation of electromagnetic waves by Hertz, and the practical development of radio techniques and systems by Tesla, Marconi, and others in the early 20th century are the historical foundations of wireless communication using RF energy.

Broadcast radio, cellular phone and networking systems, Direct Broadcast Satellite television service, wireless local area networks (WLANs), paging systems, Global Positioning System (GPS) service, and radio frequency identification (RFID) systems are all examples of wireless systems in use today.

As the world moves towards 5G, the major technological change that needs to be dealt with is the use of higher frequency bands that are ultimately based on the size of components used in the communication networks. Additionally, a large number of connected devices requires more hardware components. One way to handle this issue is the use of reconfigurable devices that can be dynamically programmed to perform different microwave functions with a single hardware component. It is similar to Field Programmable Gate Arrays (FPGA) in digital circuits. This type of programmable component

can also be used in telecommunications satellites or Unmanned Aerial Vehicles for example, where it can be reconfigured on the fly. In this thesis, we will study the different methods in the development of programmable microwave components (reconfigurable phase shifter, power divider etc.) using a single device. In particular, the concept of Field Programmable Microwave Substrate (FPMS) is demonstrated here in details, which is one of the most efficient methods to realize fully reconfigurable microwave devices. This work is mostly focused on developing the specific optimization algorithms in order to obtain microwave function with the best performance achievable using this FPMS.

The research reported in this thesis is supported by the French national research agency (ANR) and the Natural Sciences and Engineering Research Council of Canada (NSERC) through the Strategic Partnerships international project RWC_FPMS. This is an international collaboration between four academic partners, XLIM Research institute (University of Limoges, France), IETR (University of Rennes, France), Ontario Tech University (Canada) and Carleton University (Canada) with the support of the Orbcomm company.

In this project, the XLIM institute is in charge of developing an algorithm based optimization strategy to optimize the different reconfigurable functions we can create with the FPMS. This thesis is done within a strong collaboration scheme with the Ontario Tech and the IETR regarding the use of current generation of the FPMS (generation 1) and the newly developed one (generation 2) during this project. This work will be focused on the signal routing capabilities of these devices.

The thesis is organized into five chapters which are summarized below:

Chapter 1 presents several methods that have been previously discussed in the literature to realize reconfigurable devices.

Chapter 2 details the whole concept behind the Field Programmable Microwave Substrate and presents the optimization techniques that are developed and have been applied to equivalent model of FPMS.

Chapter 3 presents the measurement results of all the microwave functions that can be achieved by combining the optimization algorithms to the FPMS in real-time.

Chapter 4 presents preliminary test on the next generation of FPMS with higher frequency range and better performances.

Conclusion highlights all the important contributions of this thesis. It also elaborates on future perspectives related to the research subject of this thesis.

Chapter 1.

Reconfigurable Microwave Devices

1.1 Introduction

The microwave circuits are mainly designed for a specific function according to the needs but as mentioned earlier modern wireless communication requires devices whose functionality can be changed based on different requirements. A reconfigurable microwave device can be programmed to perform different microwave functions at the same time according to the specifications set by an individual such as filters, phase shifters, amplifiers, antennas etc. The concept is similar to that of a FPGA but it's for analog signals in the microwave range. The concept of realizing different microwave functions using only a single device has attracted tremendous interest due to its several benefits. Firstly, it reduces time and cost in development of different microwave components because a single device can address many specifications depending on the use case. We can replace different RF devices with one that covers different needs, for example one single filter that can update its frequency behavior (central frequency, bandwidth). These devices mitigate the losses in case of component failure by replacing them on the fly. There is a wide range of potential applications for reconfigurable microwave devices in military equipment and space satellite communication systems. This chapter presents different methods that have been developed so far for realizing programmable microwave circuits.

1.2 Tunable Mechanisms

To achieve reconfigurable microwave circuits, numerous tunable means have been studied over the years. Semiconductors, ferroelectric materials, or mechanically altering the circuit with microelectromechanical systems (MEMS) can all be used to create reconfigurable circuits. The most often utilized components to achieve configurability are semiconductor switches and varactors since they can be affordably integrated on the same chip as the RF/microwave circuitry. This section discusses a few methods for realizing tunability. Reconfigurable filters will be used as examples here.

1.2.1 Ferrite and Ferroelectric

Ferroelectric or ferrite-based thin films can be used into traditional microstrip circuits to achieve frequency and phase agility in microwave circuits [3]–[6]. There have been experiments with brand-new superconductor-ferrite circulators with magnetic confinement [4]. Ferrites have a magnetically controllable permeability. The use of ferrite thin films, however, need extra coils and frequently high currents for tunability.

On the other hand, the nonlinear DC electric-field dependence of their relative dielectric constant for ferroelectric thin films makes them suited for frequency-agile microwave components. The change in the ferroelectric's relative dielectric constant under an external DC field relative to that at no field determines the film's tunability. Some of the most common ferroelectric thin films currently being researched for frequency-agile parts and circuits are strontium titanate (STO) and barium strontium titanate (BSTO).

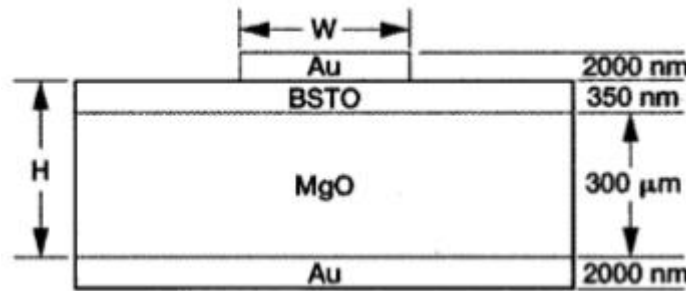


Fig. 1.1. Cross section of the two-layered microstrip structure for resonator [7].

A ring resonator configurations has been explored using Au/STO/LAO conductor/ferroelectric/dielectric(CFD) structures in the Ku and K band frequencies in [7]. Figure 1.1 displays the cross section of a two-layered microstrip structure that is employed in resonator. The microstrip structure has been modified to include a dielectric substrate (usually lanthanum aluminate (LAO) or magnesium oxide (MgO) and with a thickness of approximately $254\ \mu\text{m}$), a ferroelectric thin-film layer (with a thickness that ranges from 300 to 2000 nm depending on the application), a $2\ \mu\text{m}$ - thick gold or 350-nm-thick YBCO thin film for the top conductor, and a $2\ \mu\text{m}$ -thick gold ground plane. The frequency or phase tunability and overall insertion loss of the circuit are highly influenced by the dielectric properties of the ferroelectric thin film and the thickness of the ferroelectric film.

Microstrip side-coupled ring resonators were utilized in this research, as depicted in Fig. 1.2. To prevent moding issues, two ring resonators were designed for third-order resonance at 20 GHz, with characteristic impedances of 50Ω and 25Ω and no ferroelectric layer. These "band-stop" resonators display sharp resonances with unloaded Q as high as 15000 under suitable biasing schemes. The resonant frequency has been adjusted to surpass 1 GHz. The sharpness of the resonance was maintained while achieving significant tunability, ranging from 16.6 GHz at zero bias up to nearly 17.8 GHz at a dc voltage of 400 V, as demonstrated in Fig.1.3. With the appropriate biasing scheme and adjustment of two independent dc voltages, coupling can be optimized and resonance sharpened while maintaining significant tunabilities, as depicted in Fig. 1.3. The different biasing schemes modifying the dc voltage V_R primarily affects the ϵ_{eff} of the ring and its resonant frequency.

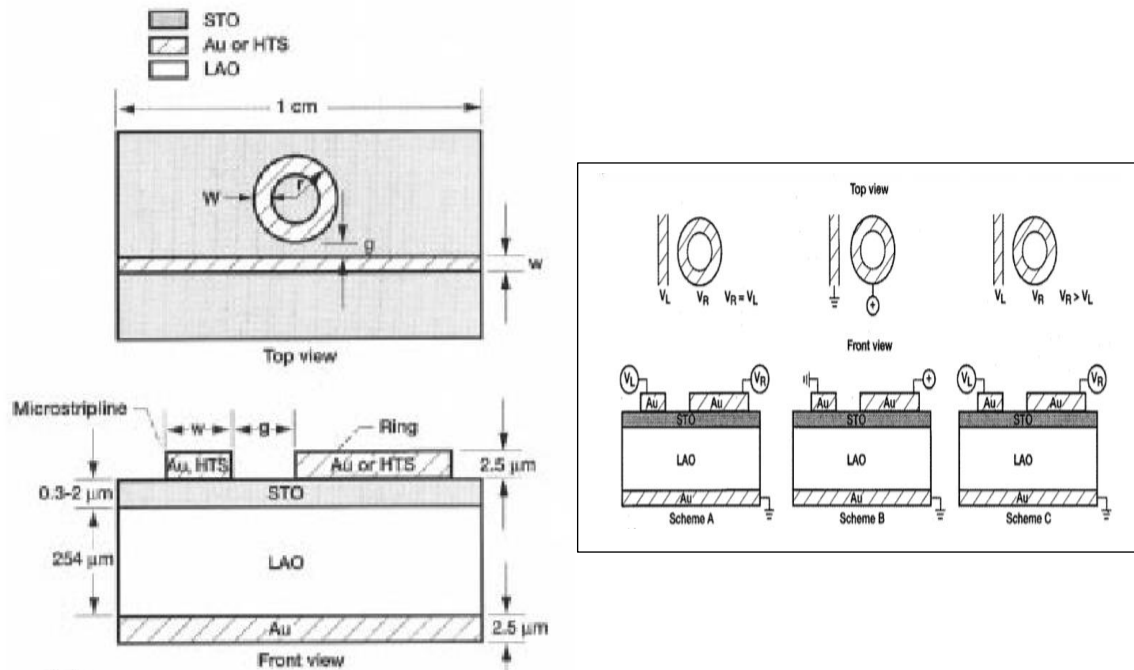


Fig. 1.2. Microstrip line side-coupled 25Ω -ring resonator. $W = 406\mu\text{m}$, $w = 89\mu\text{m}$, $r = 1694\mu\text{m}$, and $g = 25\mu\text{m}$. with the various biasing schemes [7].

By altering the voltage difference, the coupling of the ring to the line can be controlled, enabling tuning of the resonator from over coupled to critical to under coupled. Biasing scheme A (Fig. 1.2), which provides maximum coupling to the ring, resulted in higher frequency tunability but over-coupled resonances with low- values. Biasing scheme B allowed for tuning of a critical coupling and a sharp resonance but only within a narrow frequency range. Through simultaneous adjustment of both and (bias scheme C), the coupling can be optimized, and the third-order resonance can be sharpened while maintaining significant frequency tunability. The magnitude of for this differential biasing scheme can be observed in Fig. 1.3.

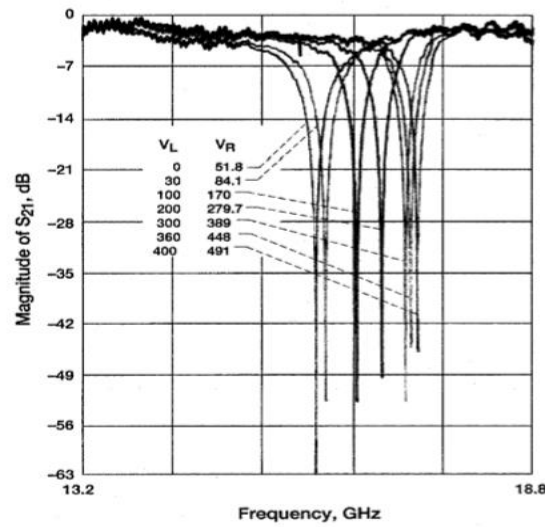


Fig. 1.3. Measured results for ring resonator [7].

Various papers highlight the application of ferroelectric tunable band pass filters. For example, in [8], a second-order quasi-elliptic ferroelectric band pass filter for Ka band is presented. The filter is based on epitaxial BSR on sapphire technology and employs coupled-line coplanar waveguide (CPW) to achieve compactness and low loss. The filter consists of four CPW quarter-wavelength resonators, each loaded with a barium strontium titanate (BST) tunable capacitor. The capacitance value changes with the application of a tuning voltage to the ferroelectric material, resulting in a frequency response change. The filter is capable of frequency tuning of 2.4 GHz (33.6-36 GHz) at biasing levels below 30 V with a loss of 6.2-7.4 dB. Figure 1.4 illustrates the filter's topology and frequency response.

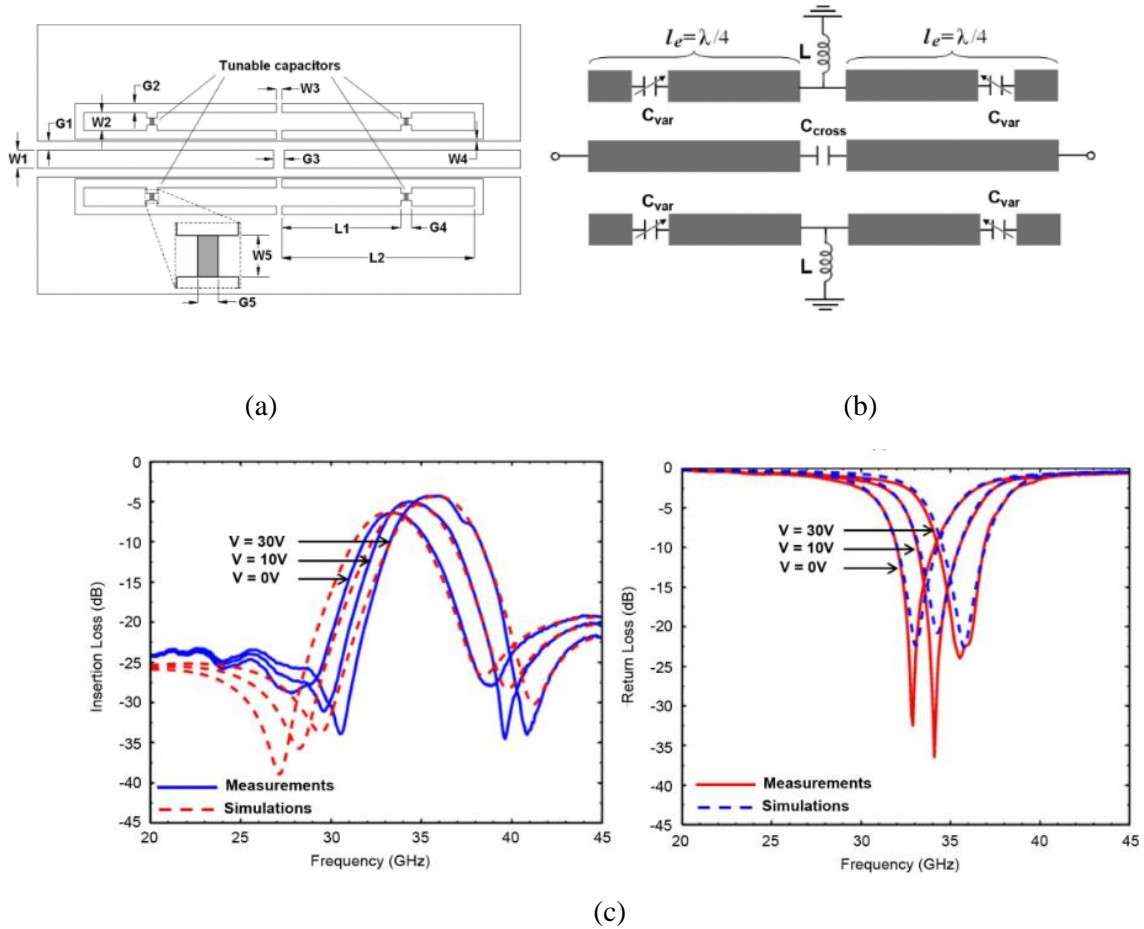


Fig. 1.4. Ka-Band tunable band pass filters using ferroelectric capacitors (a) Layout, (b) Circuit and (c) Measurement results [8].

1.2.2 Micro-electromechanical systems (MEMS)

Since the performance of a microwave circuit is closely related to its physical parameters, altering a microwave circuit mechanically is a useful tool. Although physically altering the circuit can produce a very wide range of configurability, this method is prone to wear-and-tear issues. MEMS enable the configuration of microwave circuits by the actuation of typically metallic components. Although some MEMS devices use electro-thermal activation, the majority of MEMS devices are activated utilizing an electrical bias. One such system [9] uses an interdigitated beam for capacitance, where one beam may be moved to alter the gap using electro thermal actuators. Due to its low loss and high power handling capacity, MEMS switches [10–14] are employed in a range of reconfigurable microwave circuits.

In reconfigurable microwave circuits, MEMS are typically utilized to replace semiconductor switches and varactors. The capacitive-post loaded resonant cavity in Figure 1.5 [15] is one such device that achieves significant tunability. In the figure, above the post (orange), there is a thin insulator (red), followed by a thin coating of gold (yellow) on silicon (grey) for the diaphragm. After that there is a gap that is used for the actuation. The strong capacitive effect created

in the gap is significantly altered when changing its dimension, even with very small variation less than $1\mu\text{m}$. A dielectric layer follows the gap, and an electrode layer made of silicon is placed on top. The cavity's resonance frequency ranges from 6.1-24.4GHz (Figure 1.6) that is achieved by activating gold diaphragm from $0.5\text{--}15\mu\text{m}$ above the post.

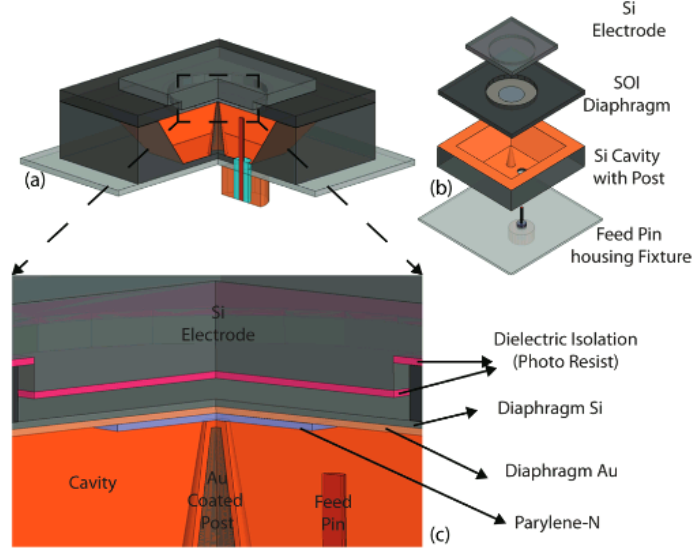


Fig. 1.5. (a) Tunable capacitive-post loaded resonant cavity and (b) parts of assembled resonator [15].

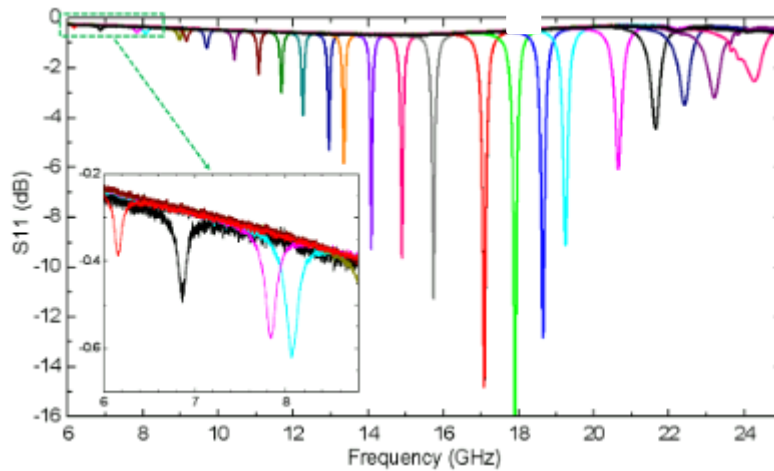


Fig. 1.6. Measured reflection coefficient with different DC bias [15].

A high performance MEMS filter has been discussed in [16]. The initial approach to creating an Integrated MEMS Filter is founded on a MEMS surface micromachining technology. This technology utilizes three metal, one dielectric, and two polymer sacrificial layers, which can facilitate the integration of various passive components [17]. With the aid of this technology, a third-order Chebyshev filter is constructed (as demonstrated in Fig. 1.7 (a)). The filter utilizes mutual inductive coupling and inductive matching, which exhibit wideband frequency matching, thus not required to tune while tuning the filter.

To attain wide frequency tuning, capacitors with a large-value and wide-tuning range are needed. To achieve this, a network of three capacitive switches and one continuously tuned capacitor (varactor) is integrated into each resonator tank (as depicted in Fig. 1.7 (b)). The varactors and capacitive switches are tuned to an equal final state value to ensure continuous tuning of the center frequency. A dual-gap configuration is used for the varactors to overcome the pull-in limitation and increase the tuning range, with an actuation to sense gap ratio of 4:1 [18]. All other capacitive switches in the bank are similarly designed, but the gap ratio is reduced to improve linearity and ease of tuning. The 3D model of the filter used in simulations is shown in Fig. 1.8 (a), and the electromagnetic simulation result using ANSYS HFSS is demonstrated in Fig. 1.8 (b). The simulations show that all tuned states of the filter exhibit an insertion loss of less than 4 dB, bandwidth of 13~15%, out-of-band rejection of better than 40 dB.

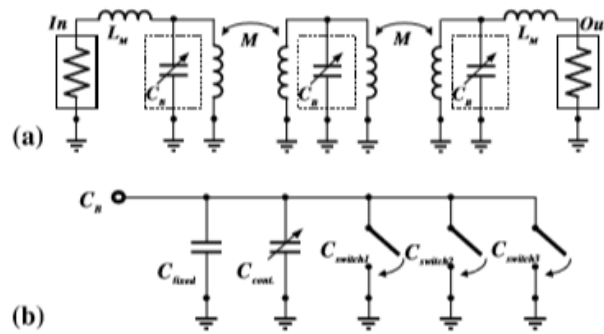


Fig. 1.7. (a) Schematic view of a third-order bandpass filter, having three tunable capacitor banks. (b) Detail composition of each tunable capacitor bank [16].

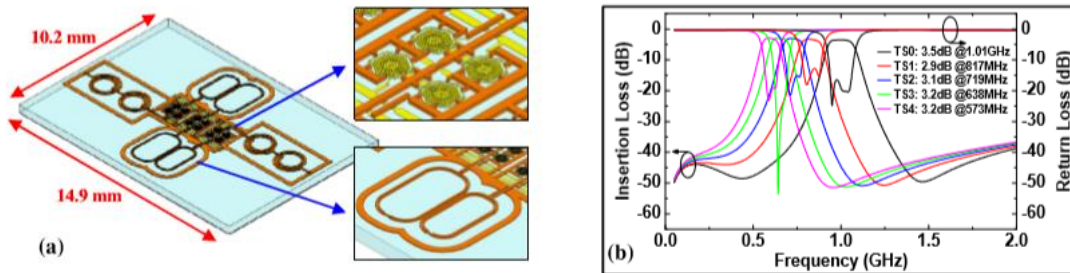


Fig. 1.8. (a) A 3D model of the integrated MEMS filter. (b) HFSS simulation results of the filter at five tuned states [16].

The measured insertion loss and return loss of the MEMS tunable filter are illustrated in Figure 1.9. The insertion loss varies from 3.0 dB to 3.6 dB at different tuned states, while retaining a consistent percentage bandwidth of approximately 13%. Additionally, the out-of-band rejection surpasses 30 dB. The group delay is also measured to be less than 10 ns. The tuning speed of the MEMS filter is between 40 μ s to 80 μ s, depending on the applied tuning bias.

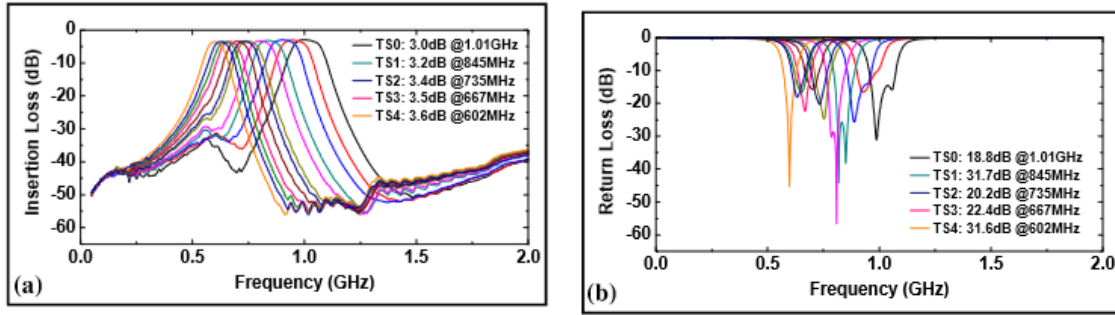


Fig. 1.9. Measured (a) insertion loss and (b) return loss of the MEMS filter at various tuned states [16].

1.2.3 Phase Change Materials

Phase change materials can change phases reversibly between insulating and conductive phases, which results into conductivity changes of several magnitude. The use of optical, electrical, stress, and thermal control signals has been illustrated for phase transitions. Vanadium dioxide (VO_2) is the most commonly used phase change material. A switch that was recently demonstrated that used VO_2 had a figure of merit less than 15fs. A CPW line with a 320nm gap and 200nm thick VO_2 deposited in the gap is used to implement the switch. The switch has a COFF of 7.7fF and a RON of 2Ω . The study demonstrates that the switch can also be electrically activated by passing a 20 mA current between its two terminals [19].

Another phase change material (PCM) that may be thermally altered from an amorphous to crystalline state, changing from being an insulator to a conductor, is germanium telluride.

Different temperature profiles must be provided to the material in order to switch it between the amorphous and crystalline states. This is often done using a micro heater that is installed nearby the phase transition material. The material must be immediately heated to 725°C , melted, and then fast quenched in order to transition to the amorphous phase (insulating). It takes a material to transition from the crystalline phase (conducting) at a temperature higher than 190°C than at its melting point. In comparison to transitioning to the amorphous state, this temperature is applied for a longer period of time and ramped down gradually. For one switch, the switch's RF power handling capacity is 3.1W, and turning it on or off needs delivering 0.5W or 4W for 1.5s or 30ns respectively [20]. One manufactured switch has $\text{RON} = 0.9\Omega$ and $\text{COFF} = 14.1\text{fF}$, with figure of merit 13fs [21]. The implementation of this switch and the measured results are depicted in Fig 1.10 and Fig 1.11 [20]. The PCM is $30\mu\text{m}$ wide and $0.9\mu\text{m}$ long.

In recent years, PCM switches for microwave applications have advanced significantly and have proven to have outstanding qualities for usage in communication systems [20–30]. The four approaches suggested in [31–34] can be used to regulate the phase transition of vanadium dioxide.

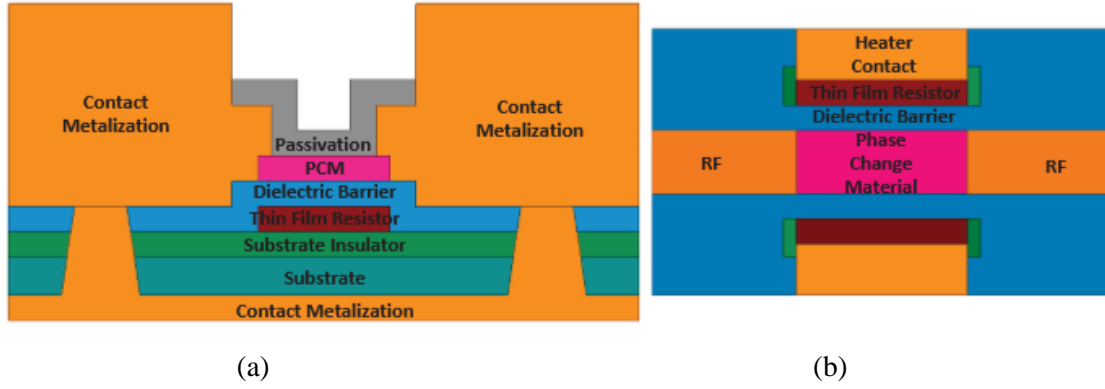


Fig 1.10. (a) Cross section of phase change switch and (b) top view shown [20].

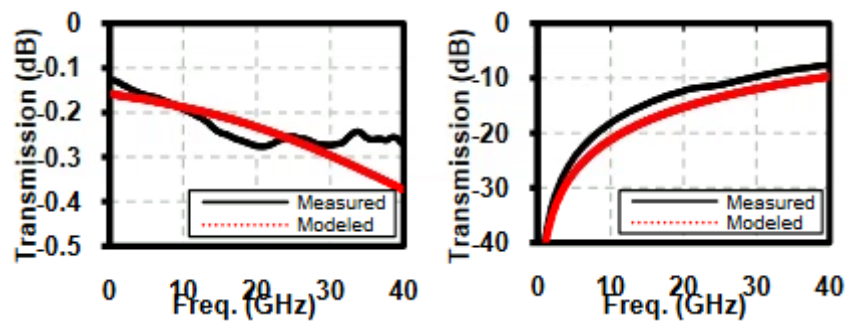


Fig 1.11. (a) Insertion loss (on state) and (b) isolation (off state) [20].

A new type of tunable filter that uses bi-stable Phase Change Material (PCM) RF switches to adjust its center frequency between 5.95 and 6.8 GHz is presented in [35]. The filter is a 1 GHz band pass filter with insertion loss between 4.5 and 5.5 dB. The bias circuit is integrated into the filter resonator to minimize any loss attributed to it. This type of tunable filter shows promise for its ability to switch frequencies and its low insertion loss.

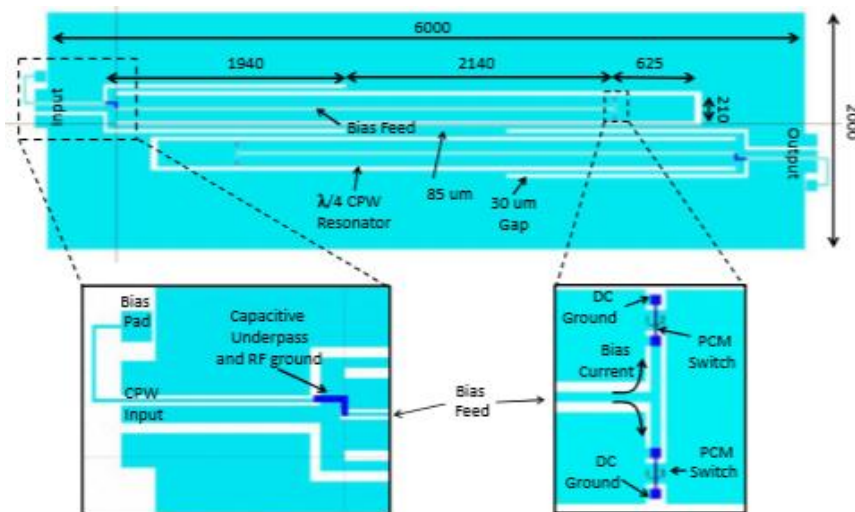


Fig. 1.12. CPW filter layout [35].

Figure 1.12 illustrates a filter structure with two poles, which comprises two coupled quarter-wavelength coplanar waveguide resonators, fed with CPW transmission lines. The filter can be tuned using PCM switches by connecting or disconnecting a short transmission line at the end of each resonator. This straightforward tuning system allows the filter's center frequency to be shifted between two specific values. The filter dimensions have been optimized for operation at 5.9 GHz and 6.8 GHz, with a 1 GHz 3 dB bandwidth and minimal insertion loss as depicted in Figure 1.13.

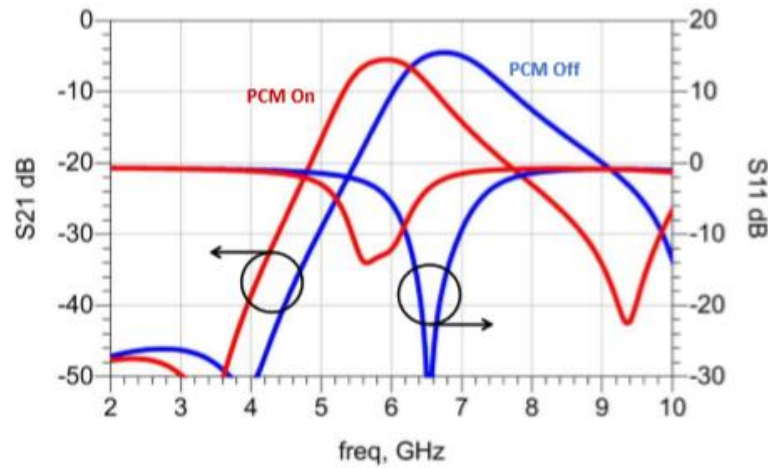


Fig. 1.13. Simulated filter response in the On and Off states [35].

The simulated insertion loss is 5.5 dB in the on-state, with a center frequency of 5.95 GHz and 4.5 dB at 6.8 GHz. Return loss are better than 20 dB in the Off-state and better than 13 dB for the four switches in the On-state.

1.2.4 Varactor Diodes

One of the simplest and most popular options for making tunable components is the varactor diode. Semiconductor varactor diodes are frequently employed in situations where a voltage-controlled variable capacitance is required in the electronic industry.

In reverse bias, a varactor diode is a P-N junction diode, meaning that no current flows. According to the amount of reverse bias used, the capacitance and series resistance of the diode alter in value. The applied bias voltage alters the thickness of the depletion zone and thus changes the capacitance values from tenth to hundreds of pF. This sort of diode's capacity to modify capacitance is extremely helpful for changing the phase of an electrical circuit or the resonance frequency of a device like a filter. Figure 1.14 shows an equivalent circuit of varactor diode [36].

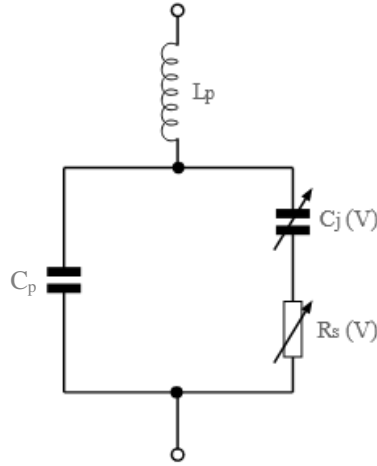


Fig. 1.14. Equivalent circuit of varactor diode [36]

The different components of varactor diode are as follows:

- $C_j(V)$: This varactor diode component indicates the real variable junction capacitance, which is a critical component.
- $R_s(V)$: The series resistance inside the diode varies depending on the applied voltage.
- C_p : This circuit component represents parasitic capacitance, which primarily results from capacitance surrounding the fundamental diode junction. This is facilitated by the package's internal wiring.
- L_p : The binding wires inside the varactor diode package are mostly responsible for this series inductance. Even its value is relatively small, high frequency RF circuits will still be able to detect it.

Given that the diode operates in reverse bias, the series resistance from the diode's leads is insignificant and the capacitance levels are quite low.

The study in [37] presents an innovative approach to surface mount suspended integrated strip-line (SISL) components, along with the construction of a surface-mount technology (SMT) thru-line to validate the method's feasibility. The proposed SMT SISL design is shown in Figure 1.15. Then, a SMT SISL technology-based S-band band pass filter (BPF) that can be continuously tuned using varactor diodes has been demonstrated. The varactor diodes are reverse-biased using direct current (DC) lines that are continuously adjustable and are fed to the component on a carrier board, along with the input/output transmission lines for radio frequency (RF). The castellated vias transition the DC lines and RF input/output transmission lines to the SISL component layer. This results in a compact solution that serves as the basis for future designs of passive components. The tunable band pass filter based on SMT SISL technology and its measured results are shown in Figure 1.16 and Figure 1.17 respectively.

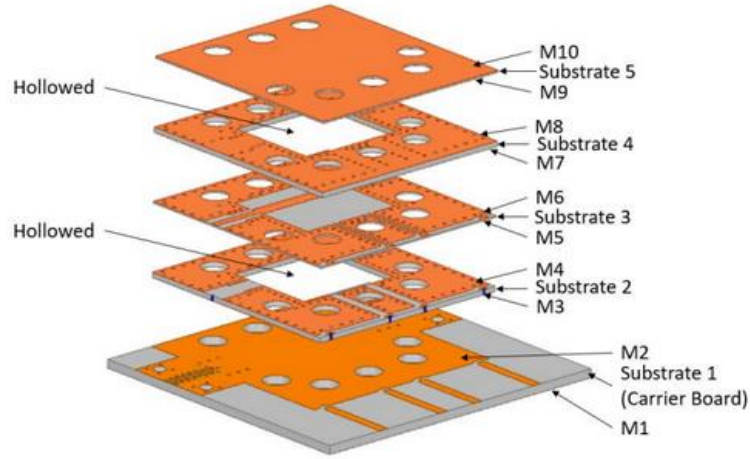
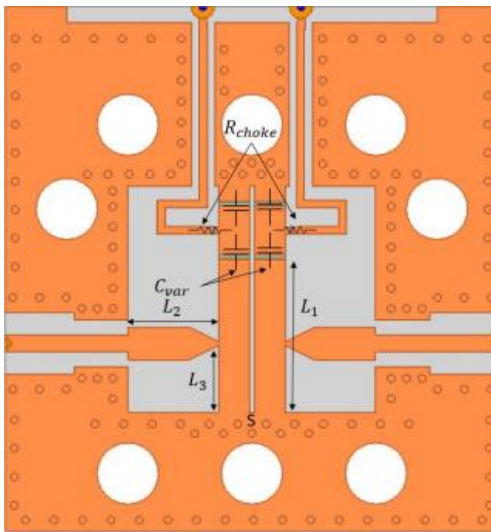
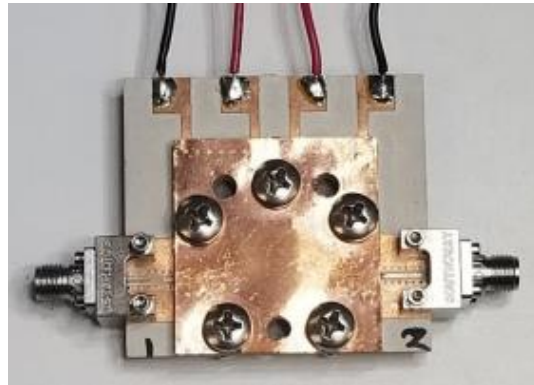


Fig. 1.15. Proposed SMT SISL [37].

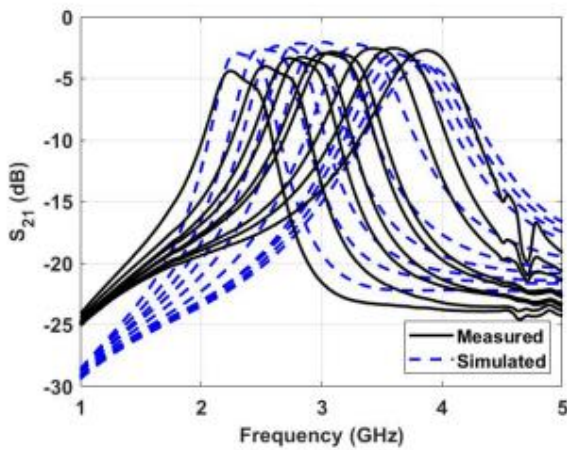


(a)

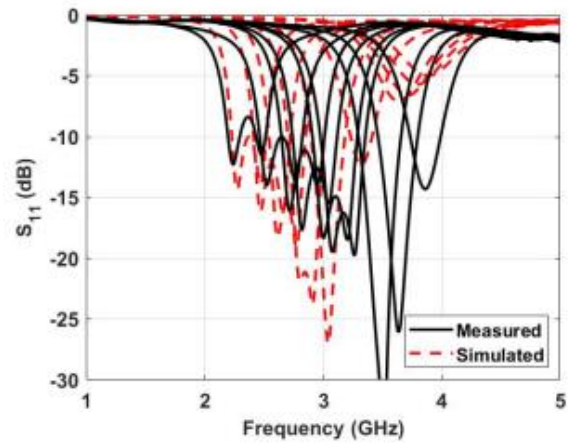


(b)

Fig. 1.16. Tunable filter. (a) Top view and (b) Fabricated filter [37].



(a)



(b)

Fig. 1.17. Measured results of the tunable SMT BPF. (a) Insertion loss. (b) Return loss [37].

An example of this concept can also be found in [38], where a metallic post is inserted into a cylindrical cavity to form an RLC resonator. A circular pattern is then etched onto the top metallized surface of the structure, creating a gap that is loaded with a varactor to modify the effective capacitance and resonance frequency of the system as shown in Figure 1.18. Various elements with changing capacitances can be used in this design. The results demonstrate a 2-pole filter with a tuning range between 0.5 to 1.1 GHz, insertion loss ranging from 4.46-1.67 dB, and a return loss up to 27.8 dB. The quality factor varies from 84 to 206. An enhancement is proposed in [39], where control of the couplings is integrated in a similar manner to the previous article, providing a continuous control of the resonance frequency and bandwidth. In this case, the cylindrical cavity is achieved through electrical vias, creating a substrate integrated waveguide (SIW) resonator. This structure, in conjunction with varactors, is frequently used to create high Q reconfigurable filters. However, varactor diodes, despite their attractive features, require bias circuits that may limit the bandwidth and Q-factor performance.

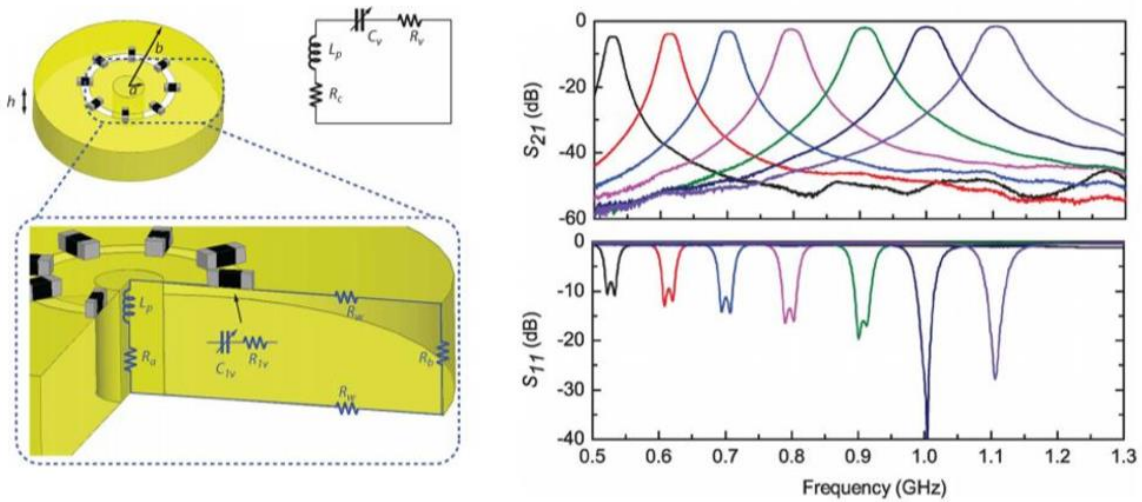


Fig. 1.18. Two-pole band pass filter loaded by varactors [38].

1.2.5 Microfluidics Tuning

The concept of microfluidics involves the movement of either a liquid dielectric or conductive material into or out of a section of a microwave circuit. Typically, microfluidics is employed for moving a liquid metal around in microwave circuits. The recent introduction of a non-toxic liquid metal called Galinstan has triggered extensive exploration into reconfigurable liquid metal microwave circuits. According to reports, Galinstan possesses the following characteristics [40-42] :

- A eutectic mixture of gallium, indium, and tin.
- A conductivity of 2.3×10^6 S/m.
- The ability to remain in liquid form within a temperature range of -19 to 1300°C.

Galinstan is highly reactive and can oxidize in the presence of as little as 1ppm of oxygen. However, the oxide formed can be reduced by immersing it in an electrolyte solution such as HCl or NaOH. Furthermore, Galinstan readily forms alloys with a wide range of metals and has a high surface tension that causes it to form into small droplets. There are four ways to move Galinstan: fluidic pumping [43], electrowetting on dielectric (EWOD) [41], continuous electrowetting (CEW) [42], and electrochemically controlled capillarity (ECC) [44].

A substrate integrated waveguide filter that is reconfigurable by pumping Galinstan is demonstrated in [45]. The filter employs four hollow vias that can be filled or emptied using a syringe for reconfiguration. To dissolve any remaining oxidized Galinstan, the vias are flushed with an NaOH solution after being emptied. The filter has a frequency range of 10.13-11.31 GHz, an insertion loss of 1.35 dB, and an unloaded quality factor of 154.

A liquid metal-based bandwidth reconfigurable filter using substrate integrated waveguide (SIW) technology is demonstrated in [46]. The design incorporates two cavity resonators that can be continuously tuned and are interconnected by an innovative inductive iris design. To adjust the bandwidth, five liquid metal posts are placed in the inductive iris, and each post can be either capacitively loaded to increase inter-resonator coupling or short-circuited to reduce the effective iris width. This combination of capacitive loading and inductive shorting provides a broad range of achievable bandwidths across the device's frequency tuning range. The filter samples were produced and tested, demonstrating the efficacy of the iris tuning mechanism by generating a 541 MHz Butterworth response and a 278 MHz Butterworth response through the tuning of the liquid metal in the five iris tuning posts. The implemented filter and its response is shown in Fig. 1.19 and Fig. 1.20.

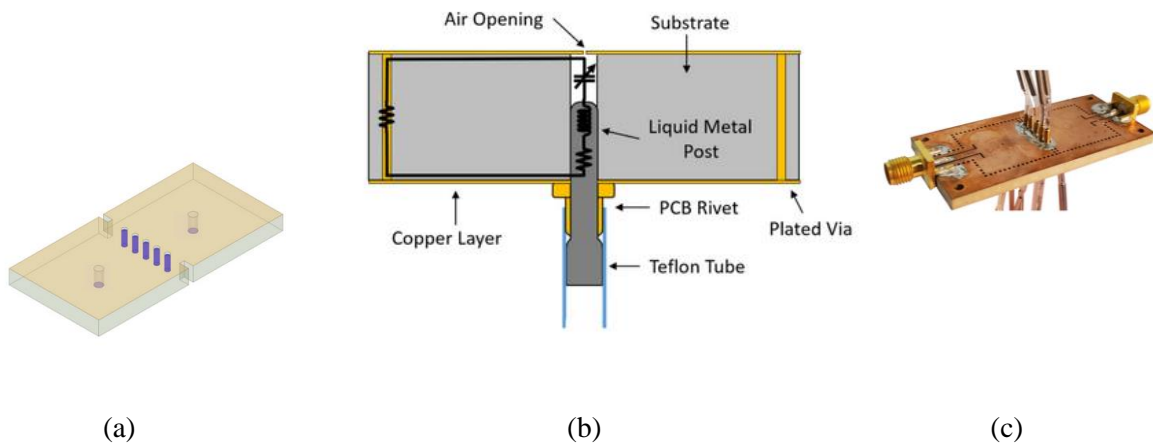


Fig. 1.19. Liquid-Metal based Tunable Band pass Filter (a) EM model, (b) cross-sectional view and (c) fabricated filter [46].

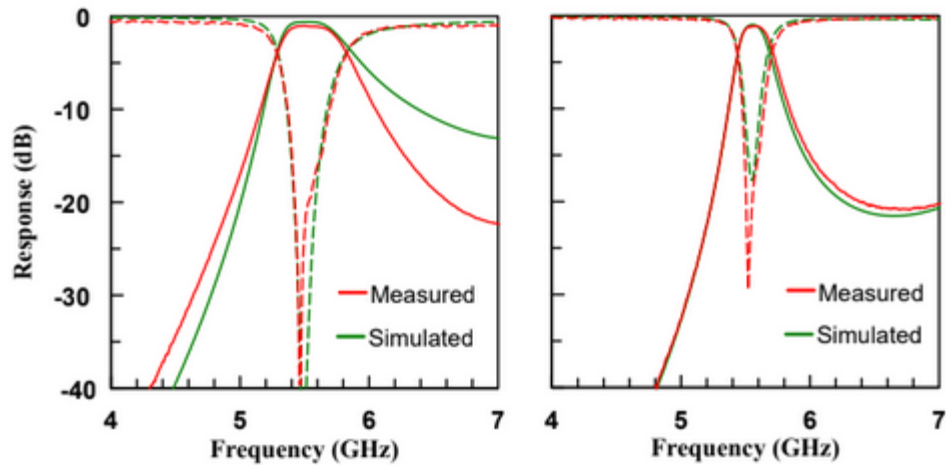


Fig. 1.20. The simulated and measured performance of the filters tuned to different bandwidths [46].

1.2.6 Summary

Some of the most promising approaches to create tunable components such as using ferroelectric material, MEMS, microfluidics, varactor diode and PCM switches have been studied in this section. Table 1.1 summarizes the pros and cons of all these methods. Based on these observations and our requirements, varactor diodes seems to be the most suitable due to its surface mounting capability and numerous variable capacitance values. It provides well spread tuning range when dealing with the devices that are made using PCB technology. Therefore, varactor diodes have been chosen in this project to achieve reconfigurability in the Field Programmable Microwave Substrate (FPMS) discussed in Chapter 2.

Table 1.1: Pros and Cons of different tuning methods

Tunable Mechanism	Pros	Cons
Ferroelectric	Higher frequency range, low power consumption	High insertion loss, Expensive
MEMS	High tuning accuracy, High Q factor	Expensive
Phase Change Materials	High tuning speed, small size	Limited tunability range, high cost
Varactor Diodes	Fast response time, compact size, low cost, wide frequency range, surface mount capability	High losses
Microfluidics	High tuning range	Low Quality factor, high losses

The methods discussed in this section have been developed to perform a single RF function only. For instance, a tunable band pass filter can be operated at different center frequency and bandwidths, however it always works as a filter. In the next section, reconfigurable devices that can perform different functions using a single hardware are studied.

1.3 Reconfigurable Devices

Reconfigurable devices are electronic devices that can be dynamically modified or altered to perform different functions. They are designed to be flexible and adaptable, allowing for a change in functionality without the need for physical modification or replacement of the underlying hardware. This capability enables reconfigurable devices to be used in a wide range of applications, such as high-performance computing, communication systems, and signal processing.

The use of reconfigurable devices can offer several advantages over traditional fixed-function devices. For example, they can increase efficiency and reduce design time and costs by allowing for a single device to be used for multiple applications. They can also improve system performance by allowing for real-time modification of the device's functionality. Additionally, reconfigurable devices can be more power-efficient than traditional fixed-function devices because they can be optimized for specific tasks and can be reconfigured to shut down unused portions of the device.

In conclusion, reconfigurable devices are a powerful and flexible technology that can be used in a wide range of applications. Their ability to dynamically change functionality offers many advantages over traditional fixed-function devices, making them an attractive option for design engineers. In this section, we will focus on reconfigurable devices that can create different functions or combine some of them.

1.3.1 Programmable Microwave Function Array (PROMFA)

The concept of Programmable Microwave Function Array (PROMFA) is based on an array of generic cell that is used to accomplish different functions [47-48]. Each PROMFA cell has four ports, it is simple to link many cells to form bigger arrays. Figure 1.21 shows a block schematic overview of PROMFA based system. Digital control logic is inserted between the connected analog building blocks (PROMFA cells) in order to regulate the behavior of each analog cell. Each PROMFA cell can be set up differently, such as an amplifier, power splitter, power combiner, router, etc. As a result, the array can implement more complicated functions like oscillators or filters. Multiple functions can be accomplished simultaneously with a vast array of PROMFA cells. The PROMFA cell was created using OMMIC's ED02AH GaAs process [47].

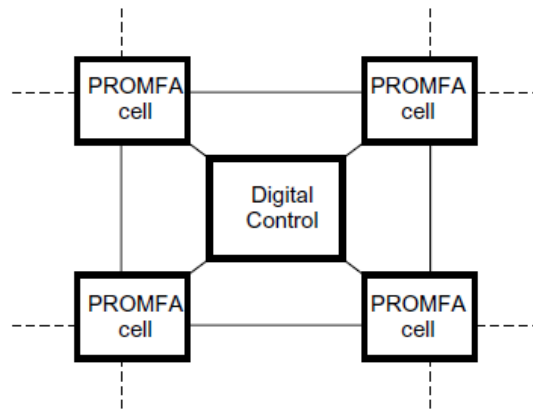


Fig.1.21. Block diagram of the PROMFA [47]

The four distinct ports of the PROMFA cell can be connected to one another in a number of different ways. Any port can be either an input or an output due to the symmetry of the cell. Depending on how the cell is biased, the signal route can be either of the pass-transistor type (basic switch) or amplifying which results in a variety of configurations. The circuit can be scaled to operate in other frequency ranges even though it is designed for 8–12 GHz. Good matching at the ports is demonstrated by simulation results, hence no further matching network is needed. The layout is small because the cell is built with almost only transistors. For biasing, a few passive components are required. The block diagram depicted in Figure. 1.22, describes the single cell of PROMFA. A common gate stage is positioned at each of the four ports to achieve good matching to both adjacent cells and a 50Ω system. The eight grey blocks are transistor arrays with common source stages. The signal is amplified by the common source stages. Switching transistors, represented by the white blocks, are utilized for two-way signal lines. Different functionalities are achieved by turning on certain phases.

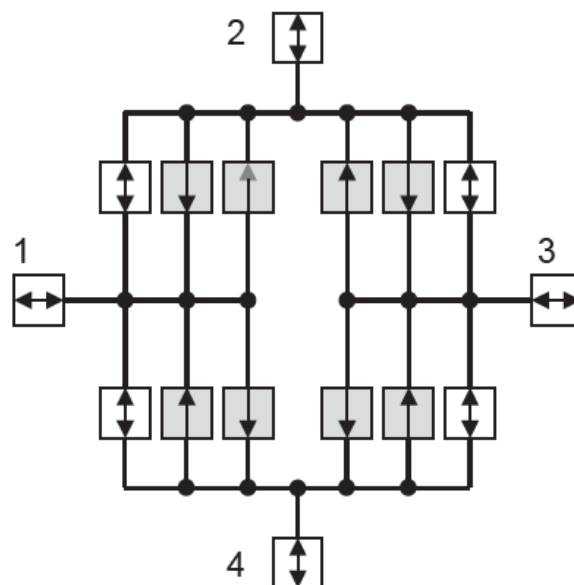


Fig.1.22. Block diagram of a single PROMFA cell [47]

A PROMFA cell can be configured in a variety of ways. One of this is a power splitter, from port 1 to port 2 and port 4 as shown in Figure 1.23(a). S_{21} and S_{41} are the same because of the symmetry of the cell. The figure's black blocks represent ports and stages that have been turned off. Any one of the four ports might serve as the input port because the cell is symmetric. Figure 1.23(b) displays the power splitter's S-parameters.

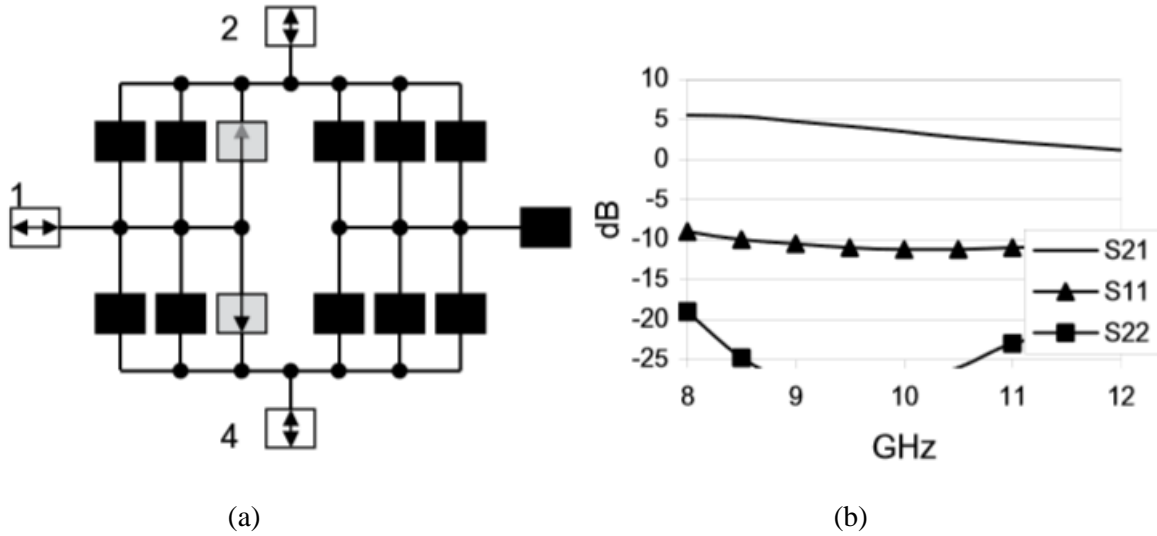
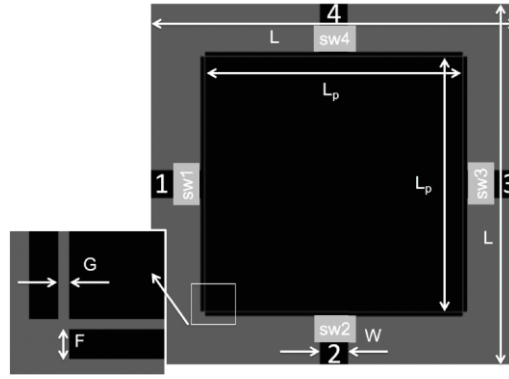


Fig.1.23. (a) Block diagram of power splitter and (b) simulated S-parameters [47]

1.3.2 Microstrip square patch resonator

This method describes a reconfigurable microwave device that can switch between operating as an antenna or a filter [49]. The system's core consists of a single-resonant element, or "building block element," (BBE) coupled to four ports. A 2.45 GHz microstrip square patch serves as the resonant component. The main objective behind its design was to build a device that allows a single resonator to perform different functions. There are four modes that are excited as a pair of coupled characteristics within the resonator and hard wired switches are used to change the mode. In order to facilitate electronic control, p-i-n diodes have also been added to the devices.



$L = 45 \text{ mm}$, $L_p = 31.6 \text{ mm}$, $W = 3.36 \text{ mm}$, $F = 0.4 \text{ mm}$ and $G = 0.15 \text{ mm}$.

Fig.1.24 Structure of the BBE. [49]

The structure of the BBE and its corresponding dimensions are shown in Figure. 1.24. Rogers 4003, with a relative permittivity of 3.55 and a thickness of 1.524 mm, served as the substrate. Four microstrip feedlines that have been created to have a characteristic impedance of 50Ω surround the resonator. Through a small gap, designated as G , electromagnetic energy is coupled from the microstrip lines into the square patch.

Each of the microstrip feedlines contains a single microwave switch (depicted by the gray block in Figure. 1.24). The device's four switches can be configured to operate as a filter or an antenna by changing their states. The BBE offers two filter modes and two antenna modes. Filter action between ports 1 and 3 or 2 and 4 is possible in modes 1 and 2, respectively. Antenna operation is available on each of the four ports in modes 3 and 4. Different antenna modes provide various linear polarization states (i.e., vertical or horizontal). Hardwired switches were used to validate the BBE architecture in which copper metallization represents an ON-state switch, whereas the absence of copper metallization represents an OFF-state switch (i.e., a gap).

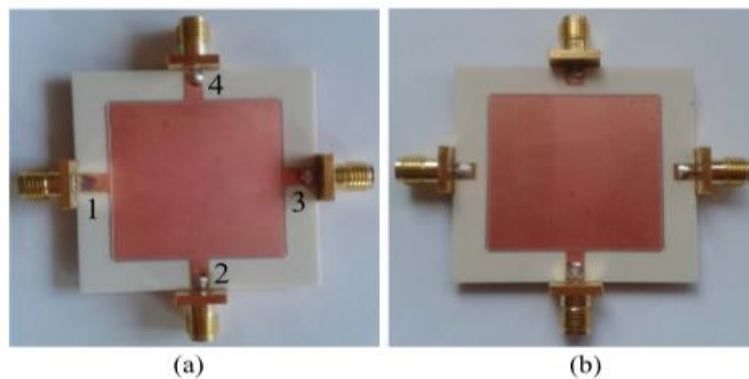


Fig.1.25. Hard-wired devices operating in (a) filter mode and (b) antenna mode [49]

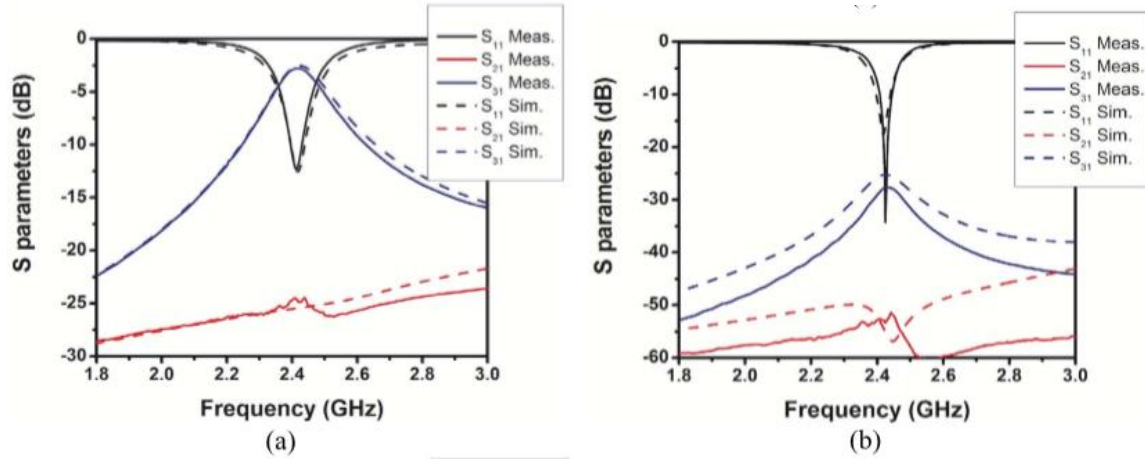


Fig.1.26. S- parameters for (a) filter mode and (b) antenna mode [49]

Figure 1.25 shows BBE with hardwired switches. The first one operates in filter mode with metallized copper in all four switch gaps. This allows for simultaneous filter mode performance across ports 1 and 3, as well as ports 2 and 4. The second one operates in antenna mode with vertical polarization. The simulation and measurement results are shown in Figure 1.26. In filter mode, the device operates at frequency of 2.41GHz with measured insertion loss and return loss are 2.8dB and 12.3 dB respectively. In antenna mode, the device operates at frequency of 2.42GHz with measured return loss 34.2dB at resonant frequency.

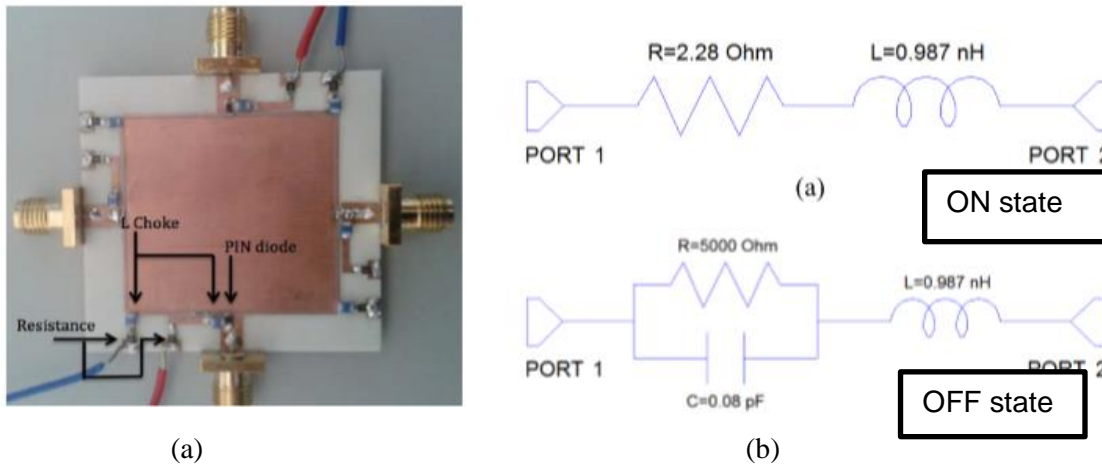


Fig. 1.27. (a) Single BBE incorporating p-i-n diode switches and (b) Lumped element equivalent circuits for the BAR50-02V p-i-n diode [49].

A prototype hardware of a single BBE was built with four p-i-n diode switches, which can switch between antennas and filter modes through voltage control. Infineon's BAR50-02V p-i-n diode was used for its availability and low cost. Computer simulations used lumped element equivalent circuits for the diode's ON and OFF states, and a biasing circuit was made with eight DC blocking inductors and an

83 Ω resistor to limit current and prevent damage to the diode while maintaining low-switch insertion loss. See Fig. 1.27 (a) and (b) for the prototype and the diode's equivalent circuits.

The scattering parameters for the single BBE were simulated and measured in Fig. 1.28, showing a bandpass response at 2.43 GHz and a -3 dB transmission bandwidth of 1.76% (42.8 MHz) in the filter mode, and a resonant frequency of 2.41 GHz and a return loss of around 20 dB in the antenna mode. Isolation between ports 1-3 is better than -20 and -30 dB for the filter and antenna modes, respectively. Total efficiency in antenna mode is 76.3%, and insertion loss in the filter mode is -3.38 dB. The switched single BBE has similar performance to the hard-wired prototype, but with some degradation due to losses introduced by the p-i-n diode switches.

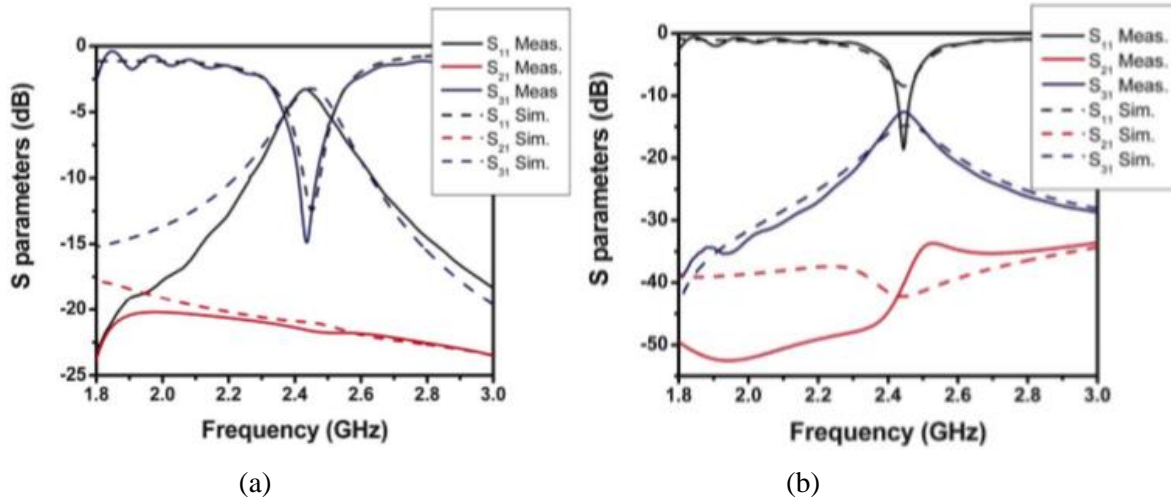


Fig. 1.28. S- parameters for (a) filter mode and (b) antenna mode [49].

The performance of a device can be modified by changing the permittivity and thickness of the substrate. For filter, high permittivity and low thickness is required whereas for antenna low permittivity and high thickness is required. Since the requirements for the filter and antenna are opposite, therefore a multifunctional device is a tradeoff between the filter and antenna performance.

1.3.3 Reconfigurable Circuits using Phase Change Materials

In general, passive microwave circuits and antennas have predefined metallic geometry according to their wavelength, therefore it cannot be modified after fabrication. In this method to realize programmable microwave circuits and antennas, the circuit's conductivity between that of metal and insulator has been set dynamically. The concept of abrupt transition of conductivity in phase-change materials (PCMs) has been used in [50].

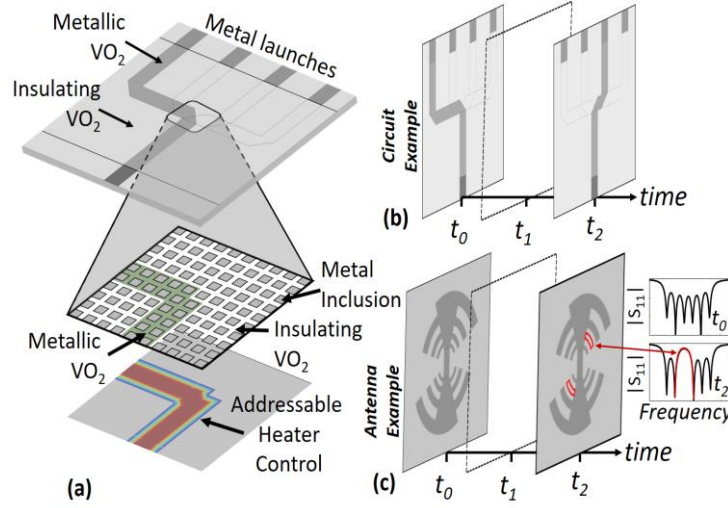


Fig.1.29 (a) VO₂ film on a microwave substrate with metallic and insulating layers to realize circuit and antenna, (b) circuit example and (c) antenna example [50].

Vanadium dioxide VO₂ film used as a PCM is illustrated in Figure 1.29(a). It can change its state from insulator to conductor through several techniques like local heating or illumination with high energy UV light. Here, a heater array is used to bias the VO₂ films in specified regions which is indicated by green metallic VO₂. The abrupt conductivity transition in VO₂ requires only a small change in temperature approximately 4° C and it occurs in less than 1 μ s. But to reduce the RF loss, there is need for integration of PCM and metallic surface inclusions which introduces a tradeoff between the loss reduction in metallic ON state and increased isolation in OFF state. The boundary between metallic and insulating regions gets disturbed due to the capacitive coupling of metal surface inclusions in insulating VO₂ regions. Ultimately to reduce the loss, high metal percentage is required but for proper reconfigurability, it should be small so that the boundary between the conducting and insulating regions can be defined. This method can be used for building programmable circuits and antennas as shown in Figure 1.29(b) and (c).

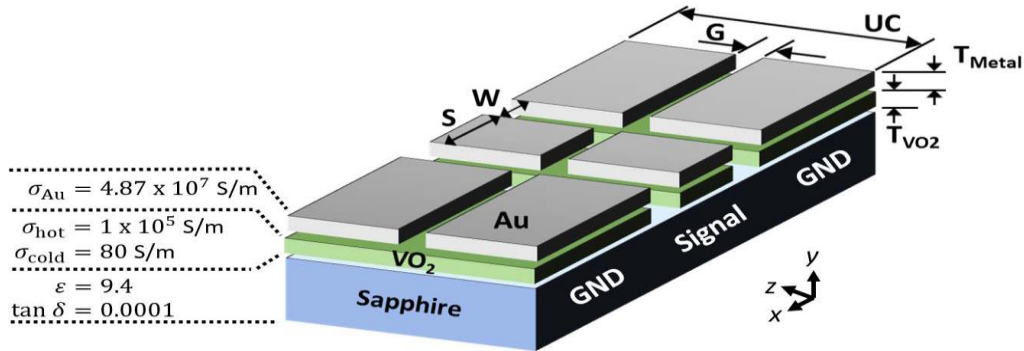


Fig.1.30. Unit-cell of a CPW transmission line comprising a VO₂ film (green layer) with gold inclusions (gray layer) on a sapphire substrate (blue layer) [50].

The unit cell of CPW transmission line consists of three layers is shown in Figure 1.30. The first layer with blue colour is a sapphire substrate, second layer with green colour is VO₂ film and third layer with gray colour is gold inclusions. The thickness of VO₂ film and gold inclusions are 17nm and 200nm respectively. Sapphire substrate has a thickness of 452μm. The values for unit cell length (UC) and unit cell gap (G) are 10μm and 2μm. It can be modified for different structures. Other fabricated unit-cell parameters S and W are 106.5 μm and 45 μm respectively. The coplanar waveguide (CPW) is designed using eight of these unit cells.

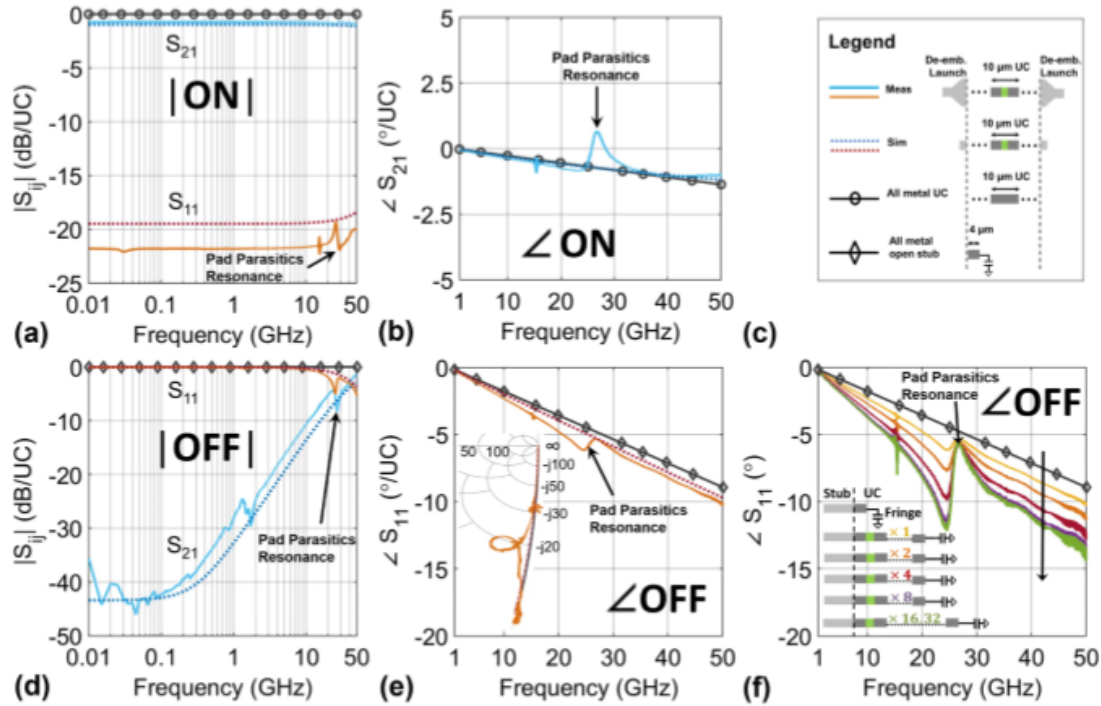


Fig. 1.31. S-parameters for CPW structure. Solid line: measured. Dotted line: simulated using MoM.
(a)–(c) and (d)–(f) ON-state and OFF-state results, respectively [50].

The measured (solid) and simulated (dotted) S-parameters of the de-embedded unit cell are depicted in Figure 1.31 in metallic and insulating states, respectively, with the labels "ON" and "OFF." The insertion loss in the ON state for the VO₂ based unit cell is 0.867dB per unit cell whereas for the metal-based unit cell it is 0.0022dB per unit cell. As we increase the thickness of VO₂ film and reduce the unit cell gap, the insertion loss will decrease.

As mentioned earlier, both low ON state insertion loss and high OFF state isolation is required to define the current path. For the frequencies below 200MHz, the isolation in OFF state is greater than 40dB and it decreases with the increase in frequency. It indicates that below 200MHz insertion loss dominates and above 200MHz, the unit cell gap capacitance dominates. So, the operating bandwidth of the CPW structure is decided by ON state insertion loss, which gives the lower frequency bound, and OFF state isolation, which gives upper frequency bound.

One-dimension realization of this concept is demonstrated by a reconfigurable dipole with 100- μm unit cells working in 2-17 GHz frequency range.

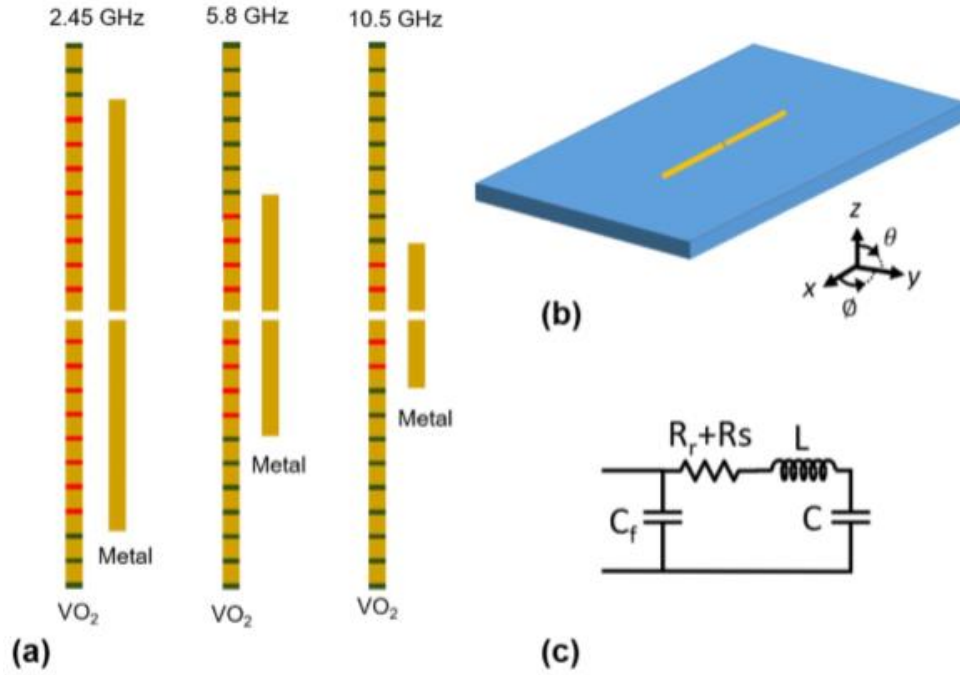


Fig.1.32. (a) Metal dipoles and VO₂ at 2.45, 5.8, and 10.5 GHz. (b) Dipoles modeled on a sapphire substrate. (c) Circuit model for each dipole consists of a feed capacitance in parallel with a series RLC circuit [50].

The simulation model of a reconfigurable VO₂-metal surface-inclusion dipole from 2.45 to 10.5 GHz is illustrated in Figure 1.32. The performance of VO₂ and metal based dipoles have been compared. To achieve resonance frequencies of 2.45, 5.8, and 10.5 GHz, the metal dipoles had lengths of 38, 14.16, and 7.06 mm. In order to simulate a true reconfigurable dipole, the VO₂ dipoles, which are made up of ON-state unit-cells, also have OFF-state unit-cells at the ends. This adds to their length (physically and electrically) and as a result, their resonant frequencies are 2.13, 5.24, and 9.07 GHz. The VO₂ film thickness was set at 100 nm, the metal thickness at 0.5 μm , the gap at 100 nm, and the dipole width at 200 μm . The dipole was modeled using $\sigma_{\text{ON}} = 10^5 \text{ S/m}$ for unit-cells in the ON-state and $\sigma_{\text{OFF}} = 80 \text{ S/m}$ for unit-cells in the OFF-state.

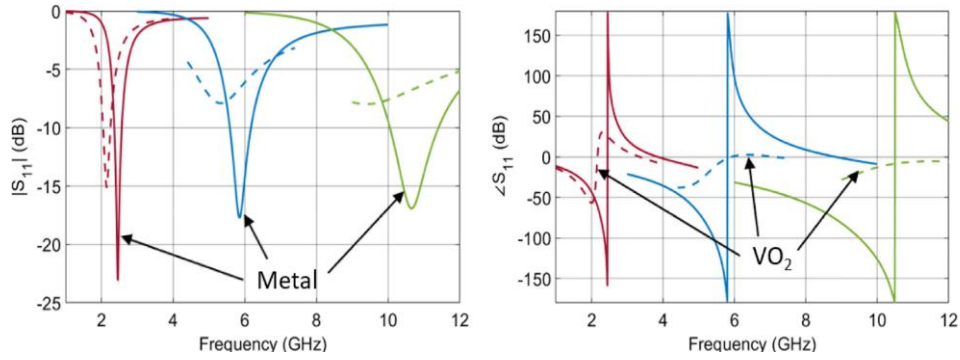


Fig.1.33. Simulated S-parameters of each metal (solid) and VO₂ dipole (dashed): red is 2.45 GHz, blue is 5.8 GHz, and green is 10.5 GHz [50].

The simulation results of VO₂ dipole and metal dipoles are shown in Figure 1.33. The length of metal dipoles is chosen in order to be resonant at 2.45, 5.8 and 10.5GHz. The VO₂ dipoles consist of both ON state and OFF state unit cells and resonate at 2.13, 5.24 and 9.07GHz. The slightly lower resonance frequency of VO₂ dipole than metal dipole is due to the increased capacitance at the ends due to the OFF state unit cells. The gain of VO₂ dipole is also lesser than the metal but it has tuning ratio of 4.25 which makes it useful for a wide range of frequencies.

1.3.4 Programmable Bridged T-Coil Array

A new configurable microwave passive component that can perform a number of different tasks is studied in [51]. The 2-D bridged-T coil (BTC) array forms the foundation of the proposed reconfigurable microwave circuit which can be designed to resemble a piece of a transmission line. The proposed bridged-T coil array can be programmed to perform a variety of functions, including filters, directional couplers, and power dividers, by strategically placing bridged-T coils with various equivalent characteristic impedances and electrical lengths in the array and enabling interconnections between bridged-T coils using bonding wires.

A design example based on the circuit structure in Figure. 1.34 is implemented as a proof-of-concept utilizing a silicon-based integrated passive device (IPD). A bridged-T coil with the defined equivalent characteristic impedance and electrical length at the center frequency is represented by each box in Figure 1.34(a). Through various wire-bonding configurations, the method can accomplish different functions such as bandpass filter, band stop filter, directional coupler and power divider. The suggested architecture can offer outstanding configurability allowing the same IPD chip to be customized for any application as compared to the traditional programmable microwave circuits that can only perform a small number of circuit tasks. Additionally, a significant size reduction is accomplished in comparison to designs for programmable microwave passive components made with traditional technology.

The wire-bonding design for a two-way power divider with a center frequency of around 4 GHz is shown in Figure 1.36(a). The analogous transmission-line model for 4 GHz, which corresponds to a two-way Wilkinson power divider, is shown in Figure 1.36(a). Figure 1.36(b) depicts the fabricated chip for the power divider function. The same IPD chip uses an incorporated thin-film resistor with bonding pads inserted at its two ends to implement the necessary isolation resistor R .

The measured and EM simulated S-parameters are shown in Figure 1.36(c). From 2.96 to 4.34 GHz (fractional bandwidth = 37.8%), the measured input return loss, output return loss, and isolation are all better than 15 dB, while the measured insertion loss is within 4.5 dB in the same frequency range. The implemented circuit's arrangement is not symmetrical, and as a result, there is some variation between $|S_{21}|$ and $|S_{31}|$ as can be seen in Figure. 1.36(c). Nevertheless, the measured in-band amplitude imbalance is within 0.36 dB.

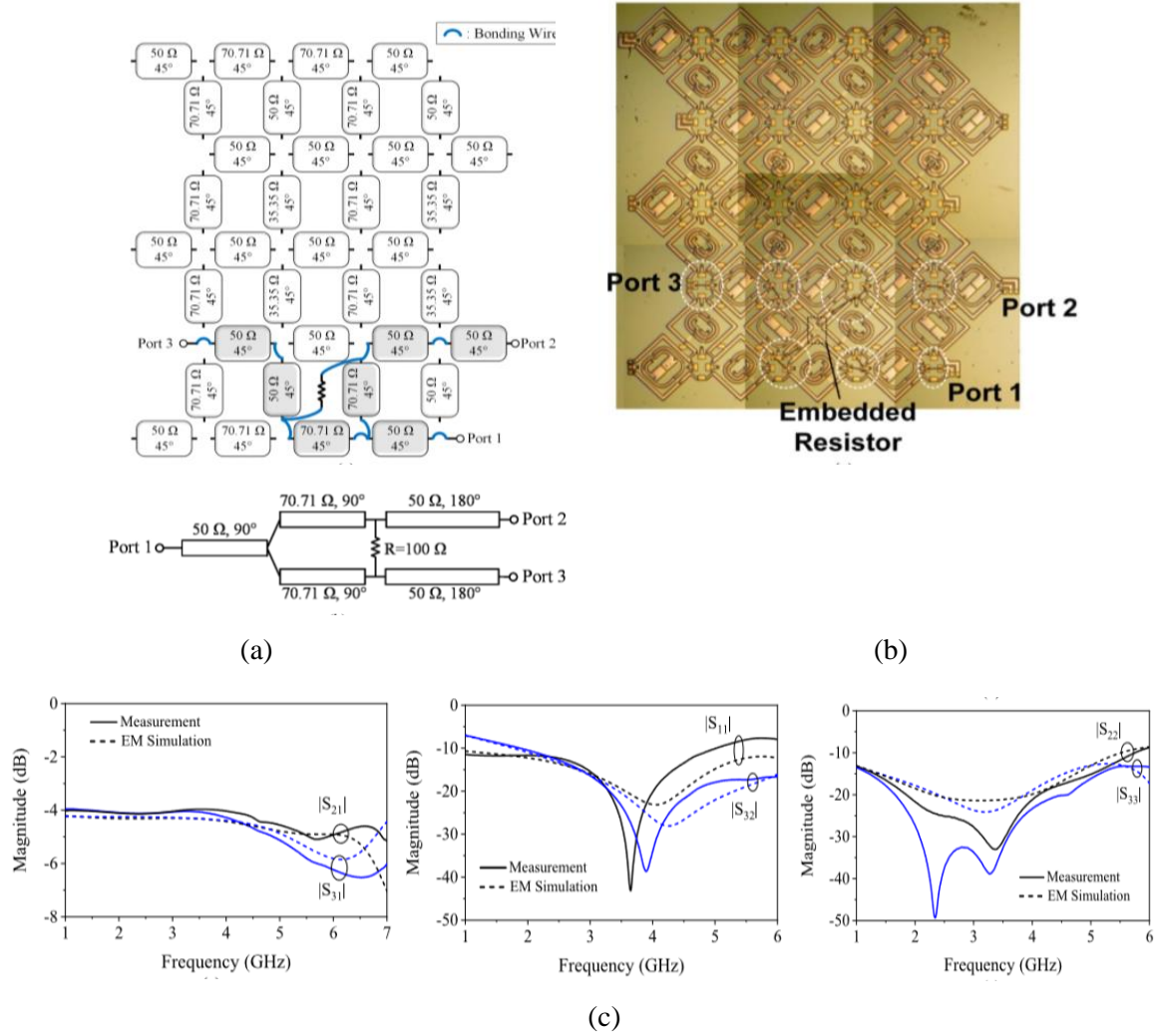


Fig.1.36. (a) Wire-bonding configuration for a power divider at 4 GHz and the corresponding equivalent transmission-line model at $2 f_0=4$ GHz. (b) Fabricated Chip and (c) Measured and EM simulated results [51].

Employing the wire-bonding configuration depicted in Figure 1.37(a) can facilitate the functioning of a 4-GHz bandstop filter and the resulting fabricated chip image is displayed in Figure 1.37(b) with the bonding wire locations highlighted. As indicated by the measured and EM simulated results shown in Figure 1.37(c), the bandstop filter generates a response centered around 4 GHz, and the stopband rejection measures more than 30 dB from 3.36 to 4.6 GHz (fractional bandwidth = 31.2%).

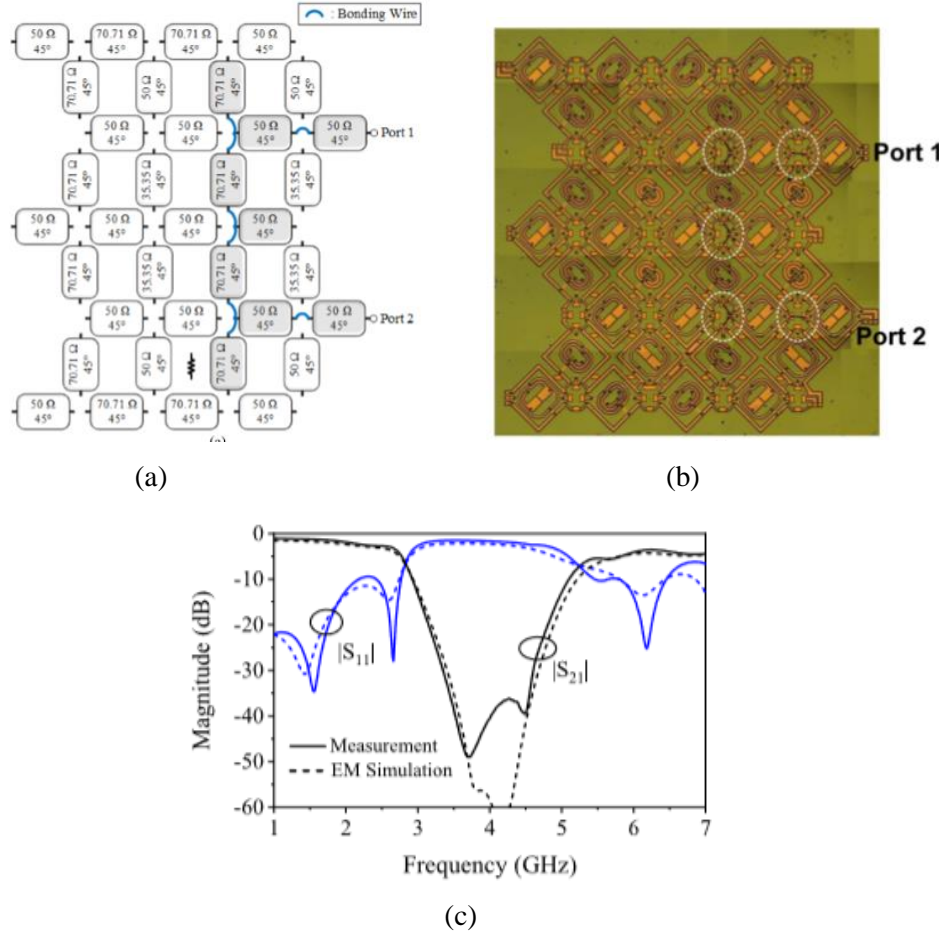


Fig.1.37. Band stop filter (a) Wire-bonding configuration, (b) Fabricated chip and (c) Measured and EM simulated results [51].

An alternative approach is to use the wire-bonding configuration illustrated in Figure 1.38(a) to configure into a bandpass filter centered around 4 GHz. Figure 1.38(b) displays the corresponding photograph of the chip, while Figure 1.38(c) presents the measured and EM simulated results. In the passband region, the measured insertion loss is less than 3 dB from 3.19 to 4.54 GHz, and the measured in-band return loss is better than 10 dB. With respect to the stopband, the measured stopband rejection measures more than 25 dB from DC to 1.45 GHz and from 6.19 to 7.66 GHz.

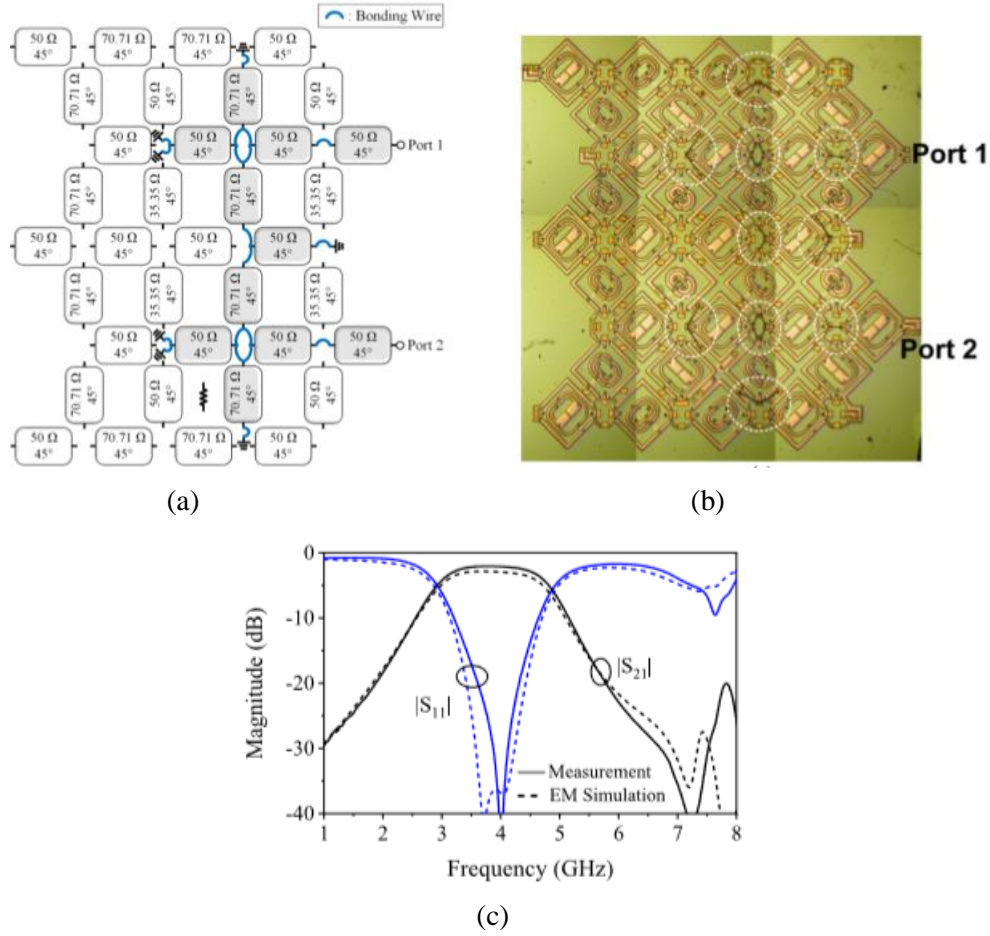


Fig.1.38. Band pass filter (a) Wire-bonding configuration, (b) Fabricated chip and (c) Measured and EM simulated results [51].

In practical applications, the wire bonding packaging of the IPD chip onto the motherboard or package substrate [52], [53] can be used to configure the suggested programmable bridged-T coil array. A single chip can be applied to many different applications in this fashion. If the IPD chip is prefabricated in high production, this substantially reduces the design turnaround time and fabrication costs, which is beneficial for fast prototyping of RF front end. But this circuit cannot be reconfigured on the fly since every function is hard wired.

1.3.5 Reconfigurable Microwave Components using software

The work in [54] proposed a new kind of programmable passive microwave component, with the goal of creating a reconfigurable microwave passive component that can be controlled by software, similar to how a field programmable gate array (FPGA) works in the digital domain. The component is made up of basic functional units, transmission units, and microwave switches, which are the building blocks used to create different topologies that alter the distribution of the electromagnetic field (EM), resulting in different functions of the component. The design as shown in Figure 1.39(a) is based on a planar

micro-strip (MS) patch circuit and uses resonance patch, slot, and coupling MS line as the basic functional units, as well as impedance transformation and MS transmission lines as the basic transmission units. Microwave p-i-n diode switches are used to connect these units and form different topologies that can function as an antenna, filter, splitter, or coupler as shown in Figure 1.39(b). An FPGA is used as the control circuit.

A prototype of the component was fabricated and measured, and the results are shown in Figure 1.40 for all the four functions. The antenna central frequency is 3.22 GHz with a realized gain of 6.2 dBi, the filter has a passband of 3.35-3.53 GHz (a fractional bandwidth of 6.3%) with an insertion loss of approximately 2.7 dB, the splitter has a working band of 2.4-3.5 GHz with a 1.6 dB insertion loss, a ± 0.4 dB amplitude unbalance, and a $\pm 3.4^\circ$ phase unbalance, and the coupler works at 2.5-5 GHz, with an insertion loss of approximately 1.7 dB and a coupling coefficient of approximately 30 ± 1.4 dB.

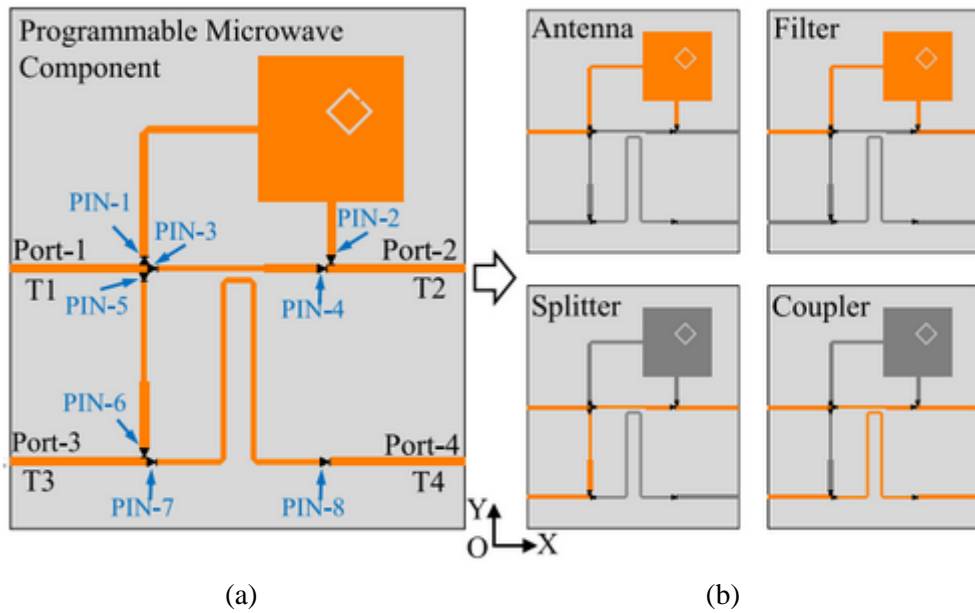


Fig.1.39 (a) Functional Programmable Microwave Component (FPMC) topology and (b) Circuit topologies for antenna, band pass filter, splitter, and coupler functions with the active units shown in orange and inactive units shown in gray [54].

1.3.6. Filtenuator

The method used in [55] introduces a new concept called the "filtenuator" which combines adjustable passband attenuation and filtering characteristics in a single design. The equations linking the desired passband loss to the necessary resistance values are presented and confirmed through circuit simulations. To demonstrate the concept, a third-order Chebyshev static filtenuator is designed at 1 GHz with various attenuation values using lumped-element components as shown in Figure 1.41(a). The results obtained from simulated and measured experiments on a filtenuator are shown in Figure 1.41(b) and (c).

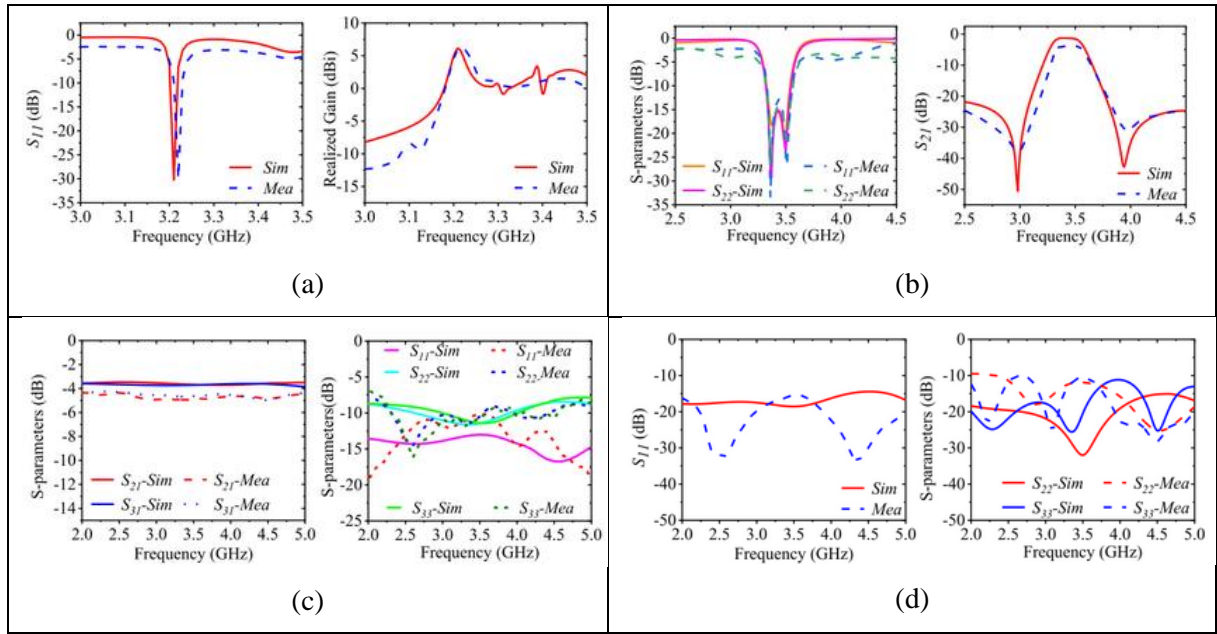


Fig. 1.40. Measured and simulated S-parameters (a) Antenna, (b) Bandpass filter, (c) Splitter and (d) Coupler [54]

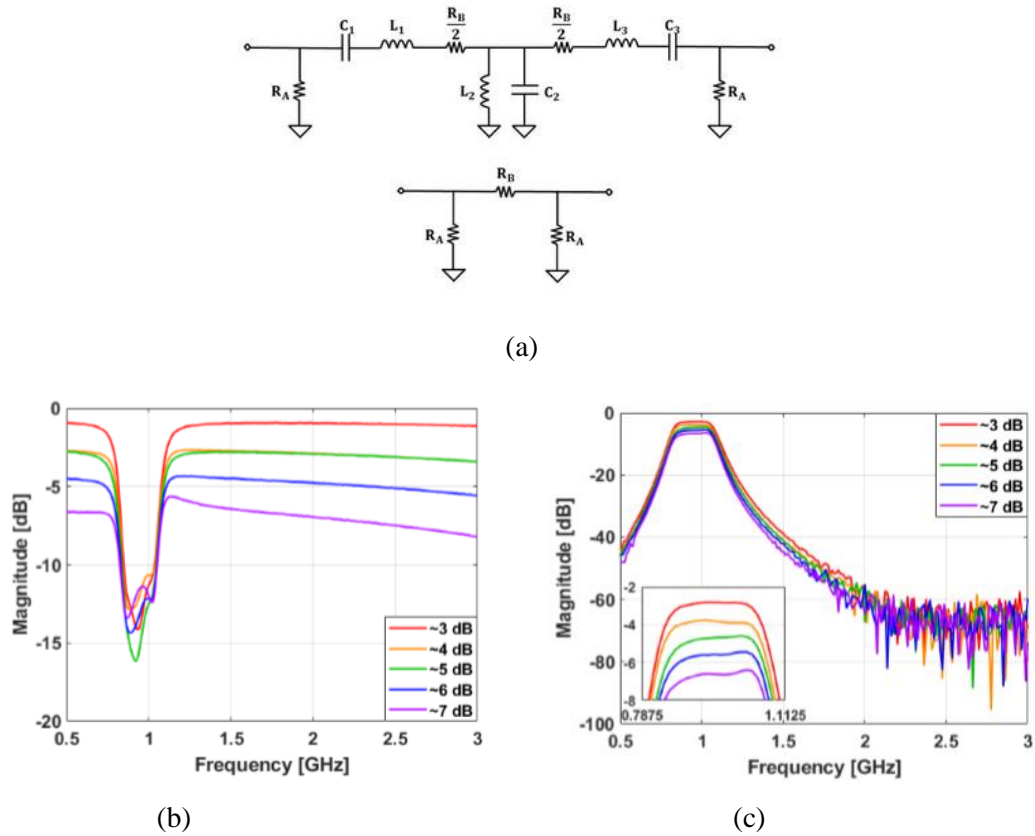


Fig.1.41 Filtenuator (a) Schematic, (b) Measured return loss and measured insertion loss [55]

Table 1.2: Recent Reconfigurable Multi-functional Microwave Components

Reference	[49]	[51]	[50]	[54]	[55]
Reconfigurable Method	p-i-n diode	Bonding Wire	PCM	Software & p-i-n diodes	Tuning resistance
Frequency range (GHz)	2-3	2-4	2-10	2.5-3.5	0.78-1.11
Insertion loss (dB)	2.8 to 3.4	3.7 to 4.7		1.6-2.7	3-7
General Comment		Not on the fly reconfigurability	No experimental demonstration	External control by FPGA	
Functions	Antenna	✓	✓	✓	
	Band pass filter	✓	✓	✓	✓
	Band stop filter		✓		
	Coupler		✓	✓	
	Power Divider		✓	✓	
	Attenuator				✓
	Phase Shifter				
	Signal Routing				

1.4. Conclusion

In this chapter, we have reviewed different approaches to realize a reconfigurable microwave component in the literature. There are numerous techniques for tuning and reconfiguring microwave circuits. First, we have reviewed different tunable mechanisms (Ferroelectric materials, MEMS, Varactor diode, Phase Change Materials and Microfluidics) that can tune the frequency, bandwidth etc. for a single function microwave component. Varactor diodes are the most popular tuning means thanks to its technological maturity, low cost and footprint and more generally ease of integration on any PCB even if it comes at the price of high losses due to its series resistance. Then we have discussed microwave devices which can perform different functions using the same hardware. Table 1.2 summarizes these devices. First of all, it is clear that only few devices exist in the literature that are capable of performing multiple functions. Also, most of these devices can perform 2 to 4 functions at a time. In [51], wire bonding is used for programmable microwave passive component during chip packaging, and thus reconfiguration is not possible on the fly by using an electrical command. Even if only a few have the capability to be reconfigured on the fly thanks to an FPGA that drives surfaces mounted p-i-n diodes for

example, none of these devices uses any kind of optimization techniques to improve their performance. Some of them also have not been validated by the experimental data.

The next chapter presents the concept of Field Programmable Microwave Substrate (FPMS) to realize a reconfigurable microwave device which can be used to obtain many microwave functions. This can be done by changing the bias voltage of unit cell of FPMS and an optimization algorithm has been proposed to improve the performance of FPMS based microwave devices on the fly.

1.5. References

- [1] <https://www.itu.int/hub/2019/03/why-wireless-standards-are-so-important-in-todays-world/>
- [2] D. M. Pozar, *Microwave Engineering*, 4th ed. Hoboken, NJ, USA: Wiley, 2011.
- [3] O. G. Vendik, L. T. Ter-Martirosyan, A. I. Dedyk, S. F. Karmanenko, and R. A. Chakalov, "High T superconductivity: New applications of ferroelectrics at microwave frequencies," *Ferroelectrics*, vol. 144, pp.33–43, 1993.
- [4] D. E. Oates, A. Piqué, K. S. Harshavardhan, J. Moses, F. Yang, and G.F. Dionne, "Tunable YBCO resonators on YIG substrates," *IEEE Trans. Appl. Superconduct.*, vol. 7, pp. 2338–2342, June 1997.
- [5] A. M. Hermann, R. M. Yandrofski, J. F. Scott, A. Naziripour, D. Galt, J. C. Price, J. Cuchario, and R. K. Ahrenkiel, "Oxide superconductors and ferroelectrics- materials for a new generation of tunable microwave devices," *J. Superconduct.*, vol. 7, no. 2, pp. 463–469, 1994.
- [6] S. S. Gevorgian, D. I. Kaparkov, and O. G. Vendik, "Electrically controlled HTSC/ferroelectric coplanar waveguide," *Proc. Inst. Elect. Eng.*, vol. 141, pp. 501–503, 1994.
- [7] Félix A. Miranda, Guru Subramanyam, Frederick W. Van Keuls, Robert R. Romanofsky, Joseph D. Warner, and Carl H. Mueller, "Design and Development of Ferroelectric Tunable Microwave Components for Ku- and K-Band Satellite Communication Systems" , *IEEE TRANSACTIONS ON MICROWAVE THEORY AND TECHNIQUES*, VOL. 48, NO. 7, JULY 2000 pp 1181-1189
- [8] H. jiang, B. Lacroix, K. Choi, Y. Wang, A. T. Hunt, and J. Papapolymerou, "Ka and U- band Tunable Bandpass Filters Using Ferroelectric Capacitors," *IEEE Trans. Microw. Theory Tech.*, vol. 59, no. 12, pp. 3068–3075, Dec. 2011.
- [9] A. Jajoo, L. Wang, and T. Mukherjee, "MEMS varactor enabled frequency reconfigurable LNA and PA in the upper UHF band," in *Microwave Symposium Digest, 2009. MTT '09. IEEE MTT-S International*, 2009, pp. 1121–1124.
- [10] A. Fukuda, H. Okazaki, S. Narahashi, T. Hirota, and Y. Yamao, "A 900/1500/2000- MHz triple-band reconfigurable power amplifier employing RF MEMS switches," in *Microwave Symposium Digest, 2005 IEEE MTT-S International*, june 2005, p. 4 pp.
- [11] J. Iannacci, F. Giacomozzi, S. Colpo, B. Margesin, and M. Bartek, "A general purpose reconfigurable MEMS-based attenuator for radio frequency and microwave applications," in *EUROCON 2009, EUROCON '09. IEEE*, may 2009, pp. 1197 –1205.
- [12] D. Qiao, R. Molfino, S. Lardizabal, B. Pillans, P. Asbeck, and G. Jerinic, "An intelligently controlled RF power amplifier with a reconfigurable MEMS varactor tuner," *Microwave Theory and Techniques, IEEE Transactions on*, vol. 53, no. 3, pp. 1089 – 1095, march 2005.

- [13] S. Fouladi, A. Akhavan, and R. Mansour, "A novel reconfigurable impedance matching network using DGS and MEMS switches for millimeter-wave applications," in *Microwave Symposium Digest, 2008 IEEE MTT-S International*, june 2008, pp. 145 –148.
- [14] S. Fouladi, F. Huang, W. D. Yan, and R. Mansour, "Comblne tunable bandpass filterusingRF-MEMSswitchedcapacitorbank,"in*MicrowaveSymposiumDigest (MTT)*, 2012 IEEE MTT-S International, june 2012, pp. 1 –3.
- [15] M. S. Arif and D. Peroulis, "A 6 to 24 GHz continuously tunable, microfabricated, high-Q cavity resonator with electrostatic MEMS actuation," in *Microwave Symposium Digest (MTT)*, 2012 IEEE MTT-S International, june 2012, pp. 1 –3.
- [16] Yonghyun Shim, Jia Ruan, Zhengzheng Wu, and Mina Rais-Zadeh, "AN INTEGRATED RF MEMS TUNABLE FILTER", 2012 IEEE International conference on Micro-electromechanical systems (MEMS).
- [17] Y. Shim, et al, "A multi-metal surface micromachining process for tunable RF MEMS passives," *Journal of Microelectromechanical System*.
- [18]Y. Shim, et al, "A high-performance, temperature-stable, continuously tuned MEMS capacitor," *IEEE MEMS Conf.*, pp. 752-755, Jan. 2011.
- [19] A. Mennai, A. Bessaudou, F. Cosset, C. Guines, D. Passerieux, P. Blondy, and A. Crunteanu, "High cut-off frequency RF switches integrating a metalinsulator transition material," in *Microwave Symposium (IMS)*, 2015 IEEE MTT-S International, May 2015, pp. 1–3.
- [20] N. El-Hinnawy, P. Borodulin, B. Wagner, M. King, J. Mason, E. Jones, V. Veliadis, R. Howell, R. Young, and M. Lee, "A 7.3 THz cut-off frequency, inline, chalcogenide phase-change RF switch using an independent resistive heater for thermal actuation," in *Compound Semiconductor Integrated Circuit Symposium (CSICS)*, 2013 IEEE, Oct 2013, pp. 1–4.
- [21] N. El-Hinnawy, P. Borodulin, M. Torpey, F. Kuss, A. Ezis, J. Paramesh, J. Bain, T. Schlesinger, R. Howell, M. Lee, D. Nichols, and R. Young, "Reconfigurable inline phase-change switches for broadband applications," in *Microwave Symposium (IMS)*, 2015 IEEE MTT-S International, May 2015, pp. 1–4.
- [22] N. El-Hinnawy, P. Borodulin, E. Jones, B. Wagner, M. King, J. Mason, J. Bain, J. Paramesh, T. Schlesinger, R. Howell, M. Lee, and R. Young, "12.5 THz Fco GeTe inline phase-change switch technology for reconfigurable RF and switching applications," in *Compound Semiconductor Integrated Circuit Symposium (CSICs)*, 2014 IEEE, Oct 2014, pp. 1–3.
- [23] M. Wang, Y. Shim, and M. Rais-Zadeh, "A low-loss directly heated two-port RF phase change switch," *Electron Device Letters, IEEE*, vol. 35, no. 4, pp. 491– 493, April 2014.

- [24] J. sunMoon, H. changSeo, and D. Le, "Development toward high-power sub-1ohm DC-67 GHz RF switches using phase change materials for reconfigurable RF front-end," in Microwave Symposium (IMS), 2014 IEEE MTT-S International, June 2014, pp. 1–3.
- [25] M. Wang and M. Rais-Zadeh, "Directly heated four-terminal phase change switches," in Microwave Symposium (IMS), 2014 IEEE MTT-S International, June 2014, pp. 1–4.
- [26] J. sun Moon, H.-C. Seo, and D. Le, "High linearity 1-ohm RF switches with phase-change materials," in Silicon Monolithic Integrated Circuits in RF Systems (SiRF), 2014 IEEE 14th Topical Meeting on, Jan 2014, pp. 7–9.
- [27] Y. Shim, G. Hummel, and M. Rais-Zadeh, "RF switches using phase change materials," in Micro Electro Mechanical Systems (MEMS), 2013 IEEE 26th International Conference on, Jan 2013, pp. 237–240.
- [28] M. Wang, F. Lin, and M. Rais-Zadeh, "Performance measurements and nonlinearity modeling of GeTe phase change RF switches with direct and indirect heating schemes," in Microwave Symposium (IMS), 2015 IEEE MTT-S International, May 2015, pp. 1–4.
- [29] J.-S. Moon, H.-C. Seo, D. Le, H. Fung, A. Schmitz, T. Oh, S. Kim, K.-A. Son, D. Zehnder, and B. Yang, "11 THz figure-of-merit phase-change RF switches for reconfigurable wireless front-ends," in Microwave Symposium (IMS), 2015 IEEE MTT-S International, May 2015, pp. 1–4.
- [30] J.-S. Moon, H.-C. Seo, D. Le, H. Fung, A. Schmitz, T. Oh, S. Kim, K.-A. Son, and B. Yang, "10.6 THz figure-of-merit phase-change RF switches with embedded micro-heater," in Silicon Monolithic Integrated Circuits in RF Systems (SiRF), 2015 IEEE 15th Topical Meeting on, Jan 2015, pp. 73–75.
- [31] D. Bouyge, A. Crunteanu, O. Massaguet' and, J.-C. Orlianges, C. Champeaux, A. Catherinot, A. Velez, J. Bonache, F. Martin, and P. Blondy, "Applications of vanadium dioxide (VO₂)-loaded electrically small resonators in the design of tunable filters," in Microwave Conference (EuMC), 2010 European, sept. 2010, pp. 822–825.
- [32] M. J. Dicken, K. Aydin, I. M. Pryce, L. A. Sweatlock, E. M. Boyd, S. Walavalkar, J. Ma, and H. A. Atwater, "Frequency tunable nearinfrared metamaterials based on VO₂ phase transition," *Opt. Express*, vol. 17, no. 20, pp. 18330–18339, Sep 2009. [Online]. Available: <http://www.opticsexpress.org/abstract.cfm?URI=oe-17-20-18330>
- [33] A. Crunteanu, J. Leroy, G. Humbert, D. Ferachou, J.-C. Orlianges, C. Champeaux, and P. Blondy, "Tunable terahertz metamaterials based on metalinsulator phase transition of VO₂ layers," in Microwave Symposium Digest (MTT), 2012 IEEE MTT-S International, june 2012, pp. 1–3.
- [34] S. Ha, Y. Zhou, A. Duwel, D. White, and S. Ramanathan, "Quick switch: Strongly correlated electronic phase transition systems for cutting-edge microwave devices," *Microwave Magazine*, IEEE, vol. 15, no. 6, pp. 32–44, Sept 2014.
- [35] Pierre Blondy, Ines Bettoumi, Nicolas Le Gall, "A Novel 2-Pole Tunable Coplanar Filter using Integrated Phase Change Material Switches", 2021 IEEE MTT-S International Microwave Filter Workshop (IMFW).

[36] https://www.electronics-notes.com/articles/electronic_components/diode/varactor-varicap-diode.php

[37] Eric W. Wells, Hjalti H. Sigmarsson, and Jay W. McDaniel, “Design of a Frequency-Agile and Surface Mountable Suspended Integrated Strip-Line Bandpass Filter Using Castellated Vias”, 2022 IEEE 22nd Annual Wireless and Microwave Technology Conference.

[38] A. Anand, J. Small, D. Peroulis, and X. Liu, “Theory and Design of Octave Tunable Filters With Lumped Tuning Elements,” *IEEE Trans. Microw. Theory Tech.*, vol. 61, no. 12, pp. 4353–4364, Dec. 2013.

[39] A. Anand and X. Liu, “Substrate-integrated coaxial-cavity filter with tunable center frequency and reconfigurable bandwidth,” in *Wireless and Microwave Technology Conference (WAMICON)*, 2014 IEEE 15th Annual, 2014, pp. 1–4.

[40] J. Dang, R. Gough, A. Morishita, A. Ohta, and W. Shiroma, “Liquid-metalbased reconfigurable components for RF front ends,” *Potentials, IEEE*, vol. 34, no. 4, pp. 24–30, July 2015.

[41] W. Irshad and D. Peroulis, “A 12-18 GHz electrostatically tunable liquid metal RF MEMS resonator with quality factor of 1400-1840,” in *Microwave Symposium Digest (MTT)*, 2011 IEEE MTT-S International, June 2011, pp. 1–4.

[42] R. Gough, A. Morishita, J. Dang, W. Hu, W. Shiroma, and A. Ohta, “Continuous electrowetting of non-toxic liquid metal for RF applications,” *Access, IEEE*, vol. 2, pp. 874–882, 2014.

[43] H.-T. Chen, W. Padilla, J. Zide, S. Bank, A. Gossard, C. Highstrete, M. Lee, J. O’Hara, A. Taylor, and R. Averitt, “Active metamaterials: A novel approach to manipulate terahertz waves,” in *Infrared and Millimeter Waves, 2007 and the 2007 15th International Conference on Terahertz Electronics. IRMMW-THz. Joint 32nd International Conference on*, sept. 2007, pp. 337–339.

[44] M. Wang, C. Trlica, M. R. Khan, M. D. Dickey, and J. J. Adams, “A reconfigurable liquid metal antenna driven by electrochemically controlled capillarity,” *Journal of Applied Physics*, vol. 117, no. 19, pp. –, 2015. [Online]. Available: <http://scitation.aip.org/content/aip/journal/jap/117/19/10.1063/1.4919605>

[45] J. Dang, R. Gough, A. Morishita, A. Ohta, and W. Shiroma, “A tunable X-band substrate integrated waveguide cavity filter using reconfigurable liquid-metal perturbing posts,” in *Microwave Symposium (IMS)*, 2015 IEEE MTT-S International, May 2015, pp. 1–4.

[46] Alex Pham, and Hjalti H. Sigmarsson, “Bandwidth-Reconfigurable Liquid-Metal Tunable Bandpass Filter”, 2021 IEEE MTT-S International Microwave Filter Workshop (IMFW).

[47] C. Samuelsson, A. Ouacha, N. Ahsan, and T. Boman, “Programmable microwave function array, PROMFA,” in *Proc. Asia-Pacific Microw. Conf.*, Dec. 2006, pp. 1787–1790.

- [48] N. Ahsan, A. Ouacha, C. Samuelsson, and T. Boman, “Applications of programmable microwave function array (PROMFA),” in *Circuit Theory and Design*, 2007. ECCTD 2007. 18th European Conference on, Aug 2007, pp. 164– 167.
- [49] Alejandro L. Borja, Yasin Kabiri, Angel Belenguer and James R. Kelly , “Programmable Multifunctional RF/Microwave Circuit for Antenna and Filter Operation” *IEEE Transactions on Antenna and Wave Propagation*, vol 66, no.8 pp.3865-3876, Aug 2018
- [50] David A. Connelly, and Jonathan D. Chisum, “Dynamically Reconfigurable Microwave Circuits Leveraging Abrupt Phase Change Material”, *IEEE Transactions on Microwave Theory and techniques*, vol. 68,no. 10, pp 4188-4205, Oct 2020.
- [51] Yo-Shen Lin, Pei-Shan Lu, and Yu-Cheng Wu, “A Novel Configurable Microwave Passive Component Based on Programmable Bridged-T Coil Array” *IEEE Transaction Microwave Theory and techniques*, vol. 69, no. 6,pp. 3001-3014, Jun. 2021.
- [52] Y. Yang, Y. Wu, Z. Zhuang, M. Kong, W. Wang, and C. Wang, “An ultraminiaturized bandpass filtering Marchand balun chip with spiral coupled lines based on GaAs integrated passive device technology,” *IEEE Trans. Plasma Sci.*, vol. 48, no. 9, pp. 3067–3075, Sep. 2020.
- [53] M. Kong, Y. Wu, Z. Zhuang, W. Wang, and C. Wang, “Ultraminiaturized wideband quasi-Chebyshev/-elliptic impedance-transforming power divider based on integrated passive device technology,” *IEEE Trans. Plasma Sci.*, vol. 48, no. 4, pp. 858–866, Apr. 2020.
- [54] Lei Sang, Ziyang Liu, Shuaitao Li, Wen Huang, Ping Li and Hao Tu “A Programmable Microwave Components Reconfigurable Between Four Functions” *IEEE Transactions on components, packaging and manufacturing technology*, vol. 13, no. 1, january 2023
- [55] Jonathan M. Knowles, Hjalti H. Sigmarsson, and Jay W. McDaniel , “Design of a Symmetric Lumped-Element Bandpass Filtering Attenuator (Filtenuator)”, 2022 IEEE 22nd Annual Wireless and Microwave Technology Conference (WAMICON).

Chapter 2.

Field Programmable Microwave Substrate

2.1 Introduction

Field Programmable Microwave Substrate (FPMS) [1] is a type of reconfigurable technology that allows to design and test microwave circuits, components, and sub-systems. FPMS typically consists of a substrate material, such as low-loss dielectric, and metal interconnected layers. The metal layers can be patterned to form the desired microwave circuits and components. The concept behind FPMS and its state-of-the-art results are presented in this chapter. FPMS offers several advantages over traditional microwave circuits, including reduced development time, low cost, and greater design flexibility. This technology can find applications in communication, radar and satellite systems.

FPMS is a programmable microwave circuit which has been developed to realize different microwave components from a single device. The main goal is to achieve the significant level of reconfigurability as FPGAs have in digital circuits but with microwave signals. This chapter covers the concepts and all the significant steps to build FPMS. An optimization algorithm has been proposed to improve the performance of FPMS based microwave devices by looking for the most optimal configuration of its unit cells. Different studies and tests on the optimization of an equivalent model are provided before applying the approach to the existing FPMS board.

There are large number of materials that are available in the literature which can be used to realize reconfigurable and tunable microwave circuits such as semiconductors switches, varactors, MEMS, materials with reconfigurable properties as discussed in previous chapter. While implementing the FPMS, metamaterials have been used. It is basically a class of engineered materials having specific effective permittivity and permeability which cannot be found in naturally occurring materials. Materials with engineered properties using metallic structuring provide a very unique opportunity for the reconfigurable properties by dynamically changing the current paths running through them.

These metamaterials can be divided into four categories based on the positive and negative value of permittivity and permeability as shown in Figure 2.1.

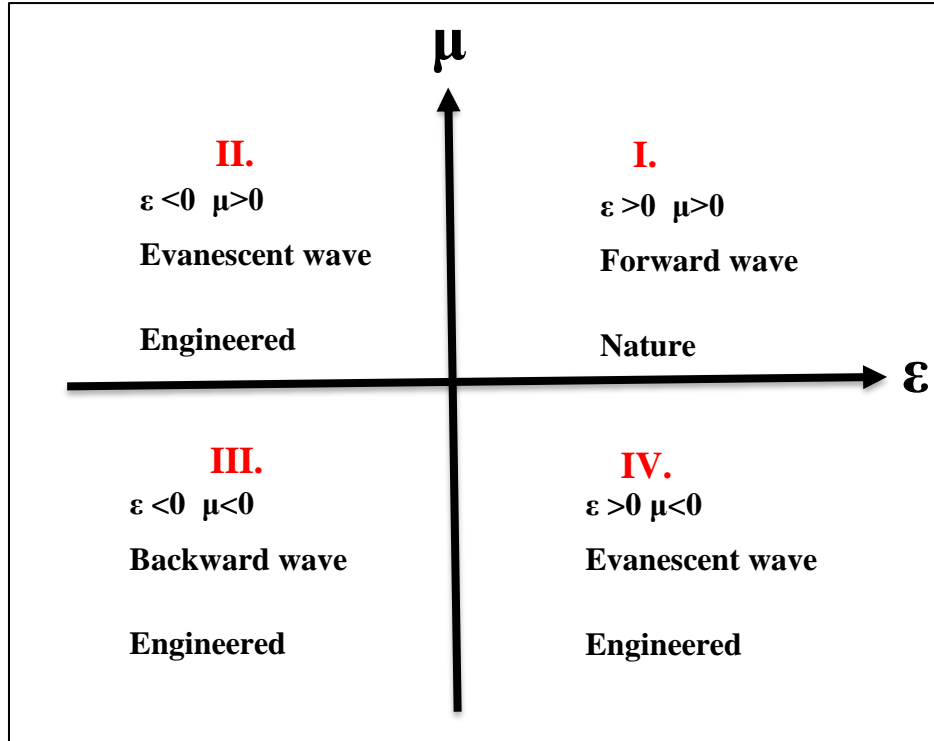


Fig. 2.1. Permittivity- Permeability values

Materials having positive values for both permittivity and permeability are easily available in nature, therefore this category is usually ignored for metamaterials. Materials having negative values for either permittivity or permeability or for both of them are usually engineered. The realization of waveguide based on the metamaterial structure referred as Field Programmable Microwave Substrate (FPMS) is presented in [1]. FPMS is made up of metamaterials in which permittivity value can be either positive or negative and permeability is positive i.e., it basically operates in I and II quadrant of Figure 2.1.

In general, most of the microwave circuit design uses a waveguide structure thus making it an essential component to achieve programmable microwave circuit. So, FPMS has been used here to implement programmable waveguides. The main building block of FPMS is a unit cell that is explained in the next section.

2.2 Unit Cell

A unit cell in Field Programmable Microwave Substrate (FPMS) technology refers to the smallest and periodically repeating unit of a microwave circuit. It is the building block that makes up the overall microwave structure and include various types of passive components, such as inductors, capacitors,

and resistors, as well as active components, such as transistors and diodes. The unit cell design is critical in determining the overall performance of the microwave circuit, including factors such as frequency response, impedance matching, and insertion loss.

In FPMS technology, the unit cell is made up of a combination of metal interconnects and a low-loss dielectric material. The metal interconnects form the electrical connections between the components and the dielectric material provides isolation between the different components and the metal interconnects. The unit cell design can be optimized for a specific application by adjusting the dimensions of the metal interconnects, the dielectric constant of the dielectric material, and the thickness of the dielectric layer.

The unit cell used to realize FPMS on FR4 substrate with dielectric constant 4.9 and loss tangent 0.02 is depicted in Figure 2.1. [1]. The effective dielectric constant can be switched between positive and negative values using this unit cell. A shunt varactor with a wide tuning range and high inductive package parasitic (1.8nH for the varactor chosen) is used to accomplish this. This enables the varactor to switch over a wide range between acting as a capacitor or an inductor. No bias (0V) produces a 12pF capacitance and the cell is series resonant at 1GHz for the selected varactor. The varactor has a capacitance value of 0.75pF, biased at 25V, and series resonant at 4.5GHz. The high series inductance was needed to decrease the impact of the varactor's $1.8\ \Omega$ resistance when biased at 0V. Since the varactor has very low resistance when reverse biased at 25 V, it's contribution to the total loss is very low compared to the dielectric loss tangent coming from the PCB itself. The varactor acts as a capacitor at frequencies below 1GHz that result in positive dielectric constant of unit cell. Above 1GHz it behaves as an inductor that results in negative dielectric constant.

The unit cell's main dimensions are as follows (see Figure 2.1):

- Distance from top metal to ground plane that is thickness = 1.171 mm,
- $L = 2.54\text{ mm}$,
- $W = 0.508\text{ mm}$.

It contains following components as seen in Figure 2.1:

- V1 is a varactor (BB 833 E6327),
- R1 is a 10-k Ω resistor (ERJ-2GEJ103X),
- Dielectric is FR4 with a dielectric constant of 4.9 and a dielectric loss tangent of 0.02,
- Vias-to-varactor bias passes via the ground plane with a clearance of 0.254 mm,
- Terminations have a value of 88.8 Ω (for simulation purpose).

The decoupling capacitor (C1), used in the unit cell is series resonant below the interested frequency range and it also provides an RF short while blocking the dc bias for the varactor. A resistor (R1) is required to isolate the varactor bias circuitry from the RF.

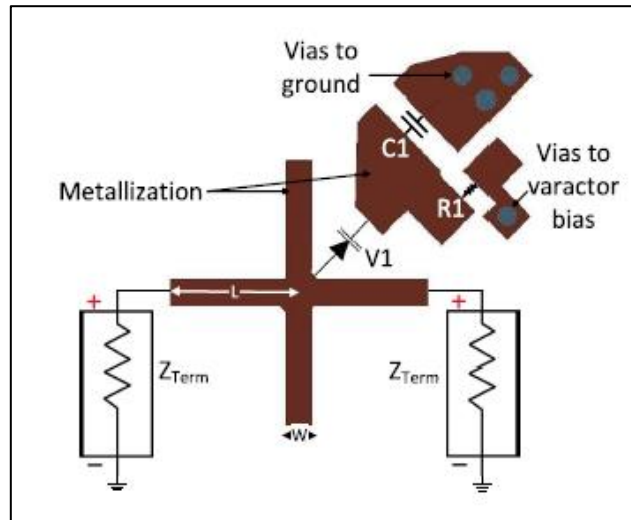


Fig. 2.1. Schematic of a Unit Cell of FPMS [1]

The unit cell's effective properties at various bias voltages are shown in Figures 2.2 -2.5. The characteristics in Figure 2.2 indicate how the bias on the varactor can alter the unit cell's effective dielectric constant. The unit cell's self-resonance frequency changes with the change in the capacitance of the varactor. Modifying the biasing voltage also allows the equivalent permittivity to be tuned, for example at 2 GHz, it should theoretically change from 8 to 16 when the voltage is 25V and 12.25V respectively. The varactor has a small effect on the dielectric loss tangent in frequency regions out of the resonance zones.

Each figure indicates a series resonance, which is mostly due to the varactor's enormous series capacitance and inductance. As the varactor behaves like an inductor, the simulated effective dielectric constant is negative following the resonance, as seen in Fig. 2.2. This effect will be extensively used to stop the wave propagating through it, as opposite to what happens when it is positive. There is a significant amount of loss around resonance, as shown in Fig. 2.3. Therefore, it is recommended to bias the varactor to have the resonance point sufficiently away from any frequency of interest. The dielectric loss tangent turns negative after the resonance, yet this still indicates loss because the effective dielectric constant is now negative.

The magnetic constant and magnetic loss tangent are illustrated in Figs. 2.4 and 2.5, respectively. The magnetic constant is greater than unity because of the enhanced series inductance of the metal cross structure of unit cell. The magnetic loss tangent shown in Figure 2.5 shows a non-zero value due to the metallic losses in the structure of unit cell. It becomes negative as we increase the frequency. There is a power loss when magnetic and dielectric loss tangent are combined.

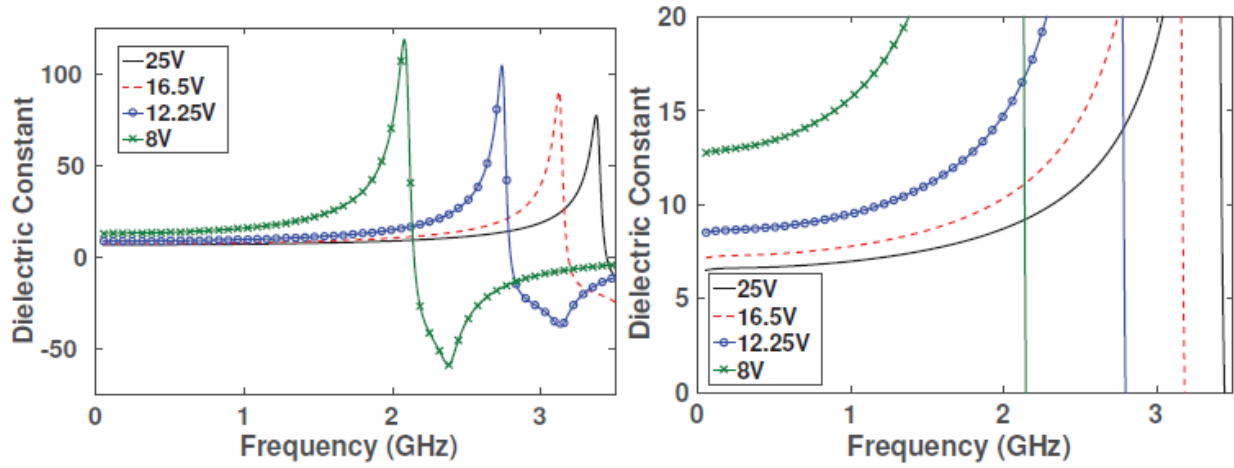


Fig. 2.2. Simulated effective dielectric constant of unit cell when the biasing voltage changes from 8 to 25V [1]

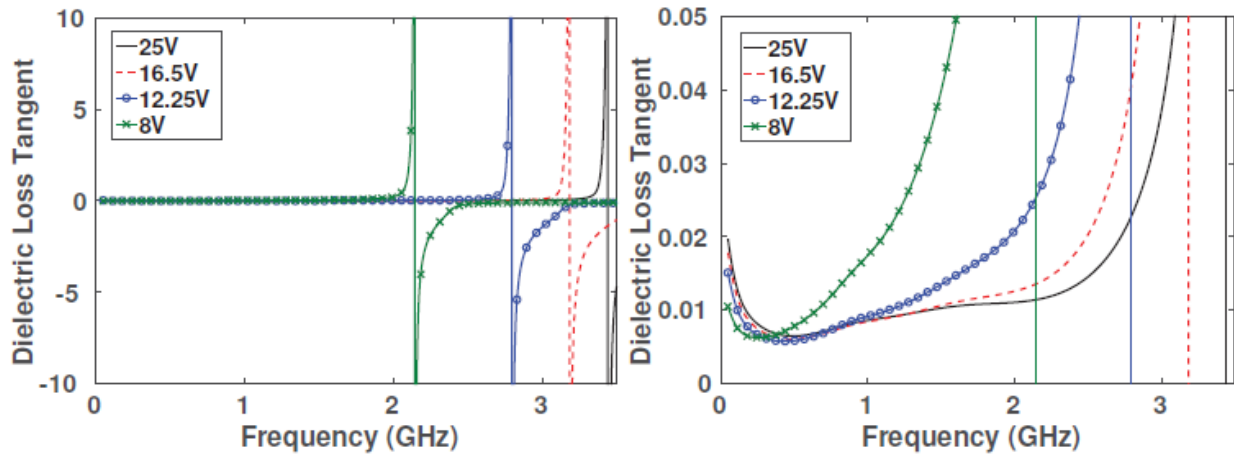


Fig. 2.3. Simulated effective dielectric loss tangent of unit cell. [1]

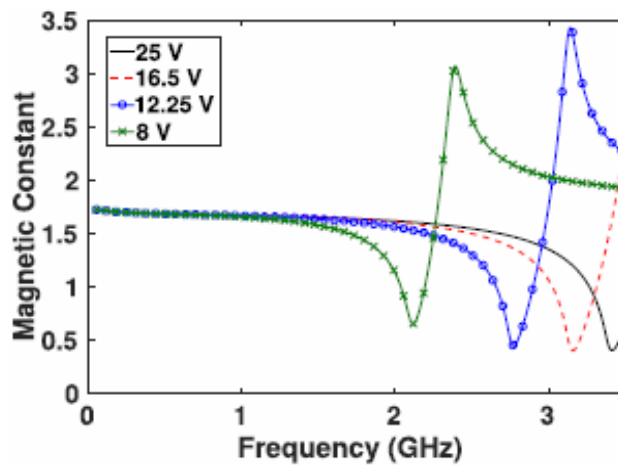


Fig. 2.4. Simulated effective magnetic constant of unit cell. [1]

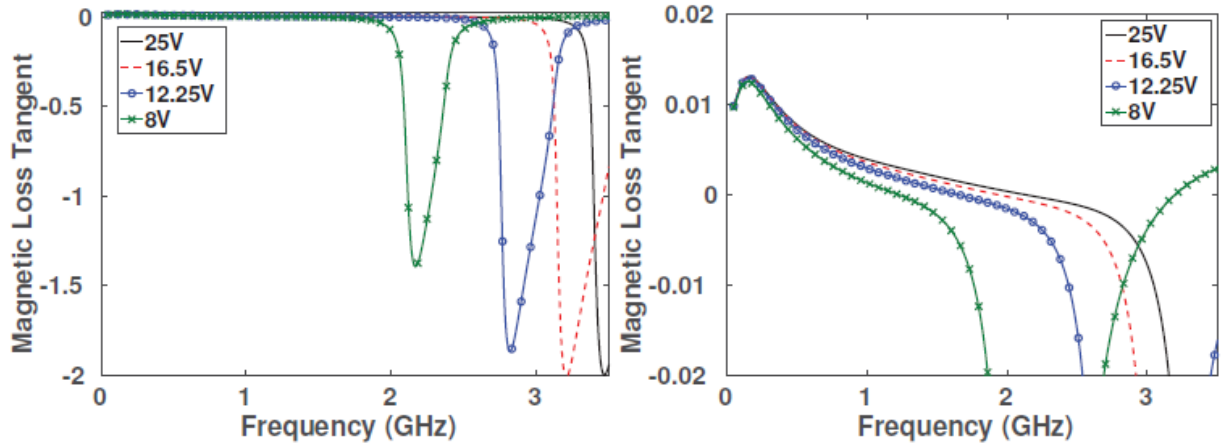


Fig. 2.5. Simulated effective magnetic loss tangent of unit cell. [1]

At 0.9 GHz, a bias of 0 V produces a maximum negative dielectric constant as seen in Figure 2.6. The losses for the negative permittivity cell are relatively large. The losses are primarily caused by the varactor's 1.8Ω series resistance when biased at 0V. However, the loss is manageable when this material is utilized to create a waveguide. This is due to the fact that the majority of electromagnetic energy is focused in materials with a positive dielectric constant rather than those with a negative permittivity.

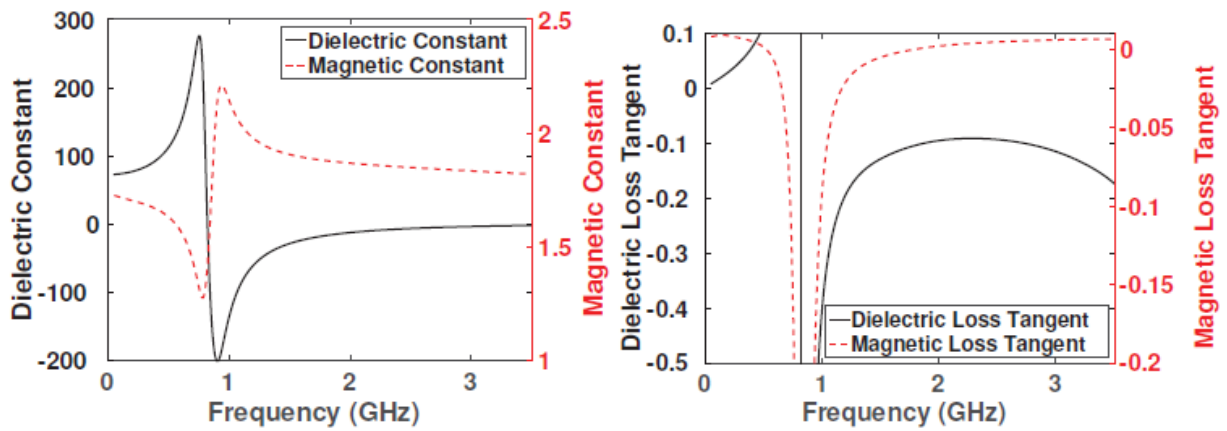


Fig. 2.6. Simulated effective properties of unit cell when biased at 0 V. [1]

These material properties show that this unit cell can operate at typical frequencies ranging from 0.9 to 3 GHz based on the previous activities made with this device. In this frequency band, it can provide either a negative dielectric constant (Fig. 2.6) when biased at 0V, or a positive value when biased at 25V (Fig. 2.2). When the biasing changes from 8 to 25V, it is possible to tune the positive dielectric constant of cell at a given frequency but the resonance also changes with the biasing so we have to be careful about this effect. The following section elaborates on the construction of the FPMS using the unit cells and the different components realized using the FPMS.

2.3 Field Programmable Microwave Substrate (FPMS)

FPMS is made up of 256 unit cells (described in the previous section) arranged in a 16x16 matrix as shown in Figure 2.7. The outer dimension of a single unit cell in this arrangement is 5.08mm \times 5.08 mm that gives the total dimension of FPMS 81.28mm \times 81.28mm. The actual FPMS board used for the measurement is shown in Figure.2.8. To connect to the FPMS implemented on the FR4 substrate, a microstrip to SIW transition is used which makes total dimension of the circuit board 314.45mm \times 293.62 mm. The FPMS is programmed with a bit stream sent to the HV57908PG-G chips from an FPGA. MATLAB is used to communicate with the FPGA and the power supply. The power supply controls the bias on all varactors. The device has three ports connected to a Vector Network Analyzer. Different types of waveguides and tunable filters implement using FPMS are discussed in the next sub-sections.

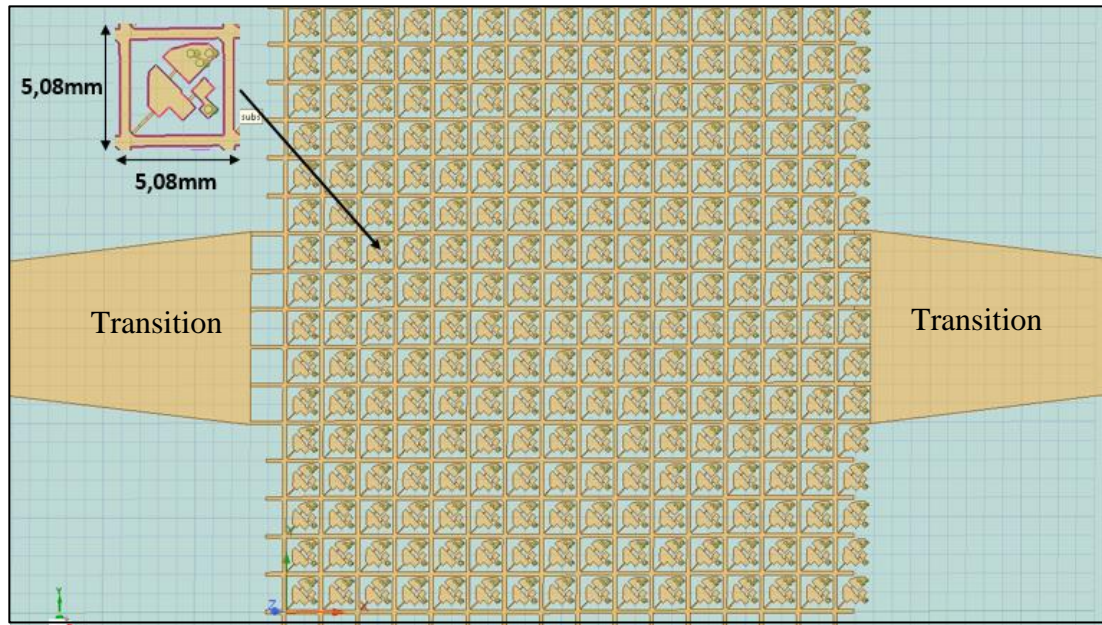


Fig. 2.7. HFSS model of FPMS

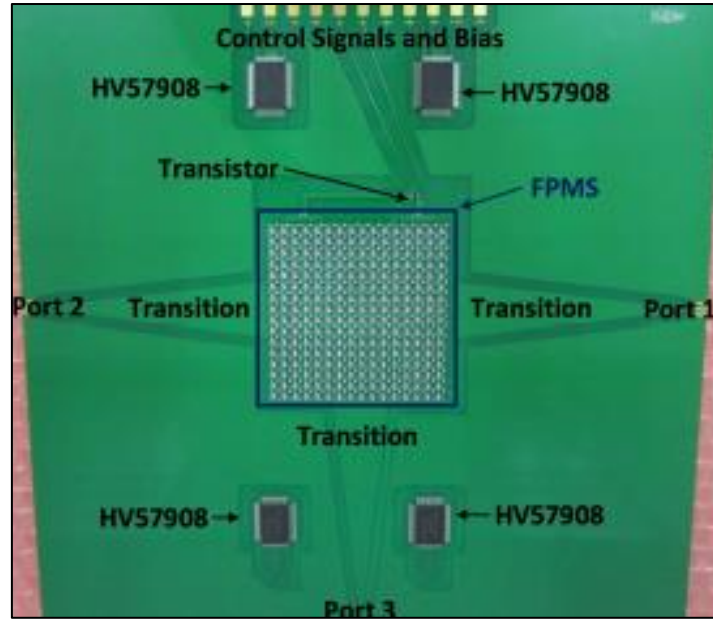


Fig. 2.8. FPMS circuit board [1]

2.3.1 Programmable Waveguides

In this section, a waveguide is realized using the FPMS. As explained in the previous section the substrate consists of small unit cells that can be programmed to have a range of positive or negative dielectric constant by varying the biasing voltage of the varactors. When the unit cell is biased to voltage from 8V-25V, it has a positive dielectric constant (ON state) for the frequency up to 3 GHz and when it is biased to 0V, it has negative dielectric constant (OFF state) for the frequency greater than 0.9 GHz. This substrate is contained in a metal parallel plate structure. Thus, programming a positive dielectric material core sandwiched between two negative dielectric material sidewalls results in a waveguide that behaves in a way that is described by the slab waveguide equations.

Three different width waveguides were depicted in Figure 2.9 in which the orange squares represent unit cells with 25V bias varactor (ON cells with positive dielectric constant) and blue squares represent unit cell with 0V bias varactor (OFF cells with negative dielectric constant). Thus, a waveguide has been created by turning ON a wide line of cells surrounded by OFF cells. The measured insertion loss and return loss for a six cells wide waveguide shown in Figure 2.10 between the frequency range 1.5 and 3GHz are 4 dB and 8.5dB respectively. The lower cut off frequency of this waveguide is decided by the OFF cells as they have effective permittivity positive below 0.9 GHz. The experimental value for lower cut off frequency is higher because of fabrication losses and imprecise material values. And the higher cut off frequency is due to the ON cells which have effective permittivity negative beyond 3GHz. By changing the width of waveguide, there is almost no change in the lower and upper cut off frequency of the waveguide as evident in Figure 2.11(a) but as we decrease the biasing voltage of ON cells, the

upper cut off frequency of the waveguide reduces as shown in Figure 2.11(b). This is because when the varactors are biased at lower voltage value, its series resonant frequency decreases (see Figure 2.2).

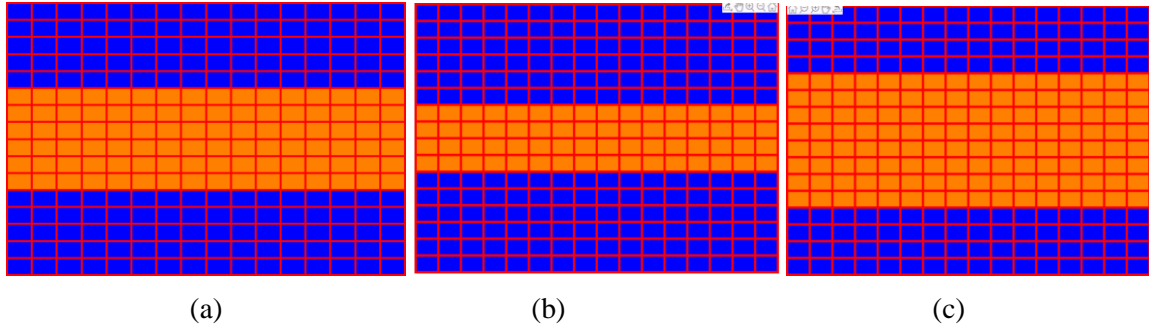


Fig. 2.9. FPMS waveguide (a) Six cells wide, (b) Four cells wide and, (c) Eight cells wide

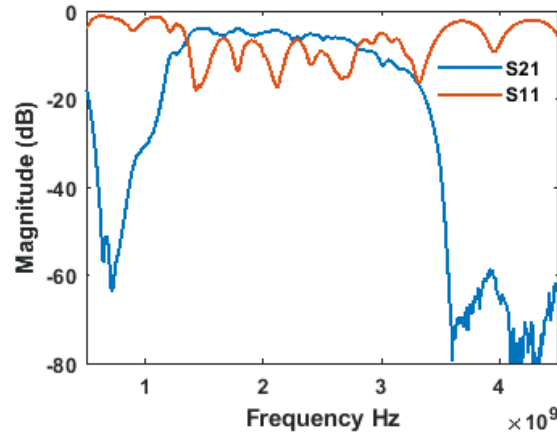


Fig. 2.10 Measurement results of six cells wide FPMS waveguide

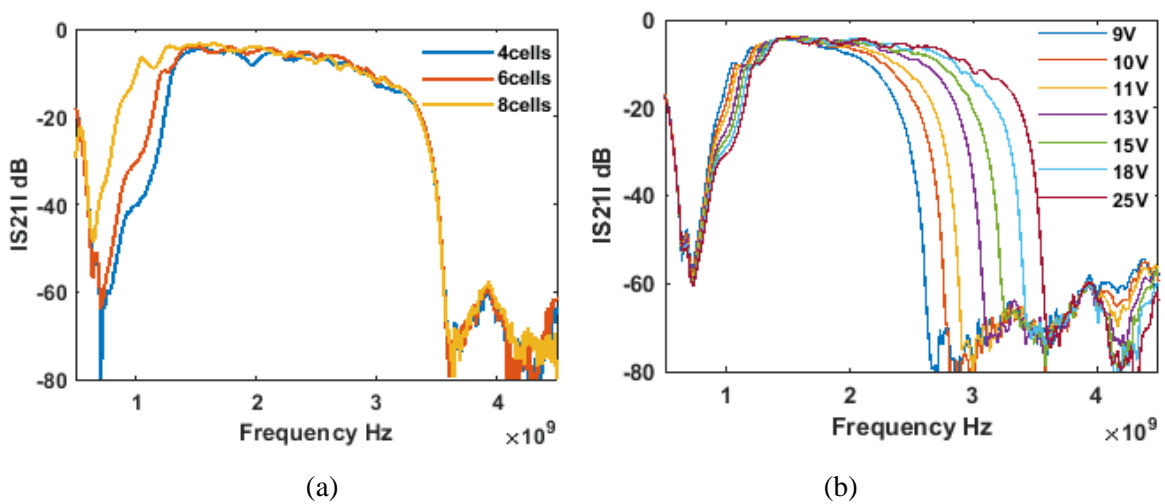


Fig 2.11. Measured insertion loss (a) For different width of waveguide and (b) For same width and different biasing voltages of ON cells

The low return loss observed in these components is caused by a non-optimal microstrip to FPMS transitions in the current FPMS board. The effective loss tangent as seen in Figure 2.3 of all the ON unit cells in the waveguide structure are one of the main source of the losses measured in the waveguide off band. The varactors used in the current FPMS board have a parasitic resistance of 1.8Ω that cause significant amounts of loss as well. Also, the cells with negative permittivity value contribute to the loss. This information is important to know about about the physical limitations of FPMS board and therefore it has been considered while applying the optimization algorithms in the next section of this manuscript.

2.3.2 FPMS Robustness

Microwave components are very often susceptible to failures and it is very difficult to design a hardware which can still work with slightly degraded performance. FPMS is one such device which is robust to random unit cell failures. In Figure 2.12, orange cells are ON (biased to 25V), blue cells are OFF (biased to 0V) and red cells are random failures which cannot be turn ON and therefore remain OFF. Despite of these random failures at random locations, it still allows signal to travel from port 1 to 2 until the size of theses holes are much smaller than the wavelength as shown in Figure 2.13. If a connected row of OFF cells occurs in the middle of the waveguide, then a critical failure will appear. It will create a wall of cells with a negative dielectric constant that will block the signal from propagating through the ON cells.

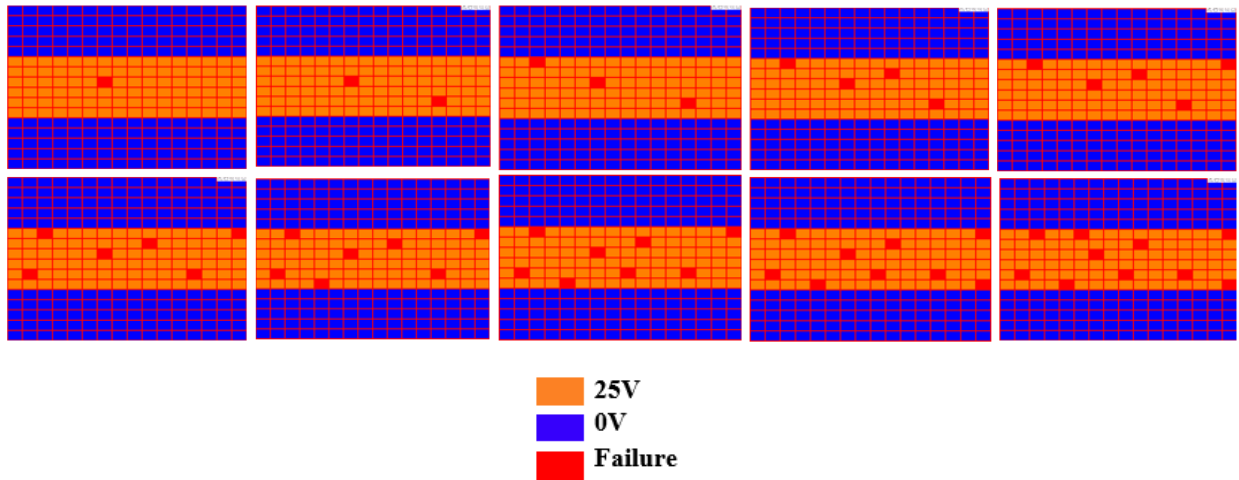


Fig. 2.12. Random failure in FPMS waveguide ranging from 1, 2.....,10 unit cells

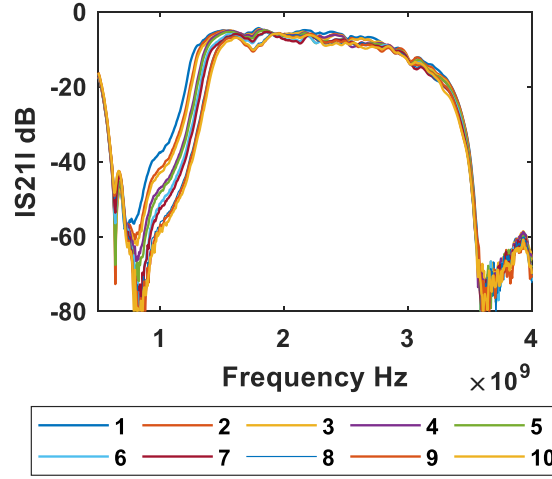


Fig. 2.13. Measured Insertion loss in case of random failures from 1,2,...,10 unit cell

2.3.3 FPMS Filter

In FPMS technology, tunable filters can be achieved by tuning the positive dielectric constant of ON cells or by varying the length or width of the metal interconnects in the unit cell. This allows for real-time tuning of the filter response, improving the performance and versatility of a communication system. FPMS technology provides several advantages in the implementation of tunable filters, including reduced development time, low cost, and greater design flexibility. Additionally, the ability to reconfigure the microwave circuits in real-time makes it possible to quickly adapt to changing system requirements, improving system performance and reliability.

FPMS is demonstrated as reconfigurable microwave filters with tunable center frequencies, bandwidth and filter orders in [2]. A schematic of a FPMS waveguide band pass filter is shown in Fig. 2.14. [2]. A resonator cavity in a conventional filter is implemented using unit cell lattice with a length of a half wavelength. Coupling iris between cavities is equivalent to coupling unit cells between cavities biased at different positive voltages. FPMS cavity boundaries are built by arranging 0V-biased unit cells on two sides of waveguide unit cells. In a conventional waveguide filter, I/O coupling and inter-resonator coupling are controlled by enlarging or reducing the size of irises; whereas in the FPMS counterpart, couplings are tuned by varying the bias voltages of coupling unit cells. The measurement results of the FPMS waveguide band pass filter are shown in Figure.2.15. [2]. The insertion loss from measurement is 9.12 dB at the filter center frequency because of the different source of losses already mentioned and are related to the bandwidth and return loss of the created filter.

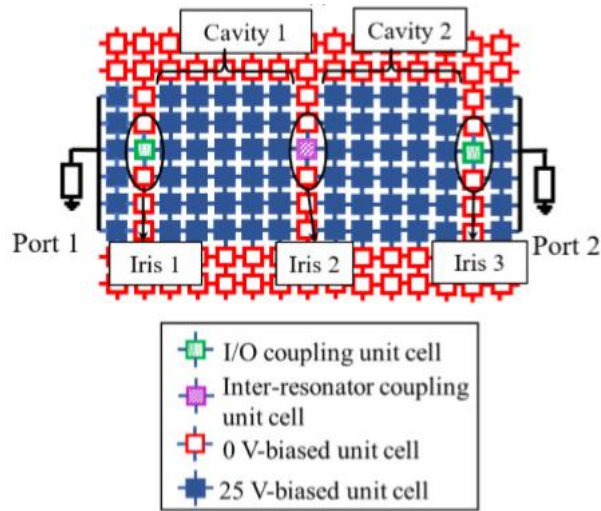


Fig. 2.14. FPMS waveguide band pass filter [2]

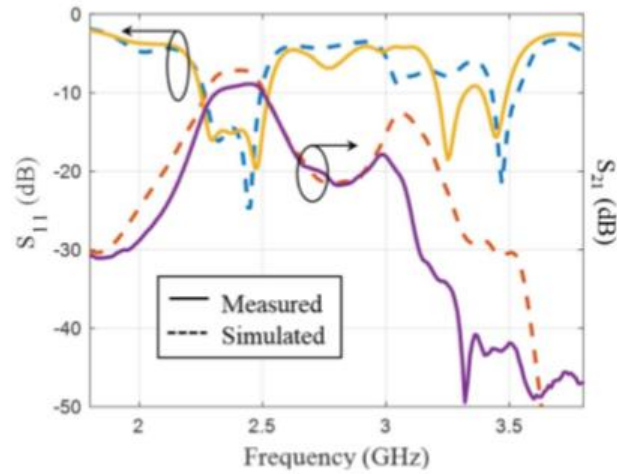


Fig. 2.15. Measured results of the FPMS waveguide band pass filter [2]

The measurement results for tunable center frequency and tunable bandwidth are shown in Figures 2.16 and 2.17. It is clearly visible that as we increase the biasing voltage of unit cell of cavities, the center frequency increases. As mentioned earlier (Figure 2.2) that increase in the biasing voltage of unit cell decreases its effective permittivity and hence increases the center frequency.

The filter bandwidth can be tuned by varying the bias voltages of coupling unit cells acting as coupling irises. The individual biasing of coupling unit cells for this measurement has been done manually. The current generation of FPMS only permit to turn ON or OFF each cells and all the ON cells can have same biasing voltage. In the next section, we will be using this way of working considering only the regular operation possible with the FPMS board.

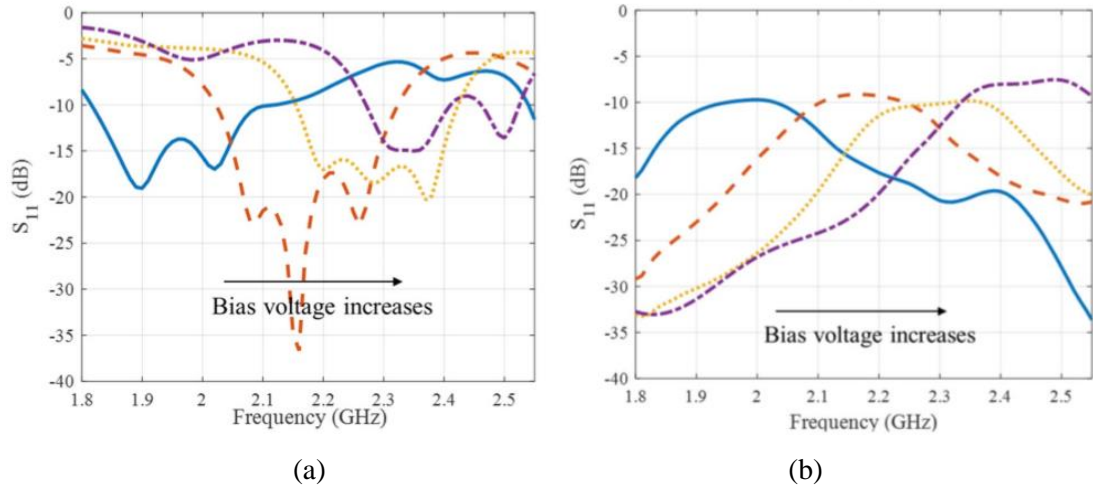


Fig. 2.16. Measurement results of the filter when its center frequency is tuned (a) $|S_{11}|$ (b) $|S_{21}|$ [2].

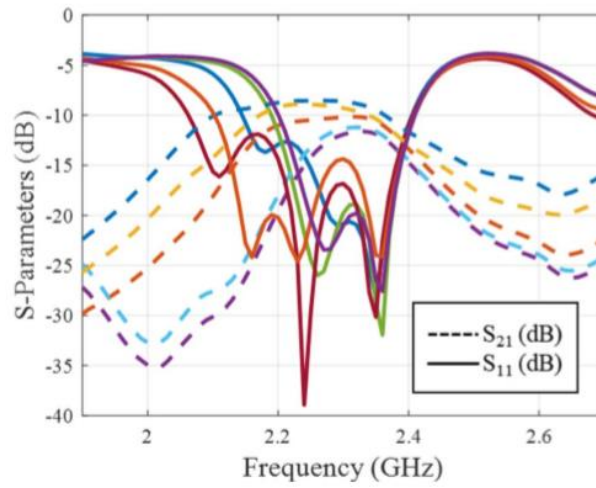


Fig. 2.17. Measurement results of the filter with tunable bandwidth [2]

In this section, we manually optimized different types of waveguides and tunable filters implemented using the FPMS. However, due to the high degree of reconfigurability and complexity of the FPMS matrix, a more advanced optimization using modern software tools is necessary to achieve the best possible performance for such devices. One such tool is described in the next section.

2.4 FPMS ADS Model Optimization

In this section, optimization tool has been applied to an electrical equivalent model of FPMS developed using ADS in order to get the envisioned devices such a phase shifter, power divider etc. using FPMS with best possible performances. An ADS-MATLAB interface has been created to make the process simpler and more efficient.

2.4.1 ADS-MATLAB Interface

The FPMS concept relies on discrete cells (pixels) that can be turned ON (positive dielectric permittivity) and OFF (negative dielectric permittivity). Using a genetic algorithm, the unit cells of FPMS can be either turned ON or OFF to meet the given specifications in terms of S-parameters.

As, it is difficult to create 16x16 matrix in ADS and also to manage the biasing of each and every cell when we have large matrix. Therefore, we have created an ADS-MATLAB interface. A code in MATLAB has been implemented which can create any size of matrix of FPMS unit cells (for example 100 cells by 100 cells and more) easily by just giving the value of the input named “dimension of matrix”. Also, the number and location of input and output ports can be set. This code can use any kind of cell, is compatible with the current generation and will be compatible with the future generations of FPMS.

The developed MATLAB code first asks the user for the inputs as shown in Figure 2.18. Then, it creates the netlist.log file for selected matrix, which will be used by ADS solver remotely using MATLAB only. ADS runs the simulation of the matrix based on an equivalent model of the unit cell shown in Appendix 1. (ADS simulation does not include the effect of transitions). After simulation a S-parameter file is created which is recovered by our code. Then, we can load the S-parameter file and perform optimization in MATLAB. If the optimization is good enough for the desired frequency, we stop there and plot the final S-parameters. And if there is a possibility of further improvement we will continue the optimization process and each time the biasing voltage of the cells will be updated. Here, the optimization variables are the voltages applied to each unit cell’s varactor and therefore the capacitance provided by them. In other words, the code provides each cell biasing that make the FPMS meet (as much as it can) the frequency specifications defined as ideal goals for the optimizer.

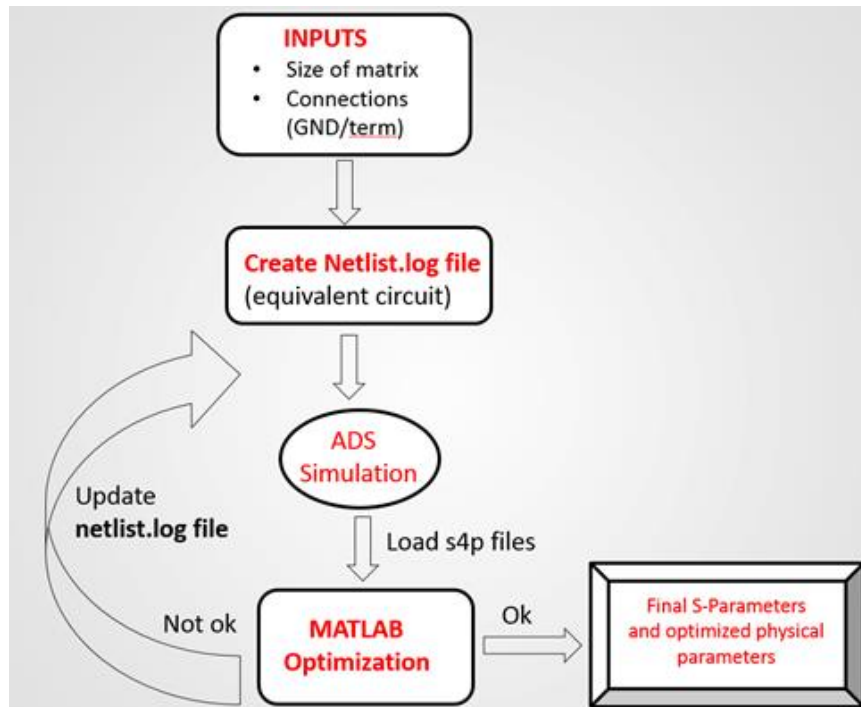


Fig. 2.18. Different blocks of ADS/MATLAB Interface

There are several other advantages of using MATLAB such as:

- The modular environment of MATLAB and a user friendly interface. It is easier to implement and test the algorithms.
- It has a large database of built in algorithms.
- It gives the user access to more information coming from the optimization algorithm, less time for the optimization compared to ADS, more flexibility to switch from one optimization tool to another. Ultimately, it will improve the performance of FPMS.

As we know, ADS generates a netlist.log file when we draw any schematic and then it simulates its behavior as a function of frequency and other physical parameters (biasing of varactors, etc). This netlist.log file basically contains all the information about components in the ADS schematic and their connections with each other. This netlist.log file can be divided into three parts for the purpose of understanding

- **Components of Unit Cell:** This blocks contains the components of ADS equivalent circuit of a unit cell with all the properties for example, dielectric permittivity of substrate, tangent loss, thickness etc. as described in Appendix 1.

- **Connections of Unit Cell:** This block contains the information about the number of cells and their connections with each other and the ports (Term1, Term2, Term3 and Term4) through Node number. It also details whether the particular cell is ON/OFF and the biasing voltage value of ON cells.
- **Simulation block:** A last block details the S-parameters specifications such as start and stop frequency for the simulation as well as the step size.

Through our MATLAB code we generate this netlist.log files and send it to ADS for simulation. The complete netlist.log file for a 3x3 FPMS matrix is described in Appendix 2.

2.4.2. MATLAB Graphical Interface

When we generate the netlist.log file with the MATLAB code, ADS can simulate it but cannot display the equivalent schematic. Therefore, in order to visualize the generated matrix, we have developed a graphical interface in MATLAB. The graphical interface has three panels: design, simulation, and optimization which is shown in Appendix 3. The design panel is used to define the initial biasing voltage of each unit cell arranged in a 16*16 matrix same as the actual FPMS board. It has to be mentioned that the program can be set to work with any number of cells and ports. One can select any number of rows and columns on the design panel for the simulation. Different colors for unit cell are used to show different biasing voltage. For example, blue is used for 0V biasing (OFF state) and orange is used for 25V biasing (ON state). We can save any configuration on the design panel and load it whenever it is required. The code also allows us to choose cells for the optimization step if we want to reduce the number of variables.

Then in the simulation panel, one can plot the S-parameters response of the configuration defined on the design panel. It is divided into two parts, one for magnitude and another for phase of S-parameters.

Finally, the optimization panel, allows to choose the optimization algorithm, define the S-parameters constraints on magnitude or phase (or both at the same time) and then start the optimization process. The code also allows us to choose the number of iterations for the optimization algorithm. This algorithm then alters the biasing of unit cells and stops once the goals on the S-parameters are achieved. The constraints can be put either on magnitude or phase or both. It will return the final S-parameters and optimized voltages of unit cells on the optimization panel and design panel of graphical interface respectively. One can also stop the optimization process in between if it is observed that goals are almost achieved (slightly different from what was asked). The optimization algorithm will stop either if the goals are satisfied or maximum number of iterations have been done. After optimization has been done, the results can be easily saved using the save button on the design panel.

The different optimization algorithms that can be used on the equivalent model of FPMS is discussed in the next section.

2.4.3 Optimization Algorithms

The current generation of the FPMS board (existing hardware) allows us to switch the cells state only between two values either ON or OFF. Therefore, for the current generation only genetic algorithms can be used but for the future generation, the developed code also includes Nlopt optimization algorithms, which are used for continuous optimization. Nlopt algorithms are however studied here as it can be used on the ADS equivalent model of the FPMS which virtually allows to individually bias each unit cell with any voltage value between 0V to 25V without the limitations of the current hardware.

Genetic Algorithm [3]

The genetic algorithm (GA) was first introduced by Holland in 1975, and it has become a very popular method for solving many optimization problems with multiple local optima in various fields of application. To reach the global optimum, this method explores the admissible search space to choose the best performing regions.

In general, GAs are function optimizers, i.e. methods for finding the optimum of the objective function (x) where the elements x_i of the vector $x = (x_1, x_2, \dots, x_n)$ are binaries. The GA begins by randomly generating an even number p of binary strings of length n to form an initial population. In the electromagnetic community, function optimizers of all types are mainly used in design and in solving inverse problems. In design problems, the parameters x_i describe the main features of a design and (x) is a measure of system performance to be maximized or minimized. GAs differ from most traditional optimization methods in two ways. First, they don't necessarily act directly on the design parameters x , and second, they simultaneously optimize entire populations of solutions.

Nlopt Algorithms [4]

Nlopt is an open source library for nonlinear optimization that is callable from MATLAB. It can support large scale optimization with thousands of constraints. These algorithms are derivative free and only uses the function values. Some of the Nlopt optimization algorithms that can be used (for simulation purpose only) have been briefly explained here.

- DIRECT and DIRECT-L: DIRECT is the Dividing RECTangles algorithm for global optimization and DIRECT-L is the "locally biased" variant. These are deterministic-search algorithms based on systematic division of the search domain into smaller and smaller hyperrectangles. These algorithm is more biased towards local search so that it is more efficient for functions without too many local minima. NLopt contains several implementations of both of these algorithms. The DIRECT and DIRECT-L algorithms start by rescaling the bound constraints to a hypercube, which gives all dimensions equal weight in the search procedure. Most of the above algorithms only handle bound constraints, and in fact require finite bound

constraints (they are not applicable to unconstrained problems). They do not handle arbitrary nonlinear constraints.

- COBYLA (Constrained Optimization BY Linear Approximations): This is a derivative of Powell's implementation of the COBYLA (Constrained Optimization BY Linear Approximations) algorithm for derivative-free optimization with nonlinear inequality and equality constraints. It constructs successive linear approximations of the objective function and constraints via a simplex of $n+1$ points (in n dimensions), and optimizes these approximations in a trust region at each step.
- BOBYQA: BOBYQA performs derivative-free bound-constrained optimization using an iteratively constructed quadratic approximation for the objective function. Because BOBYQA constructs a quadratic approximation of the objective, it may perform poorly for objective functions that are not twice-differentiable. The NLOpt BOBYQA interface supports unequal initial-step sizes in the different parameters (by the simple expedient of internally rescaling the parameters proportional to the initial steps), which is important when different parameters have very different scales.
- PRAXIS (PRincipal AXIS): PRAXIS" gradient-free local optimization via the "principal-axis method. This algorithm was originally designed for unconstrained optimization. In NLOpt, bound constraints are "implemented" in PRAXIS by the simple expedient of returning infinity (Inf) when the constraints are violated (this is done automatically—you don't have to do this in your own function). This seems to work, more-or-less, but appears to slow convergence significantly.

Table 2.1 gives advantages and disadvantages of the different algorithms that can be used for the optimization in different cases as per the mentioned specifications. In the next section, we will use the optimization algorithms discussed above to test on the ADS equivalent model of FPMS in order to get the overview of what can or can't be achieved using the FPMS.

Table 2.1: Comparison of different optimization algorithms

Algorithm	Pros	Cons
Genetic	Large no. of variables can be considered Applicable to both linear and non-linear constraints	More no. of iterations are required
DIRECT	Large no. of variables can be considered	More no. of iterations is required Applicable to linear constraints only
COBYLA	Less no. of iterations is required Applicable to both linear and non-linear constraints	Large no. of variables can't be considered
BOBYQA	Unequal initial step size can be considered	Poor performance due to quadratic approximation
PRAXIS	Less no. of iterations are required	Applicable to unconstrained optimization

2.5 FPMS Devices

Here, we present the high frequency devices that can be made by combining FPMS capabilities and the optimization tools discussed in the previous section. A 3-port power divider with equal and different power distribution, a phase shifter and a tunable notch are described in the next sub-sections. These examples are tested using the ADS equivalent model and genetic optimization algorithm is used for all the cases.

2.5.1 3-port Power Divider

A 3-port power divider splitting equal power is implemented using the FPMS. The performance of the power divider is not that good initially as one can see through Figure 2.19(a) but it can be improved using the optimization techniques. The goal is to find the optimal configuration of ON or OFF cells (using genetic algorithm) of the FPMS circuit that satisfies our specifications based on the S-parameters. It is very much similar to shape optimization techniques which improves the performance of a device by changing its topology and ultimately gives the optimal solution based on the calculation of cost function [5].

In this case, the genetic algorithm modifies the biasing voltage of a unit cell based on the S-parameter response of the device. Instead of considering all 256 unit cells for optimization, we have considered few cells in the center first to reduce time for optimization. If it does not work, we can consider more number of cells for optimization. The constraints provided to the optimizer for equal power distribution are magnitude of S_{21} and S_{31} should be equal and greater than -5dB and magnitude of S_{11} should be less than -15dB between 1.7 to 2.7 GHz. The optimized structure of the power divider and the corresponding S-parameters are shown in Figure 2.19(b). The goals have been clearly accomplished by the optimization algorithm and it took 18 iterations and 126 seconds on a regular laptop.

Similarly, the constraints are provided for the unequal power distributions for a power dividing ratio of 1: 2. The magnitude of S_{21} should be greater than -4dB, magnitude of S_{31} should be greater than -8dB and magnitude of S_{11} should be less than -12dB between 1.7 to 2.7 GHz. Figure 2.20 shows the simulated results for the unequal power distribution. The optimization is quite successful again.

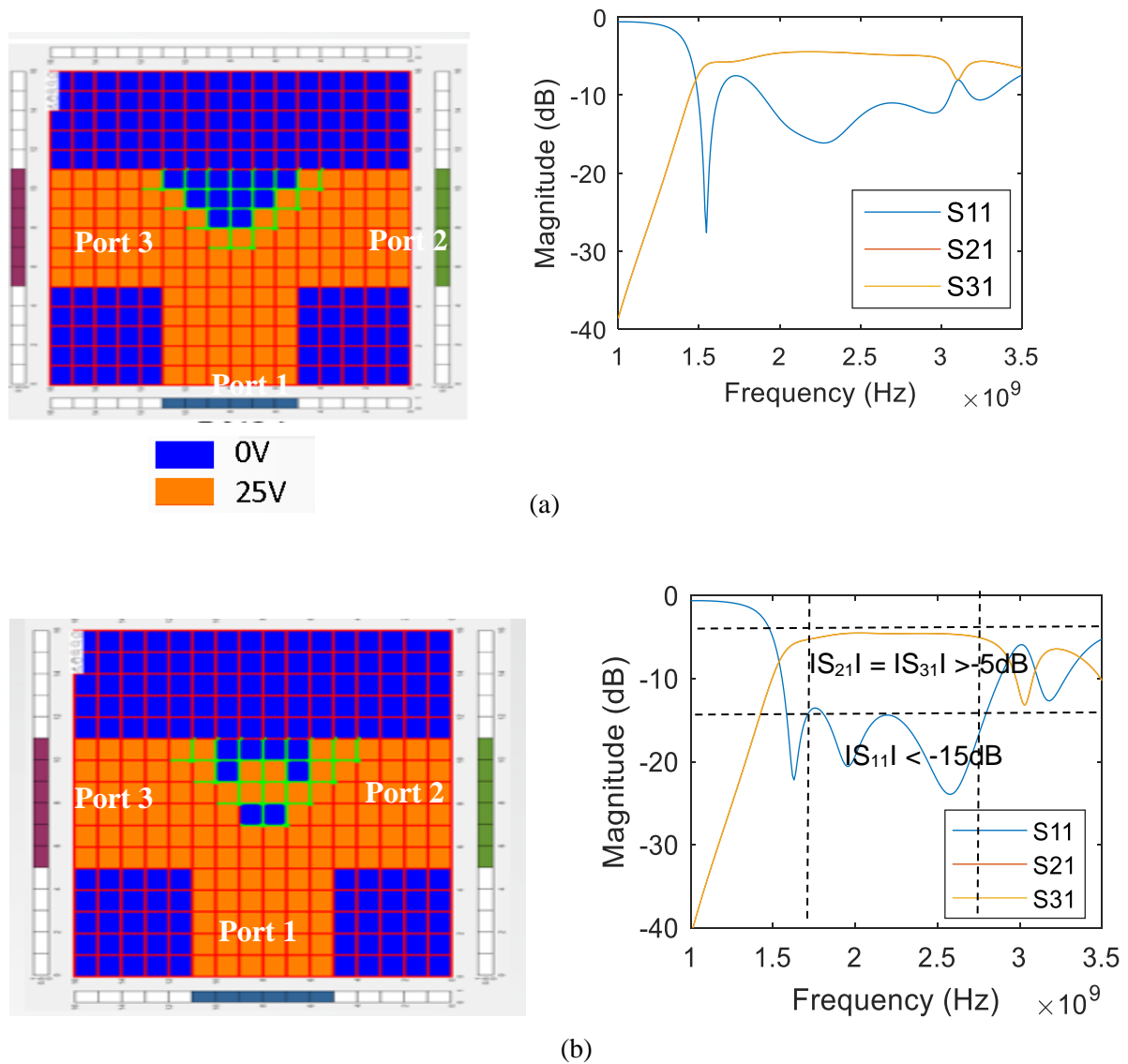


Fig. 2.19. Power Divider with equal power distribution (a) initial structure and simulated S-parameters, (b) optimized structure and simulated S-parameters

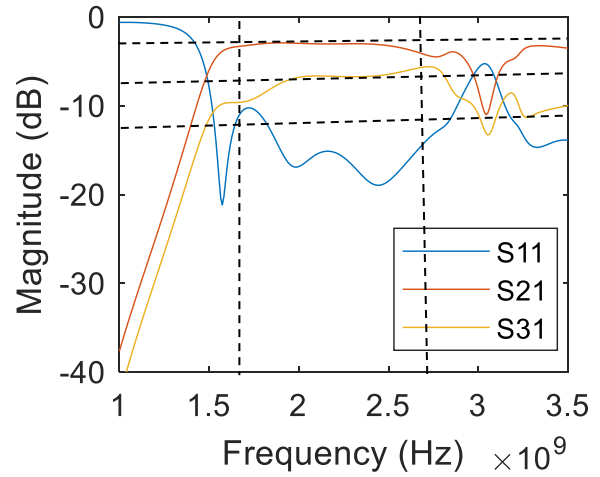
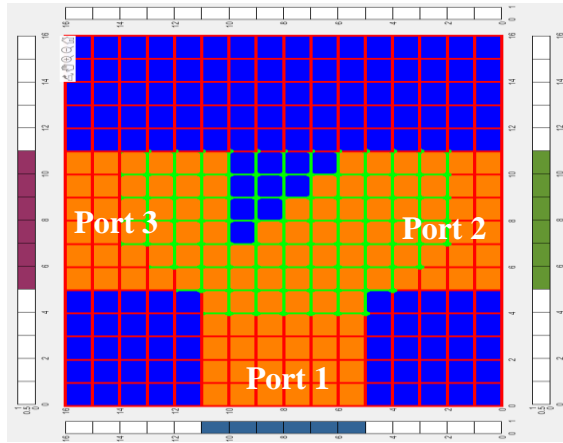


Fig. 2.20. Power Divider with 1:2 dividing ratio and simulated S-parameters

2.5.2 Phase Shifter

Phase shifting can be obtained from the straight waveguide configurations using the genetic optimization algorithm. In this method, the ON unit cells are biased to 25V for all the cases. To achieve the required phase shift different constraints were added to the phase of S_{21} for the straight waveguide case at 1.5GHz. Initially for the structure 1 depicted in Figure 2.21(a), phase of S_{21} at 1.5 GHz is -190° . Then we ask the optimizer to increase the phase by 20° at 1.5 GHz while keeping the same magnitude for S_{21} and we obtained structure 2. It took 25 iterations to achieve the goal. Taking the structure 1 again as initial configuration and choosing different cells for optimization, we ask the optimizer to increase the phase by 45° at 1.5 GHz while keeping the same magnitude for S_{21} and we obtained structure 3. It took 22 iterations to achieve the goal. The magnitude and phase of S_{21} for the three structures are shown in Figure 2.21(b). Phase shifting assisted by the optimization algorithm is thus possible.

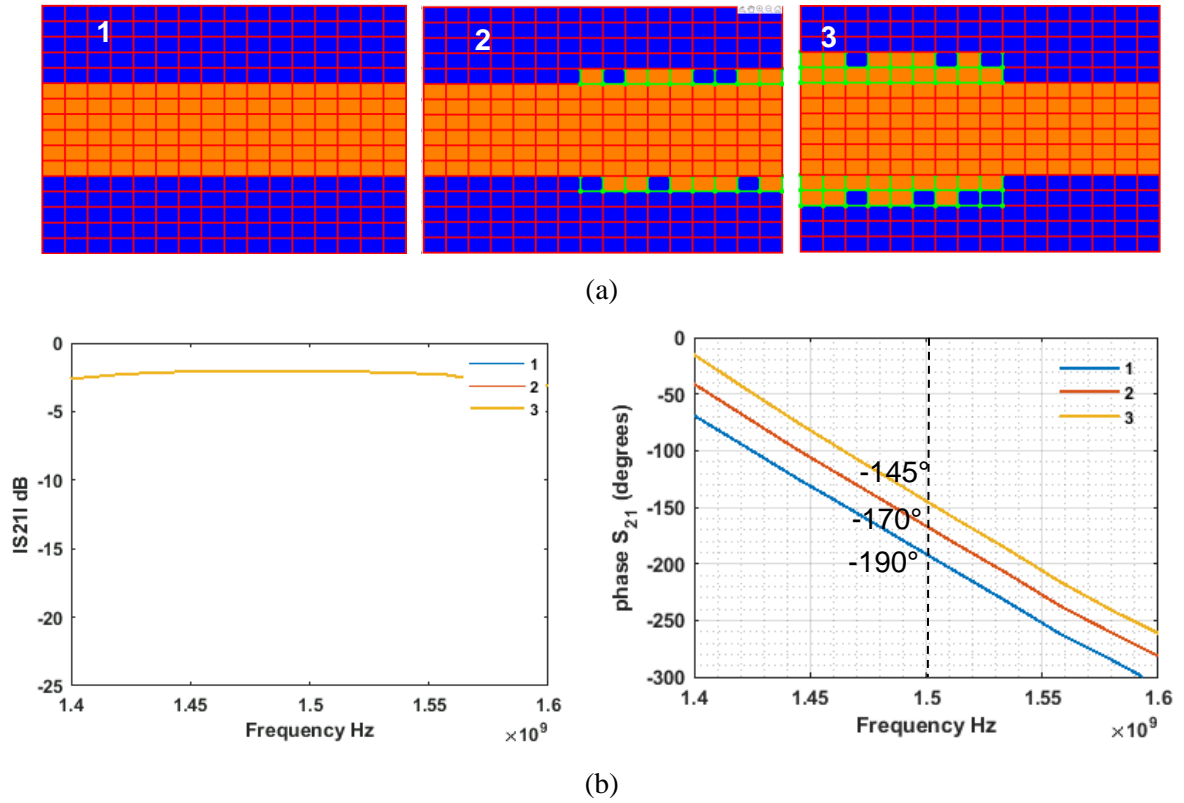


Fig. 2.21. (a) Optimized waveguide based structures to obtain phase shifter and (b) Simulated S-parameters.

2.5.3 Tunable Notch

The FPMS can be used to create a tunable notch by turning on specific unit cells on either side of a waveguide, creating a locally adjustable stub. The size and position of the stub can be changed by using the optimization algorithm. To achieve this, the unit cells are selected for optimization on one or both sides of the waveguide and the desired notch frequencies are specified as goals for the optimizer. Notch is obtained at 1.64 GHz and 1.77 GHz respectively, with a S_{21} magnitude lower than -12 dB making it another function that can be optimized with the FPMS.

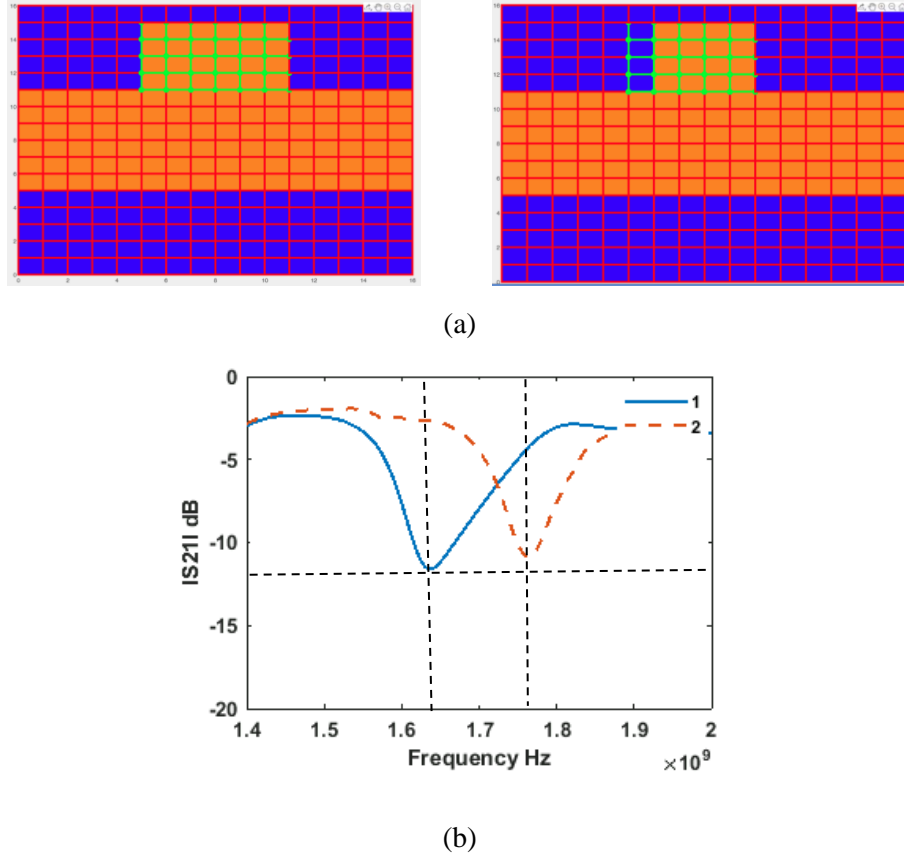


Fig. 2.22. (a) Optimized structures for tunable notch and (b) Simulated S-parameters

2.6 Conclusion

In this chapter, the unit cell, which serves as the building block for the FPMS, is explained in detail along with its various components. The properties of the unit cell, specifically its dielectric and magnetic constant, are discussed in relation to the biasing voltages of the varactors. Based on these properties, the operating frequency range of the FPMS is determined to be 0.9 to 3 GHz. ON and OFF cells can thus be created, providing respectively a local positive and negative equivalent dielectric constant. By arranging these cells, it is possible to create waveguides and filters whose properties (bandwidth and center frequency) can be tuned. The tested cases with the Canadian partners were manually adjusted so far by changing cell behavior (ON or OFF).

A MATLAB-based optimization tool was therefore introduced to enhance the performance of complex functions realized with the FPMS. The optimization process was first carried out on the equivalent FPMS model built in ADS, and the successful implementation of the ADS-MATLAB interface allowed for remote use of the ADS solver via MATLAB code. The MATLAB graphical interface enabled visualization of the FPMS matrix and made the simulation and optimization steps clear and straightforward. Various optimization algorithms were briefly described for the realization of

different components. With the current FPMS hardware (1st generation), only genetic algorithms can be applied since the cells can be either ON or OFF. The equivalent electrical model can however let us virtually and individually optimize each unit cell's biasing voltage and more kinds of optimization algorithms can be used with MATLAB.

By combining the FPMS and the MATLAB optimization tool, more diverse high-frequency devices were simulated, including a 3-port power divider with equal and unequal power distribution, a phase shifter, and a tunable notch. The goals (S-parameter specifications) were successfully achieved using the genetic algorithm with less than 30 iterations when optimizing about 25-30 cells within the whole matrix. Even if successful, these cases have shown that the time needed for optimization is clearly related to the number of cells to optimize. Due to the huge number of combinations if we ask the algorithm to tune the whole matrix (256 cells), a starting case defined by human is mandatory. The knowledge of the FPMS capabilities and limitations is also important to set goals for the optimizer that can be realistically met. In the next chapter, these optimization techniques will be directly applied to the actual FPMS board, demonstrating a real-time optimization method for realizing these components so that there is no discrepancy between simulation and measurement results.

2.7 References

- [1] N. Jess, B. A. Syrett, and L. Roy, “The Field-Programmable Microwave Substrate,” *IEEE Transactions on Microwave Theory and techniques*, vol 64, no. 11, pp. 3469–3482, Nov. 2016.
- [2] Hanyue Xu, Ying Wang, Farhan A. Ghaffar, and Langis Roy, “Reconfigurable Microwave Filters Implemented Using Field Programmable Microwave Substrate” , *IEEE Transactions on Microwave Theory and techniques*, vol. 69, no. 2, pp 1344-1354, Feb 2021.
- [3] D. S. Weile et E. Michielssen, “Genetic algorithm optimization applied to electromagnetics: a review”, *IEEE Transactions on Antennas and Propagation.*, vol. 45, no 3, p. 343-353, mars 1997, doi: 10.1109/8.558650.
- [4] https://nlopt.readthedocs.io/en/latest/NLopt_Algorithms/
- [5] Ali Dia, Christophe Durousseau, Cyrille Menudier, Ludovic Carpentier, Olivier Ruatta and Stephane Bila, “Shape Optimization Methods for the Design of Microwave Circuits and Antennas”, *2nd URSI AT-RASC, Gran Canaria, 28 May – 1 June 2018*

Chapter 3.

Optimized FPMS Devices

3.1 Introduction

This chapter presents novel designs of reconfigurable microwave components based on the concept of field programmable microwave substrate (FPMS). FPMS technology combined together with a live optimization method is used to demonstrate a power divider with tunable power dividing ratio, a tunable notch, a switch, a phase shifter and a programmable attenuator. The developed optimization technique is capable of changing the S-parameters response of the device according to the desired specifications. Thus, making it much simple and quick to realize different microwave functions with best performance achievable with the FPMS.

The optimization method uses a genetic algorithm developed in MATLAB specifically for the FPMS. This genetic algorithm changes the biasing voltages of varactors deployed in unit cells of FPMS according to the required S-parameters specifications. The optimization method uses the real measured S-parameters to get the most accurate results from the FPMS cell behavior. It is possible to use instead the FPMS equivalent model shown in the previous chapter. In that case this virtual twin is theoretically optimized and the output of this step, that is the biasing voltage of unit cells, are then sent to the actual FPMS. Even if possible and tested during this project, it was realized that the current board shows some slight but existing differences with the equivalent model. Another reason for this choice is that, as it will be explained in the next section, the automated process of retrieving the measured S-parameters from a remotely controlled VNA and sending a new configuration to the varactors is just as fast as using the ADS model instead. Therefore, it was more accurate to rely on measured S-parameters to run the device optimization. Using the equivalent model has still some merits like having a very useful tool for the development and test of the different optimization algorithms and many useful tests that can be done virtually. From a coding point of view, we have only replaced the ADS simulation part with a code that remotely drives the FPMS board and VNA. All that was previously described remains applicable here. All the steps to achieve the live optimization that is using real time measurements from a remotely driven

VNA on FPMS are explained in detail in the next section. Different examples are also presented to prove the efficiency of the developed optimization process.

Optimization strategies are also presented to reduce the number of variables to optimize, applying coarse and fine strategies on waveguides and 3 ports power dividers. New tunable RF functions compared to what was previously published in [1] and [2] have been tested and optimized. Switch, tunable notches, phase shifter and 3 ports power dividers that can be dynamically reconfigured to split the power from one port to two ports with a given amplitude ratio and out phasing between the two exit ports are presented. A discussion on such highly reconfigurable device is provided as well as a comparison with similar devices from the literature and a conclusion.

3.2 Live Optimization on FPMS

The FPMS board used for the measurement has been completely described in chapter 2. As stated previously, the current generation of the FPMS board allows us to switch the cells state only between two values either ON or OFF. Therefore, a genetic algorithm based on [3] has been developed in MATLAB that modifies the biasing voltage of the unit cell based on the S-parameter response of the device. The goal of the algorithm is to find the optimal configuration of the ON or OFF cells of the FPMS circuit that satisfies specifications based on the S-parameters, i.e. objectives given on the modulus and/or the phase of these parameters as a function of frequency. It is very similar to shape optimization techniques, which improve the performance of the device by changing its topology and ultimately give the optimal solution based on the calculation of a cost function [4]. Since the microcontrollers on the FPMS board can be driven remotely using a MATLAB driver and the measured S-parameters on the Vector Network Analyzer (VNA) can be easily imported to MATLAB as demonstrated in Figure 3.1, therefore it is possible to live tune the unit cells of the FPMS.

This method will provide most accurate set of data for the optimization algorithms and we can remove any discrepancy between simulation and measured results. There can be several factors that cause these differences in the results such as

- parasitic couplings when comparing the actual board and its theoretical model,
- slight differences in the voltage of each cell to make them produce the required equivalent capacitance values determined from a theoretical optimization,
- evolution of the board soldering over many years of use etc.

The different steps involved in this live optimization is shown in Figure. 3.2 and explained in the next paragraphs. The goal of the MATLAB algorithms and interface is to firstly measure an initial S-parameter response corresponding to the initial configuration of FPMS unit cells and to use a genetic algorithm which alters this configuration repeatedly to reach specified goals on the phase and amplitude of the FPMS S-parameters.

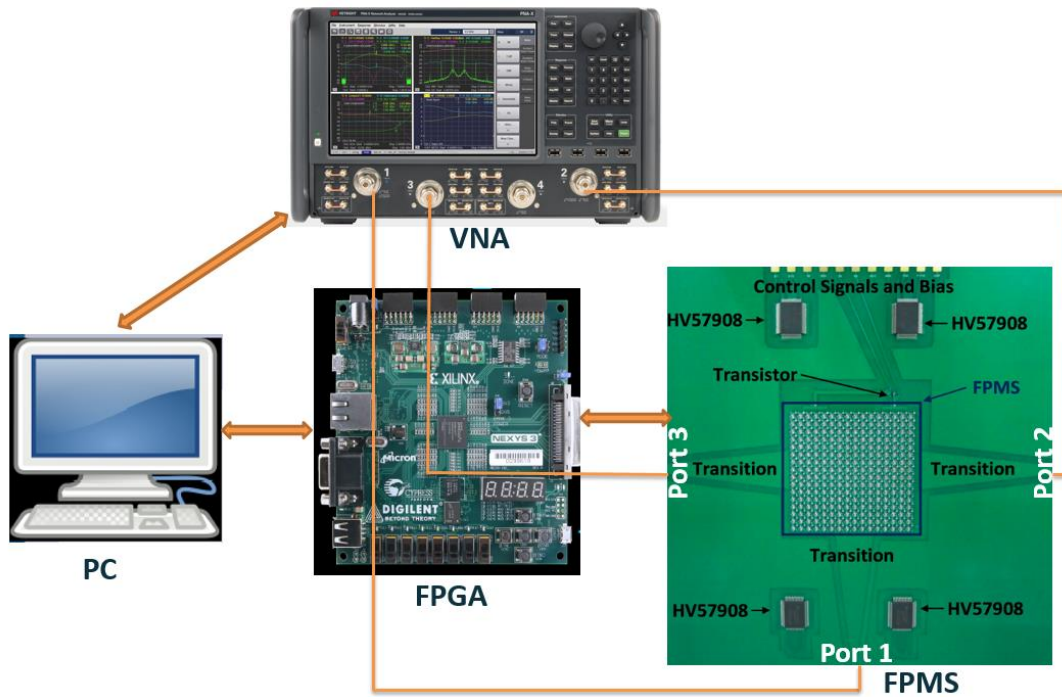


Fig. 3.1. Measurement set-up for the Live Optimization

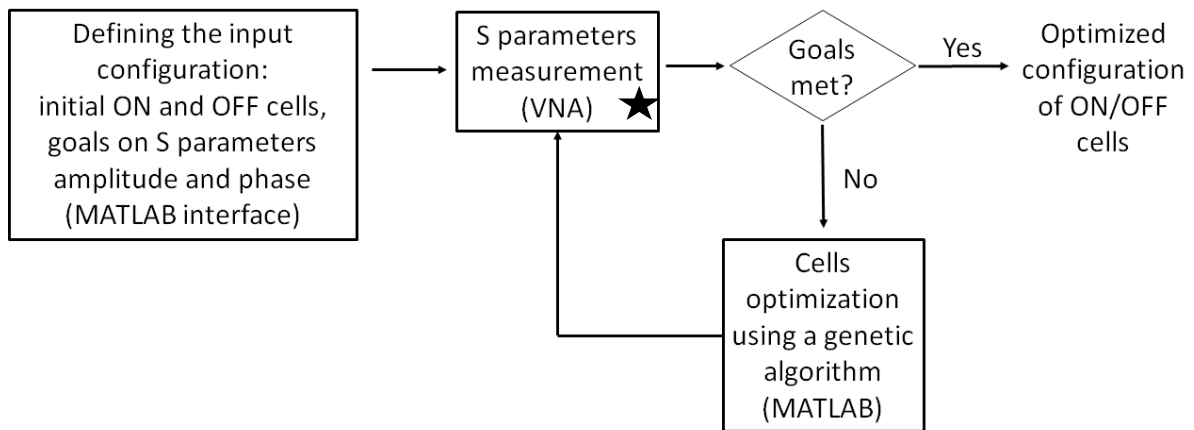


Fig. 3.2. Steps for live optimization on FPMS

★This can be replaced by S-parameters from ADS simulation tool if applied on a virtual twin.

3.2.1 MATLAB Graphical Interface

The graphical interface code developed in MATLAB that has been explained in the previous chapter makes it possible to visualize the live tuning of unit cells (either ON or OFF) and plot the corresponding S-parameters. The only difference is previously the graphical interface code was combined to ADS-MATLAB interface and here the graphical interface code is combined to the MATLAB driver for FPMS board and VNA. Also, the simulations are replaced by the actual measured results on the VNA. Since, we are using optimization directly on the actual FPMS, it will be better to use some techniques to reduce

the number of iterations to speed up the optimization time. In the next sub-section, one such strategy is described to reduce the number of variables for the optimization which will ultimately reduce the number of iterations.

3.2.2 Coarse and Fine Optimization

There are 256 unit cells in FPMS which can be turned ON or OFF, which is huge number of variables for the developed genetic algorithm and it will take very high number of iterations. Considering all the unit cells for the optimization, the number of binary combinations is then very high ($>1.e^{17}$) even if many of them do not have a physical interest from an RF point of view. In order to reduce the number of variables and the time needed for optimization, a two-step optimization approach can be used here. First, coarse optimization and then fine optimization. In coarse optimization, 4 unit cells of FPMS are grouped together as one and they are considered as a single unit cell for the genetic algorithm which basically means these 4 cells of a group will be either ON or OFF simultaneously as depicted in Figure 3.3. In this figure and the following, orange cells are ON and blue cells are OFF. In this way, number of variables are reduced to one-fourth that is 64 instead of 256 initially. Once the coarse optimization step is completed and still there is a slight chance to improve the performance of the component, then one can go for the fine optimization in which each cell can be individually turned ON or OFF.

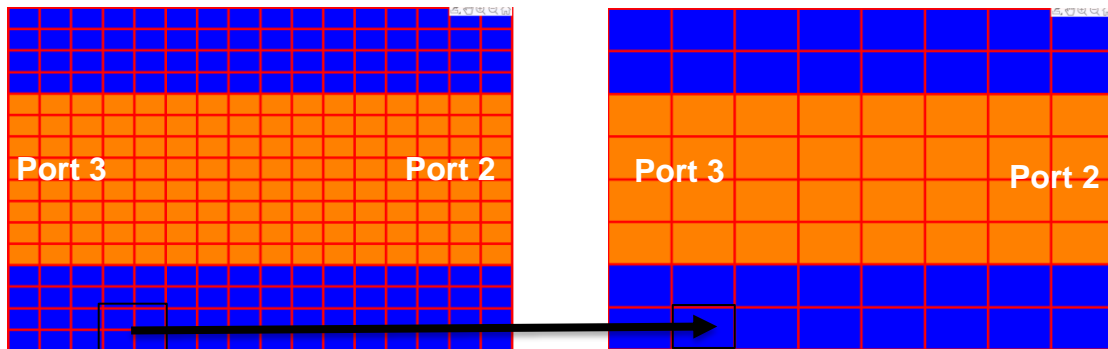


Fig. 3.3. 16x16 FPMS matrix converted into 8x8 FPMS matrix of macro 2x2 cells

The developed genetic algorithm also allows to select the cells for the optimization process based on the human knowledge of electromagnetic wave propagation as the initial configuration of the optimization process. For example, if a signal is required to travel from port 3 to port 2 (see Figure 3.3), only the cells on the middle part of the FPMS should be considered for optimization. The cells on the corner does not affect the wave propagation in this case and therefore only increases the optimization time if selected. In the graphical interface, green color border indicates that the cell is selected for optimization and red color indicates, it is not selected for the optimization process. Figure.3.4 and 3.5

depict the 16x16 matrix converted into 8x8 for the coarse optimization step. Here, two examples are used to demonstrate coarse optimization and fine optimization with the FPMS measured S-parameters.

- In a first example (Figure 3.4), few cells near to the port 2 and 3 are turned ON and unit cells in the middle of FPMS are selected for the optimization process. As it is seen, a first set of cells (a seed) has to be initially defined based on a human input at this stage. The goal here is to find out if the algorithm is able to find a path for a wave to propagate between ports 2 and 3. The S-parameters specifications for insertion loss and return loss which is achieved by the FPMS waveguide previously that is $|S_{33}|$ less than -8.5dB and $|S_{23}|$ greater than -4dB from 1.5GHz to 3GHz has been provided and then started the optimization process. As observed in Figure 3.4, the genetic algorithm is successfully able to find a path for a wave to travel between the two ports and achieved the specified goal on S-Parameters. It took 102 iterations and 8.5 minutes to complete the optimization process on a regular laptop. In this case, there is no requirement of fine optimization.

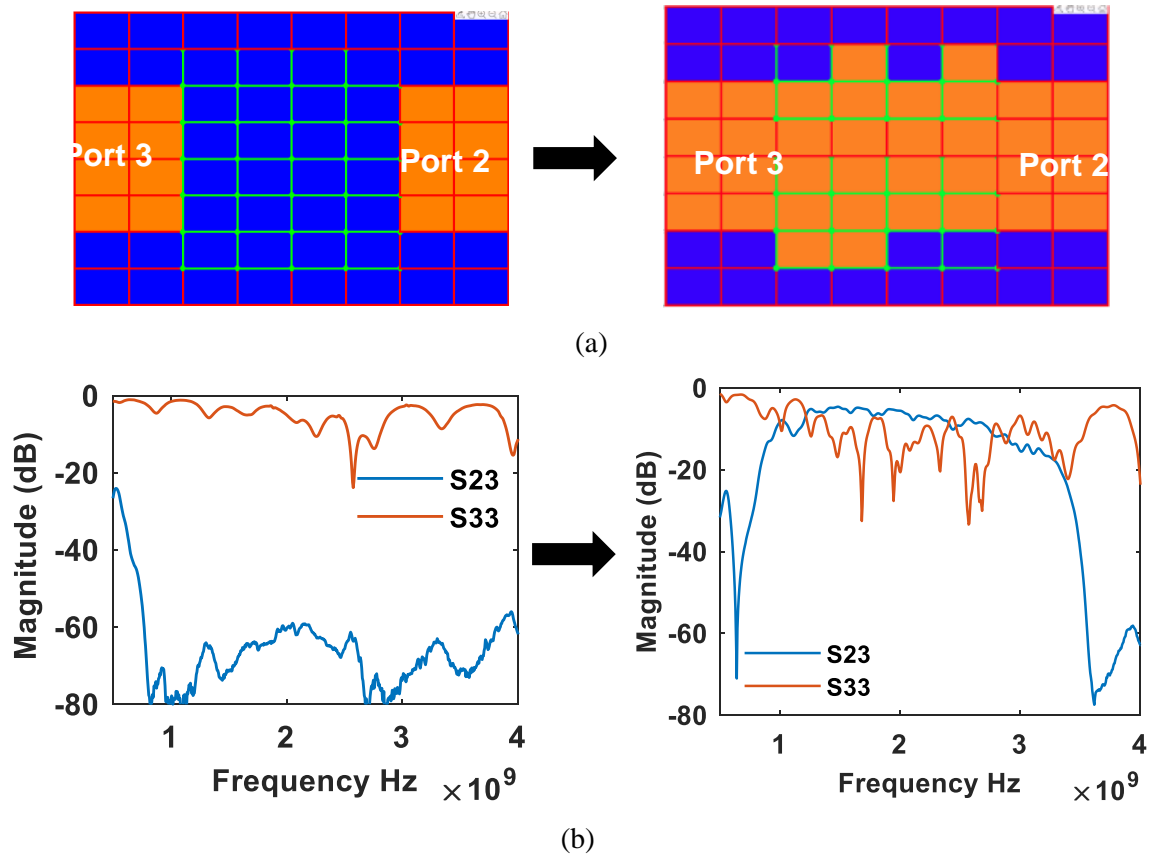


Fig. 3.4. Coarse optimization: Waveguide (a) Initial and Optimized Structure from left to right and (b) measured S-parameters of the initial (left) and optimized (right) waveguide.

- Now, in the second example (Figure 3.5) the goal is to split equal power from port 1 to port 2 and 3. Similar to previous case, few unit cells near to all the ports are turned ON and provided

the S-parameters constraints as $|S_{21}|$ should be equal to $|S_{31}|$ and both should be greater than -10dB for frequency 1.5 to 2.3 GHz. $|S_{23}|$ must remain lower than -10dB. The results obtained using coarse optimization in this case as shown in Figure 3.5 are not satisfactory, $|S_{23}|$ is below -10 dB as required but $|S_{21}|$ and $|S_{31}|$ are clearly far from being similar and both are below -10dB. Therefore, the fine optimization step is required in this case. The optimized configuration from the coarse step (converted from a 8x8 matrix back to a 16x16 matrix) now becomes the initial configuration. As observed in Figure 3.6, the fine optimization for this case provides a S-parameter response closer to the initial goal with $|S_{21}| = |S_{31}| = 8.72\text{dB} \pm 2\text{ dB}$ from 1.5 to 2.3 GHz while maintaining $|S_{23}|$ lower than -10 dB. Limited by the current FPMS performances, it was not possible to extend this configuration over a wider frequency band and to have a better result on the S-parameters.

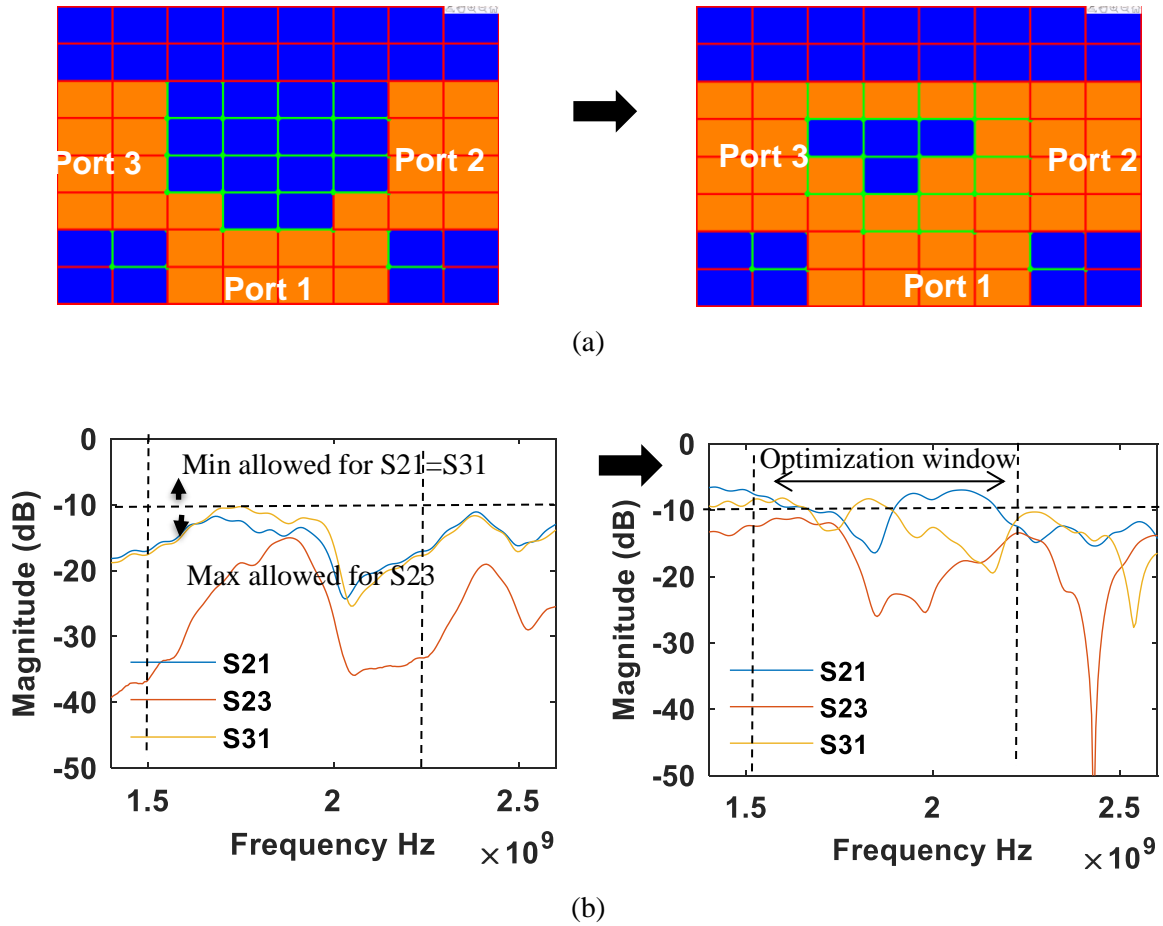


Fig. 3.5. Coarse optimization: Power divider (a) Initial and Optimized Structure from left to right and (b) measured S-parameters of the initial (left) and optimized (right) waveguide.

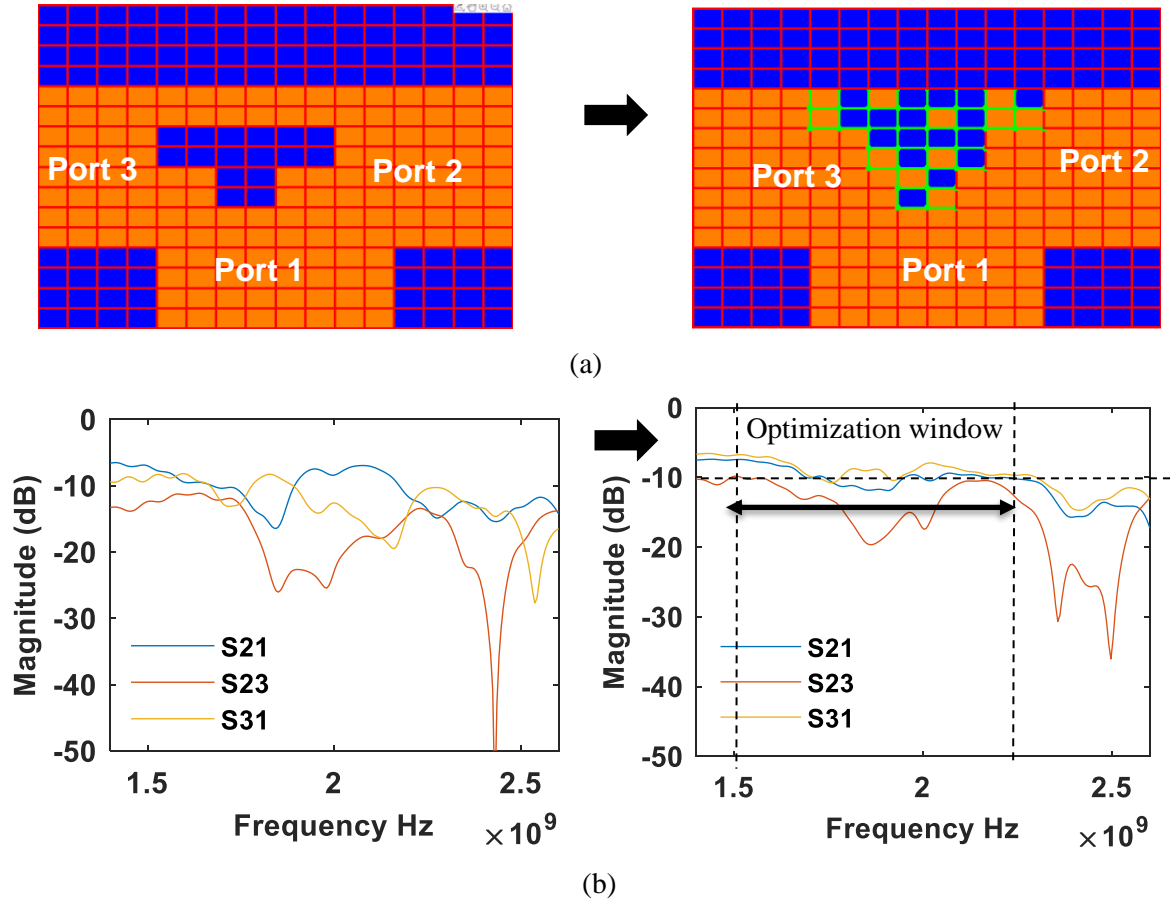


Fig. 3.6. Fine optimization: Power divider (a) Initial (in this case the optimized configuration from the coarse optimization turned back into 16x16 matrix) and Optimized Structure from left to right and (b) measured S-parameters of the optimized waveguide.

After testing this approach on these simple cases, this optimization technique has been applied in the next section to split power between the three ports of FPMS with specific goals on the amplitude and phase. A tunable notch filter will also be optimized following the same optimization scheme. More configurations will finally be tested that is mixing the function of FPMS with a specific focus on combining inherent signal routing capabilities of the FPMS with programmable phase shifting and attenuation.

3.3 Power Divider

In the previous section, it has been shown that FPMS can be used to split power between the three ports and that the coarse and fine optimization strategies provide options to reach our goals (taking obviously into account the physical limitations of the FPMS). In this section, the coarse and fine optimization method has been more specifically used to realize even, balanced, and unbalanced power distribution with FPMS. The initial configuration and its measured S-parameter response for optimizing the power divider in all of the cases described below is shown in Figure. 3.7. A basic T-junction shape power

divider is set as a first seed for the optimizer to work with. The return loss for the initial and optimized structures in all the cases is same as that of the FPMS standard waveguide i.e., around 8.5 dB.

The initial state is a symmetrical configuration of the ON and OFF cells, leading to $|S_{21}|$ and $|S_{31}|$ being very close as seen in Figure 3.7. The slight difference is due to some damage at port 2 during the initial testing of the FPMS board. The board was accidentally bent which caused visible damage on the top of the board. The visible damage has negligible effect on the circuit, however the ground plane which is not visible may be damaged and could affect the circuit. Alternatively, the lack of symmetry could be due to the non-symmetrical component filling the transitions. Since this configuration is very close to a straight waveguide between ports 2 and 3, $|S_{23}|$ is relatively constant between 1.4 and 2.6 GHz. This experimental information that a symmetrical geometry leads to a symmetrical S-parameters is an important confirmation that the cells behave symmetrically. Therefore, with the help of the optimization, even power distribution in amplitude should be accessible.

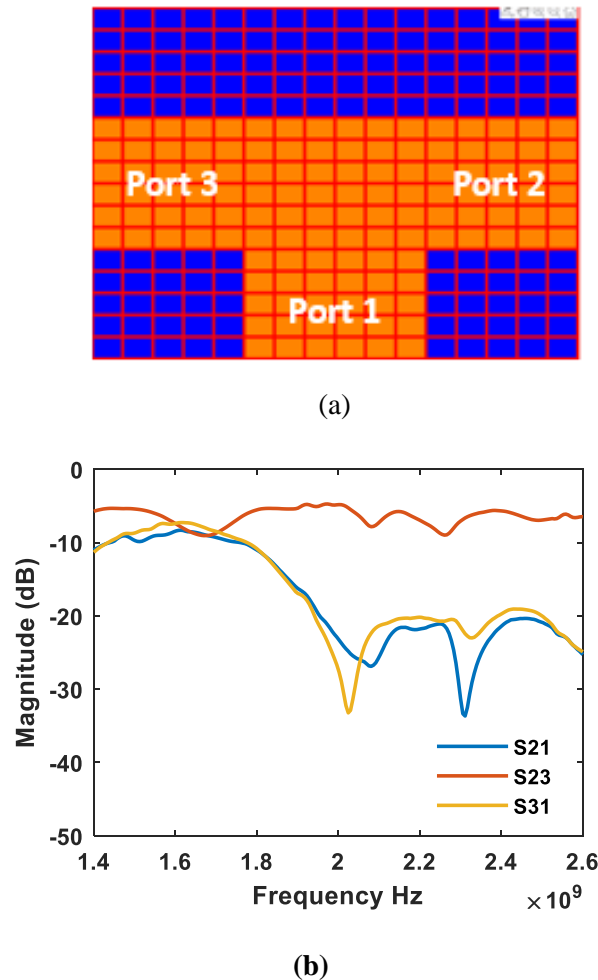


Fig. 3.7. Initial (non-optimized) configuration for the 3 ports power divider and measured S-parameter

3.3.1 Even Power Distribution

Here, the goal for the optimizer is to get equal power between any two branches of FPMS, i.e., $|S_{21}| = |S_{31}| = |S_{23}|$ and all of them should be greater than -10dB in magnitude between the frequency 1.4-1.9 GHz. The device performance did not make it possible to have such performances over a wider frequency range. Figure.3.8(a) shows the optimized configuration of unit cells of the FPMS. It took around 33 iterations and 105 seconds on a normal PC to reach the specified goal. Figure.3.8(b) represents the measured S-parameters. From 1.4 to 1.9 GHz, $|S_{21}| = |S_{31}| = |S_{23}| = 8.81\text{dB} \pm 1.1\text{ dB}$.

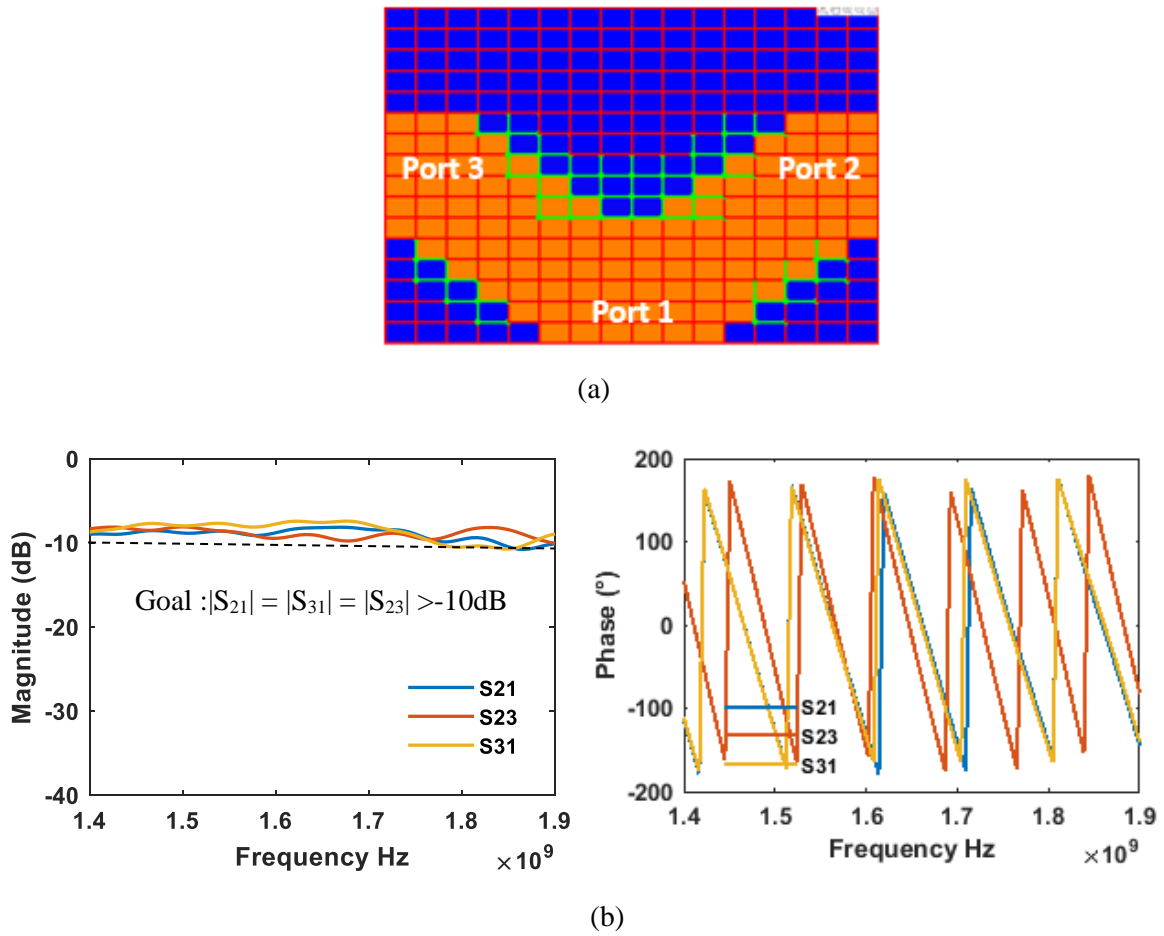


Fig. 3.8. Even power distribution (a) Optimized configuration, (b) measured S-parameters from 1.4 to 1.9 GHz.

In this case, no specific goals were defined on the phase of the S-parameters. Thanks to the symmetry of the obtained configuration, phase difference between $|S_{21}|$ and $|S_{31}|$ is approximately 0° . Since the signal path between ports 2 and 3 is longer compared to the path between ports 1 and 2 (identical to the path between ports 1 and 3), the phase difference between $|S_{23}|$ and $|S_{21}|$ is continuously changing in the entire frequency range. It should be then possible to optimize at the same time the magnitude and phase balance between the ports by applying a similar methodology.

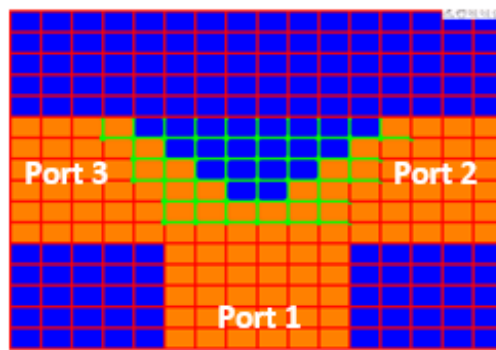
3.3.2 Balanced Power Distribution

- **Equal magnitude and phase**

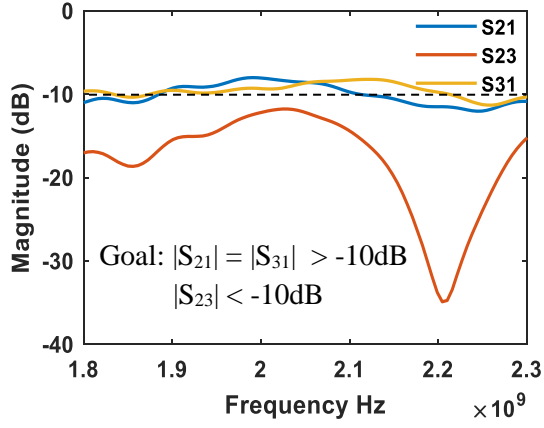
A balanced power divider with the FPMS can be realized by using its port 1 as input port to distribute equal power to output ports 2 and 3. Since the optimization algorithm allows to put the specifications on the phase of S-parameters, one can decide to have either constant phase or distinct phase between the ports 2 and 3. For the first case, the goals specified for the optimizer are both the magnitude and the phase of S_{21} should be equal to the magnitude and the phase of S_{31} . In order to achieve better isolation between the ports 2 and 3, one can put the goal on magnitude of S_{23} that it should be less than -12dB. Figure. 3.9 depicts the configuration of FPMS cells for same magnitude with constant phase and the corresponding S-parameters, considering an optimization between 1.8 and 2.3 GHz. Over this frequency range, $|S_{31}|=|S_{21}| = -9.21 \text{ dB} \pm 0.6 \text{ dB}$ and $|S_{23}|$ is less than -12 dB. The phase difference between S_{21} and S_{31} has an average value of $0.18^\circ \pm 2^\circ$ over this frequency range.

- **Equal magnitude and different phase**

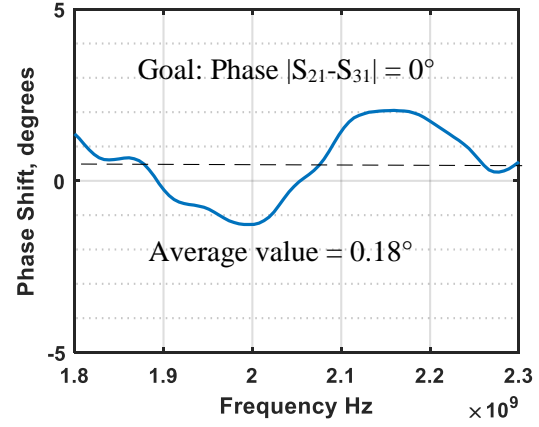
In the second case, one goal for optimizer is to have the same magnitude of S_{21} and S_{31} and then one can obtain different phase shift between the ports 2 and 3. In this case, we set a goal to achieve a phase shift of 45° between S_{21} and S_{31} . The average phase shift achieved between the two ports and between the optimization window from 1.8 GHz and 2.3 GHz is $40.62^\circ \pm 20^\circ$. Over this frequency range, $|S_{21}| = |S_{31}| = -8.78 \text{ dB} \pm 1.1 \text{ dB}$. Figure 3.10 depicts the configuration of FPMS cells for equal magnitude and different phase and its corresponding S-parameters. The isolation between port 2 and 3 ($|S_{23}|$) could not be improved further because there is no possibility of creating a variable resistor in FPMS as we have in Wilkinson power divider.



(a)

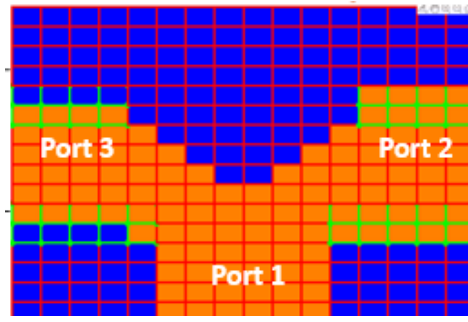


(b)

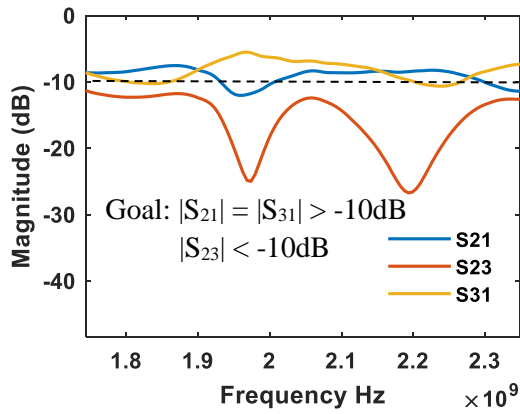


(c)

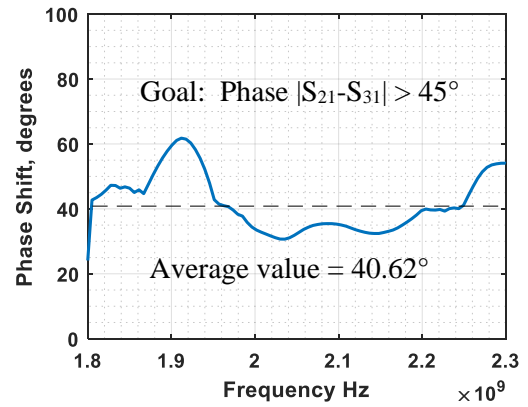
Fig. 3.9. (a) Optimized configuration for equal power distributed to ports 2 and 3 with same phase, (b) Measured S-parameters magnitude; (c) measured phase difference between S21 and S31.



(a)



(b)



(c)

Fig.3.10. (a) Optimized configuration for equal power distributed to ports 2 and 3 with different phase and (b) measured S-parameters, (c) measured phase difference between S21 and S31.

3.3.3 Unbalanced Power Distribution

Optimization algorithm also helps to realize an unequal power distribution between port 2 and port 3 through the FPMS board. The goals can be set to achieve different power dividing ratio but due to the current limitations of FPMS, it is not possible for the optimization algorithm to satisfy every imaginable

specification. Therefore, the goals set for the optimizer here are magnitude of S_{21} that should be greater than -10dB and magnitude of S_{31} that should be lesser than -10dB from 1.8GHz to 2.3 GHz. $|S_{23}|$ should still be less than -12dB over this frequency range. Figure 3.11 shows the optimized configuration and its measured S-parameters. The measured value of mean of difference between the magnitude of S_{21} and S_{31} is 6.74dB. The OFF cells that are between the ports 2 and 3 provide a diminution of the amount of energy that goes between them. They create a natural obstacle that decreases the magnitude of S_{31} and S_{23} .

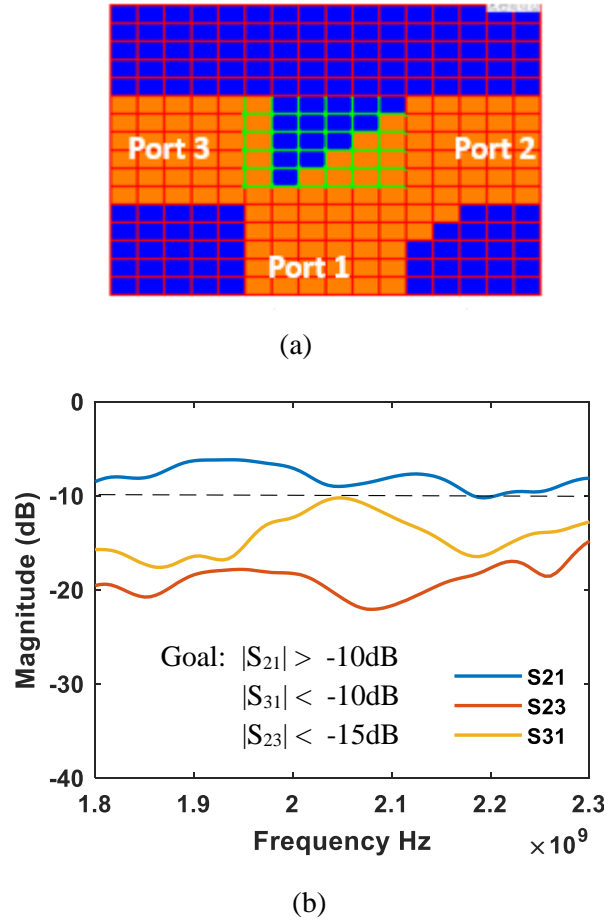


Fig. 3.11. Unequal power distribution from port 1 to ports 2 and 3 (a) Optimized configuration and (b) measured S-parameters.

The power divider realized using FPMS does not have better performance than the microwave circuits specifically designed for a power dividing function presented in [10]–[13]. But it should be noted here that FPMS is designed to perform multiple functions at the same time. In the next section we will see how FPMS can be used as a tunable notch filter.

3.4 Tunable Notch

The term "notch" refers to the shape of the frequency response of the filter, which is characterized by a deep dip or "notch" in the passband. The tunable aspect of the notch filter refers to its ability to adjust the frequency at which the notch occurs, allowing it to reject different frequencies as needed. A tunable notch can be realized from the FPMS by turning some unit cells ON either side of a waveguide, creating locally a stub whose size (width, length and position) can be changed by using the optimization algorithm explained in section 3.2.

We have first selected the unit cells for the optimization on either or both side of waveguide structure and then specify the goals for the optimizer to have a notch at desired frequencies. Two different waveguide structures have been used here to get a tunable notch behavior. First case depicts a straight 6 cells wide waveguide structure and the cells with green boundaries have been chosen for optimization to achieve the goals. Figure 3.12 shows three optimized configurations to have a notch at 1.64 GHz, 1.77 GHz and 1.83 GHz respectively with a S_{23} magnitude lower than -10dB. In the second case, a curved waveguide structure is used, and the same method as in first case is applied. Figure 3.13 shows the three optimized configurations for this case to have a notch at 1.9, 2 and 2.1 GHz respectively.

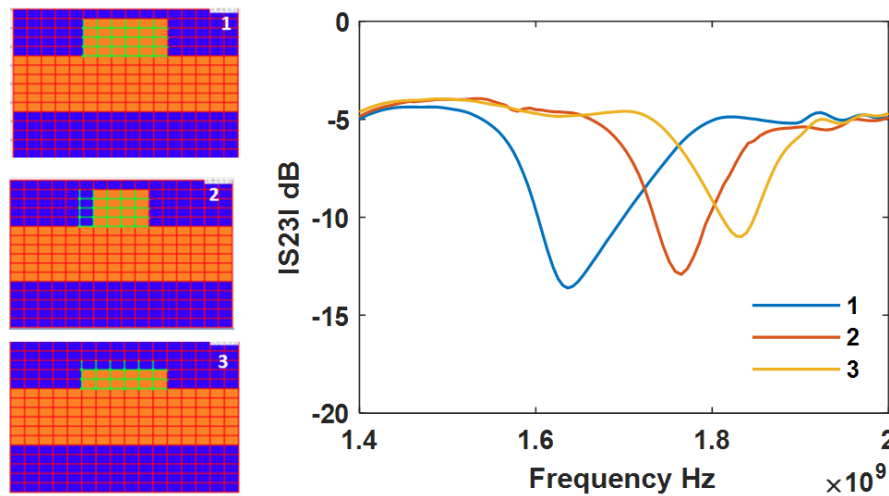


Fig. 3.12. Straight waveguide based tunable notch structure and measured S-parameters

The optimization algorithm with the FPMS reconfiguration capability can handle such problem and create on demand a band stop behaviour at a given frequency. Inducing more cells for the optimization may help to optimize the $|S_{23}|$ out of the rejected region.

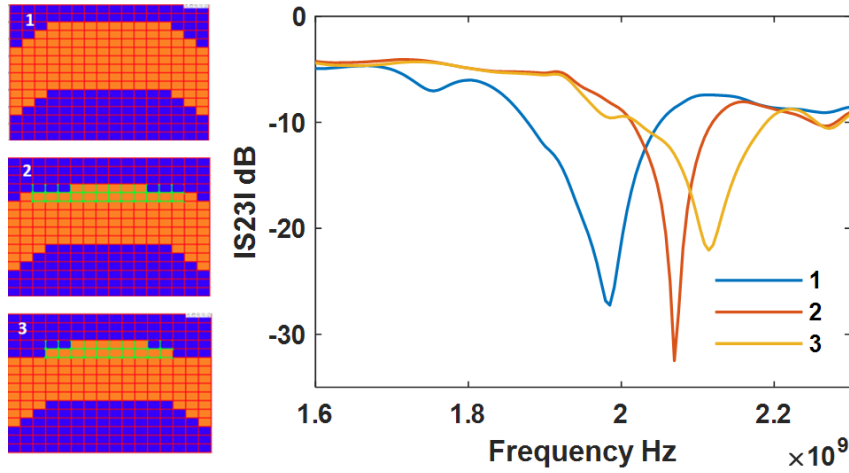


Fig. 3.13. Curved waveguide based tunable notch structure and measured S-parameters

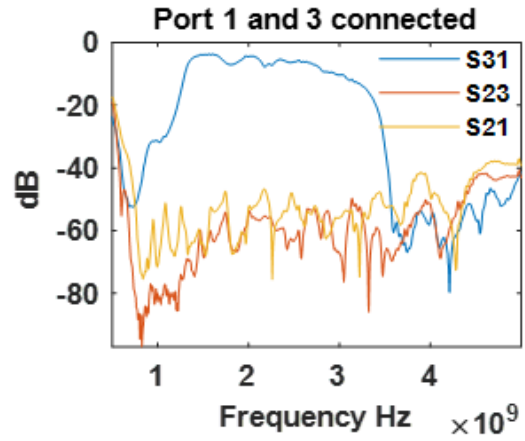
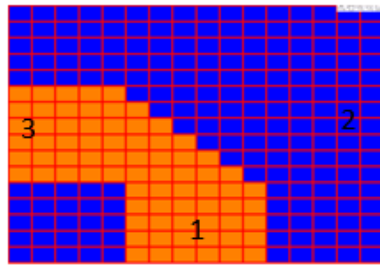
3.5 Mixing Signal Routing and other functions

This section will be focused on one key feature of the FPMS that is its capability to route signal from one port to other one and to combine functions using the FPMS. For example, we can target a specific phase range while the signal goes from one point to another one. On top of that, adding OFF cells at precise locations helps adding more losses and then creating a tunable attenuation. Based on these points, we will first see if we can create a bended waveguide (i.e., from port 1 to port 2 or 3) that is as good as a straight one between the port 2 and port 3 and measure the isolation that is achievable between the ports that are not connected. We will then add to these building blocks (straight or bended waveguide) two more features, a programmable phase shifter and a programmable attenuator.

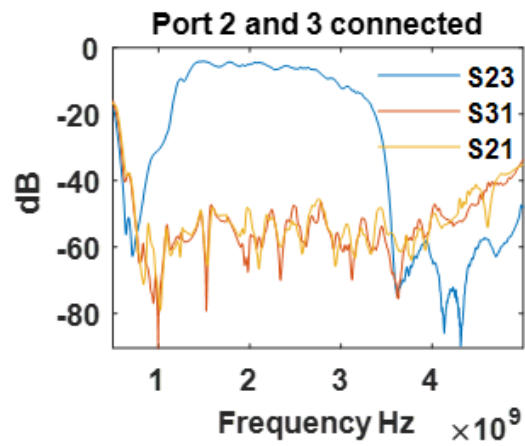
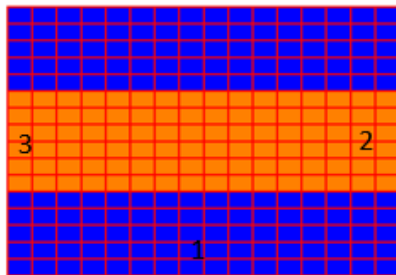
3.5.1 Switch

This section presents the FPMS potential to function as a switch without using optimization as a first step. The FPMS can be used as a switch due to its capability to route signal between its three different ports as depicted in Figure.3.14 where the orange cells are ON and blue cells are OFF. The measured insertion loss and isolation between the different ports are also shown in Figure.3.14.

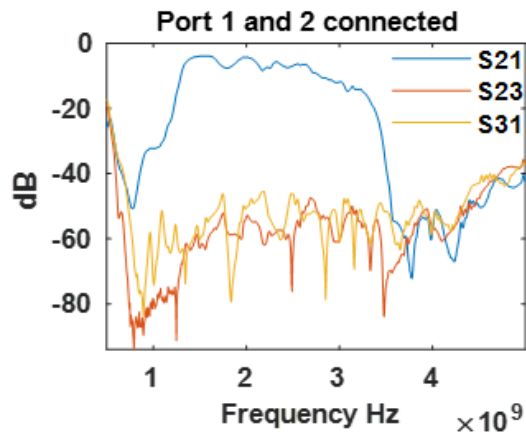
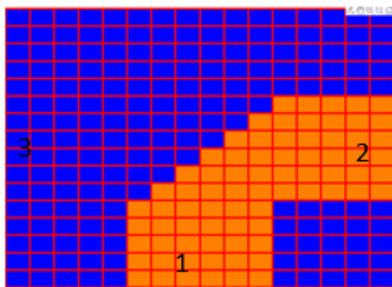
In every configuration, the direct connection between two ports (1 to 3, 1 to 2 or 2 to 3) presents the same frequency behaviour with a typical insertion loss of 5 dB between 1.5 and 3 GHz. A minimum isolation of 50dB is achieved (thanks to the OFF cells between two isolated ports) in all cases over the same frequency range. The return loss for all the configurations is almost the same, at a level of 8.74dB. The insertion loss is relatively high but the isolation is reasonably good in comparison to switches mentioned in [5] and [6]. Due to the reconfigurable nature of the FPMS, we can easily change the direction of the propagating wave from one port to another one while having 50dB of isolation between the unconnected ports. We will then apply the optimization algorithm to add to a straight or bended waveguide a programmable phase shifter.



(a)



(b)



(c)

Fig. 3.14. Switch (a) Configuration for signal routing between ports 1 & 3 and measured S-parameters; (b) Configuration for signal routing between ports 2 & 3 and measured S-parameters; (c) Configuration for signal routing between ports 1 & 2 and measured S-parameters.

3.5.2 Signal Routing and Phase Shifting

This section presents FPMS capabilities of phase shifting on the transmitted path using binary state reconfiguration. The phase shifter can be realized in two ways using FPMS. First, using the developed optimization algorithm while keeping the same biasing voltages and second, using the voltage control of the ON state of the FPMS cells. Here, the phase shift for straight and bended section of waveguides using both methods are presented.

- **Phase Shifter using optimization**

Phase shifting can also be obtained from the straight and bended waveguide configurations using the genetic optimization algorithm. In this method, the ON unit cells are biased to 25V for all the cases. To achieve the required phase shift, different constraints were added to the phase of S_{23} for the straight waveguide case and to the phase of S_{31} for the bended waveguide case at 1.5 GHz. After that, the live optimization on the FPMS board has been launched as described in section 3.2. The developed MATLAB code allows us to choose the cells that will be considered for the optimization process, the initial configuration being based on human knowledge of propagation of electromagnetic waves. This step is not mandatory since we can start with a random configuration but it reduces the computation time for the optimization algorithm. For instance, we can predict that the 25-30 unit cells around the waveguide structure can alter the phase value while maintaining the same magnitude. So, if only those cells are selected for the optimization process, the average computation time is between 9-10 minutes on a regular laptop. As we increase the number of cells for optimization process, the computation time increases. It can take up to several hours to do the optimization if all cells are selected for the optimization process. This step is useful for every device that can be implemented using FPMS. After running different test scenarios, it is finally observed that the cells on the boundary of waveguide actually contributes to phase shift as expected. Figure. 3.15(a) and 3.16(a) show the configuration of ON/OFF cells on the FPMS board that were proposed by the optimizer, which yields to different phases while keeping the insertion loss for the straight and bended waveguide approximately constant as shown in Figure. 3.17. The cells in the orange color with green border are ON and have been manually selected for the optimization in most of the cases and the cells in blue color are OFF.

In order to produce the results that can be observed in Figure.3.15 and 3.16, we gave to the optimizer a goal on the phase of S_{23} (Figure. 3.15) and S_{31} (Figure. 3.16) to have a value equal to, less than or greater than a given value in degrees. At the same time, a complementary goal was to limit as much as possible the degradation of the insertion loss and maintain a return loss equivalent to the one of a regular waveguide (see case 1 in Figure. 3.15 (a) for example).

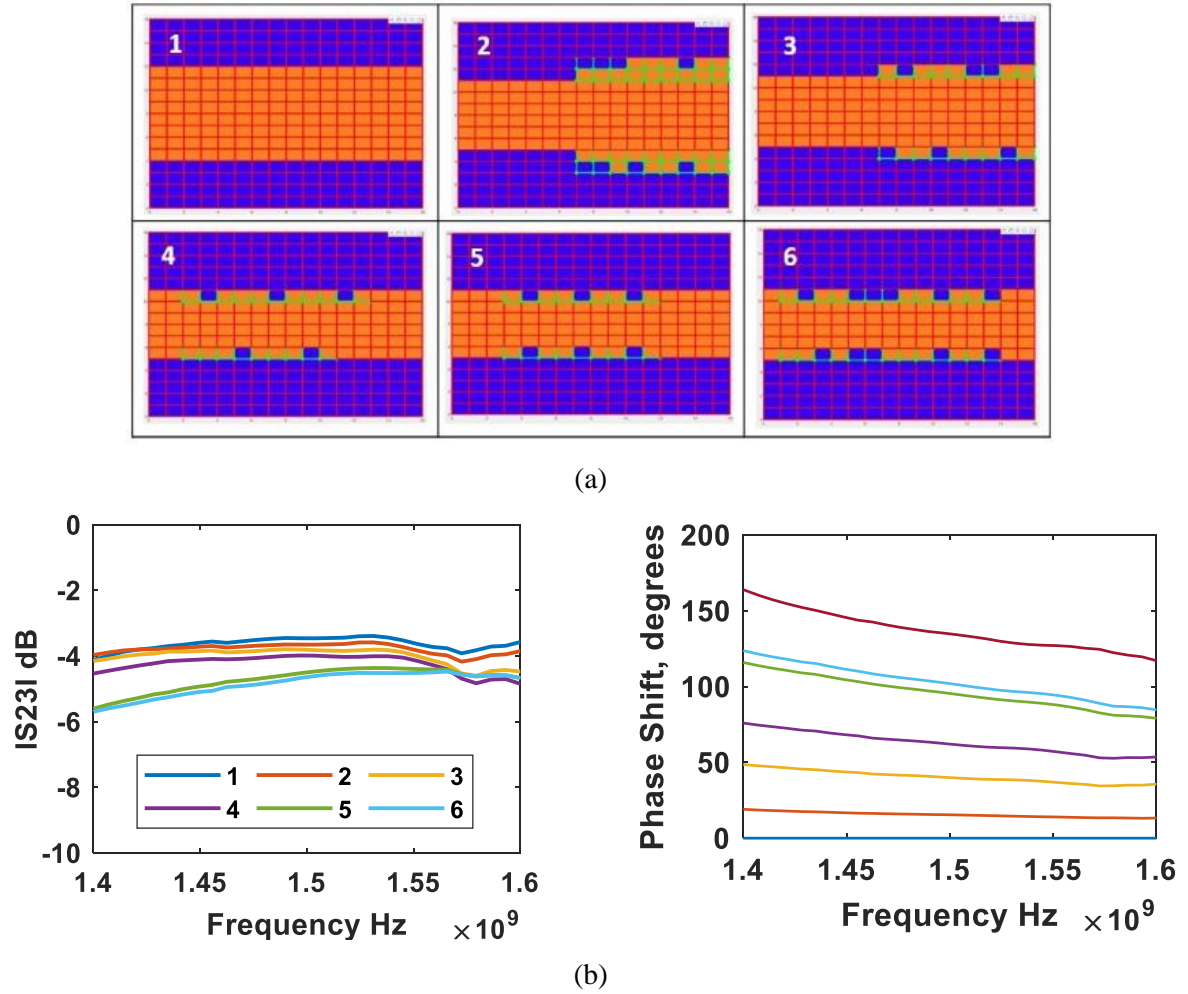
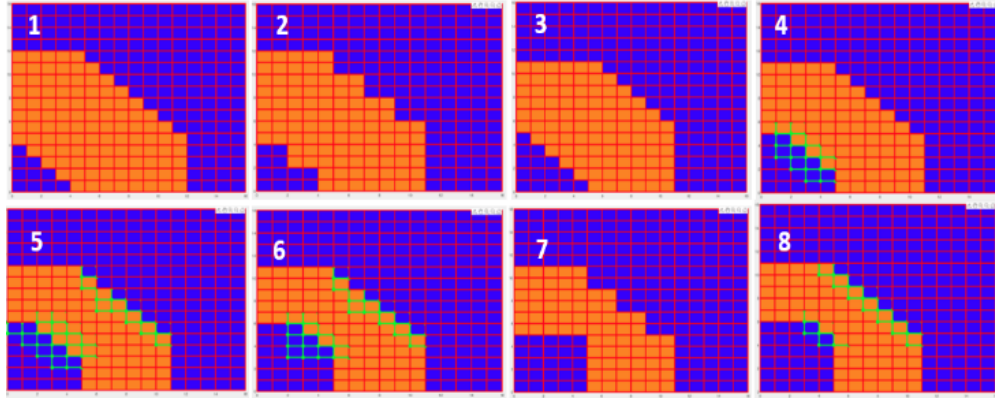


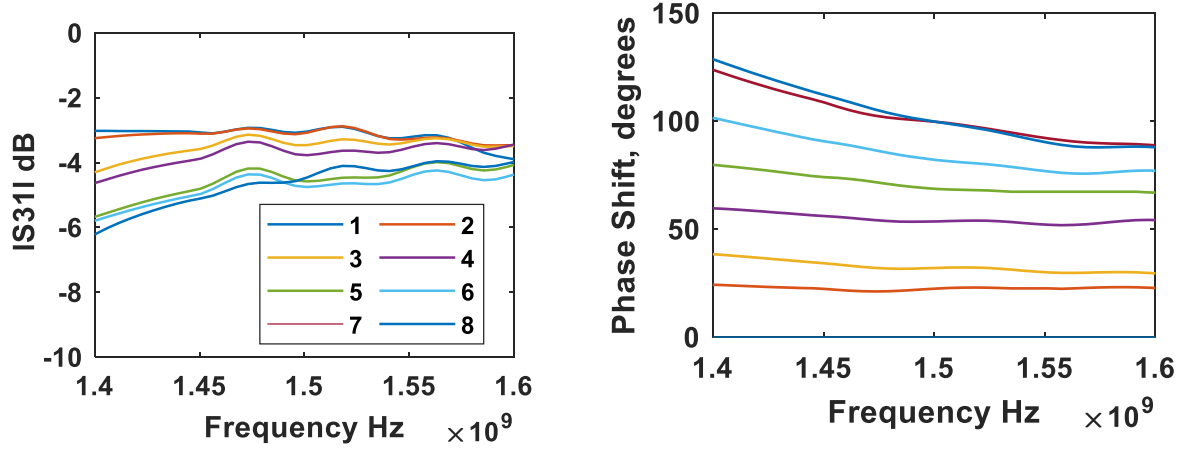
Fig. 3.15. Phase shifter obtained by optimization (a) Optimized structures for straight waveguide (port 2 to 3), (b) Measured $|S_{23}|$ in dB and phase shift in degrees for straight waveguide.

The measurement results for the phase shift and insertion loss are depicted in Figure. 3.15(b) and 3.16(b). The total phase shift obtained for the straight waveguide case is 134° at 1.5 GHz with an average insertion loss of 4.4 dB and phase shift obtained for the bended waveguide case is 100° at 1.5GHz with an average insertion loss of 5 dB. This relatively large insertion loss is a known limitation of the current FPMS board [1]. The phase shifter's figure of merit (FOM) is $30.45^\circ/\text{dB}$ and $20^\circ/\text{dB}$ at 1.5 GHz for the straight and bended waveguide respectively.

The phase shifting effect is provided by local variations of the waveguide width. By doing so and for a physical identical length L of 16 cells for a straight waveguide, a $\Delta\phi = \Delta\beta.L$ phase shift occurs with $\Delta\beta$, a variation of the propagation constant. A small variation of the waveguide lower cut-off frequency occurs because of the changes in the physical width of the waveguides as it can be seen in Figure 3.17 for straight and bended waveguide cases, the slope of $|S_{23}|$ and $|S_{31}|$ changes around 1.4GHz.

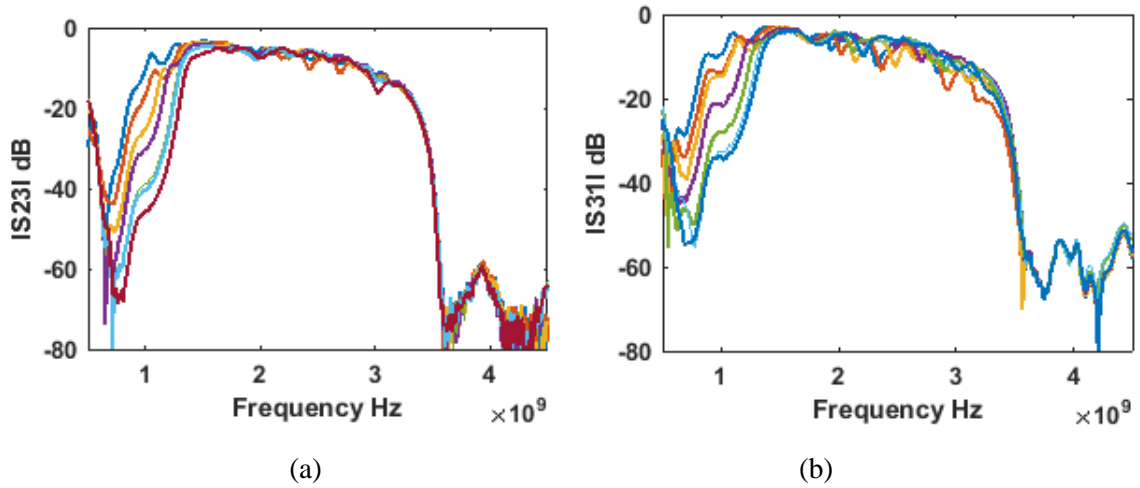


(a)



(b)

Fig. 3.16. Phase shifter obtained by optimization (a) Optimized structures for bended waveguide (port 1 to 3), (b) Measured $|S_{31}|$ in dB and phase shift in degrees for bended waveguide.



(a)

(b)

Fig. 3.17. Insertion loss for the complete frequency range (a) Phase shifter using straight waveguide case and (b) Phase shifter using bended waveguide case.

Since it is also possible to change the biasing of the ON cells, another route to add a phase shifting effect is tested in the next section.

- **Phase Shifter by varying the voltage**

All the ON cells of FPMS have the same biasing voltage but this value can vary from 8V to 25V using the microcontrollers associated with the device, so it is possible to get a phase shifter with FPMS by using different biasing voltage. Indeed, when changing the voltage from 25V to 8V, a cell remains on the ON state but its equivalent relative permittivity slightly changes from a typical value of 5 to 20 around 1.5 GHz (Figure 2.2). Then, while conserving a same physical length, its effective permittivity changes and thus its equivalent electrical length.

The upper cut off for the working frequency range of FPMS reduces as we decrease the biasing voltage value as shown in Figure 3.18 (see section 2.2 for more explanation of this behavior) for straight and bended waveguide, therefore we can only get a satisfactory phase shifter for a narrow band between 1.4 and 1.6 GHz by using this method. Any two ports can be used to achieve phase shift as shown in Figure 3.19 and 3.20. The phase shift achieved for a straight waveguide case (port 2&3) is around 180° with an average insertion loss of 4.59 dB whereas for the bended waveguide case (port 1&3), phase shift and insertion loss are 160° and 5.63 dB respectively. The phase shifter's figure of merit (FOM) is $39.22^\circ/\text{dB}$ and $28.42^\circ/\text{dB}$ for the straight and bended waveguide respectively.

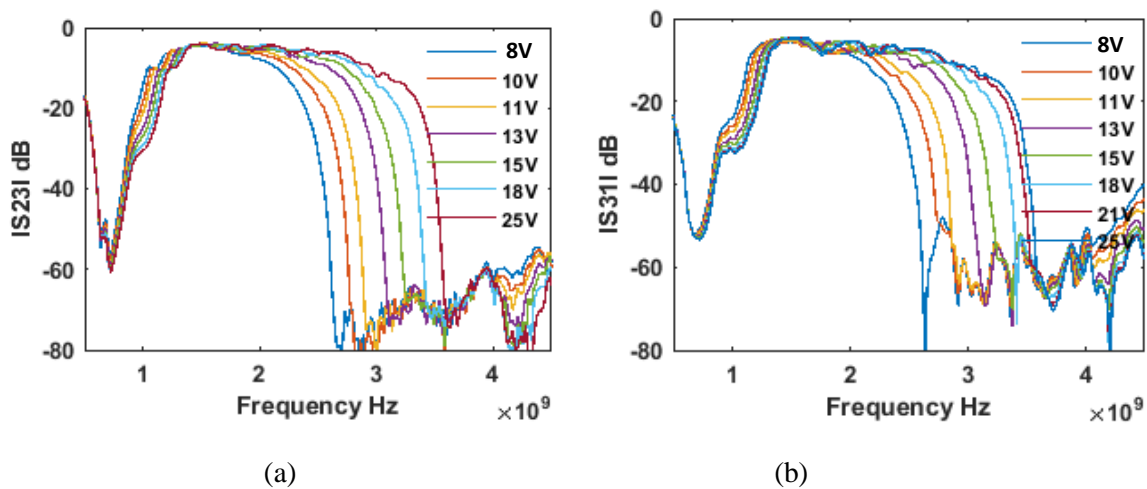


Fig. 3.18. Insertion loss for the complete frequency range (a) Phase shifter using straight waveguide case and (b) Phase shifter using bended waveguide case.

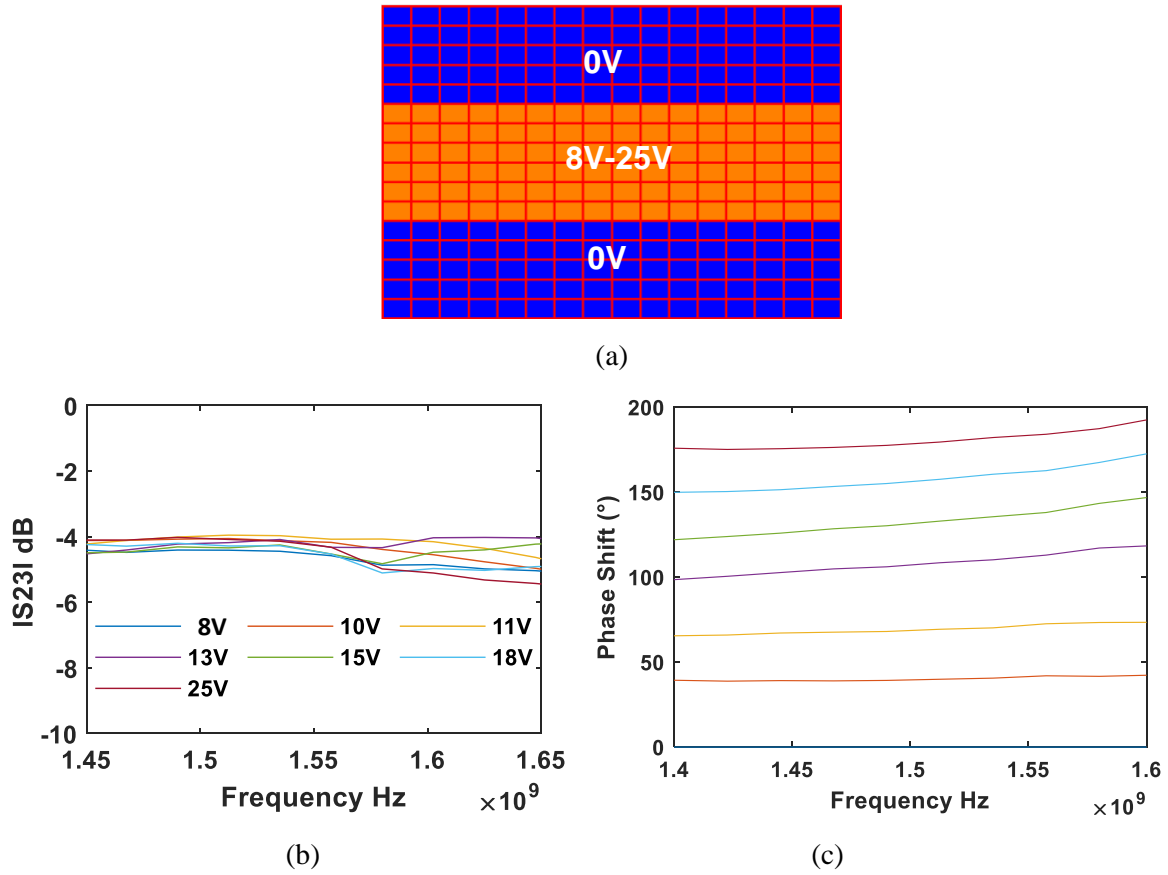


Fig. 3.19. Phase shifter obtained by changing the bias of ON cells (a) Straight waveguide structure, (b) $|S_{23}|$ in dB and (c) phase shift in degrees.

The FPMS has shown the capability to combine the function of signal routing and programmable phase shifting within a single component. Table 3.1 summarizes the key features of the phase shifter implemented using FPMS. Compared to specialized phase shifters at the same frequency [7] – [9], the FOM of FPMS based phase shifter is low. Dedicated phase shifter in [7] have a typical figure of merit $96.42^\circ/\text{dB}$ whereas the best one with the FPMS has figure of merit $39.22^\circ/\text{dB}$. On the other hand, these devices cannot offer the capability to switch from this role to any that are possible with this device. The FPMS provides the possibility to totally change its function and can provide here a signal routing and phase shifting capability as well as other functions, such as reconfigurable band pass or band stop filters [2]. In the next section we will see if signal routing and programmable attenuation can be made as well.

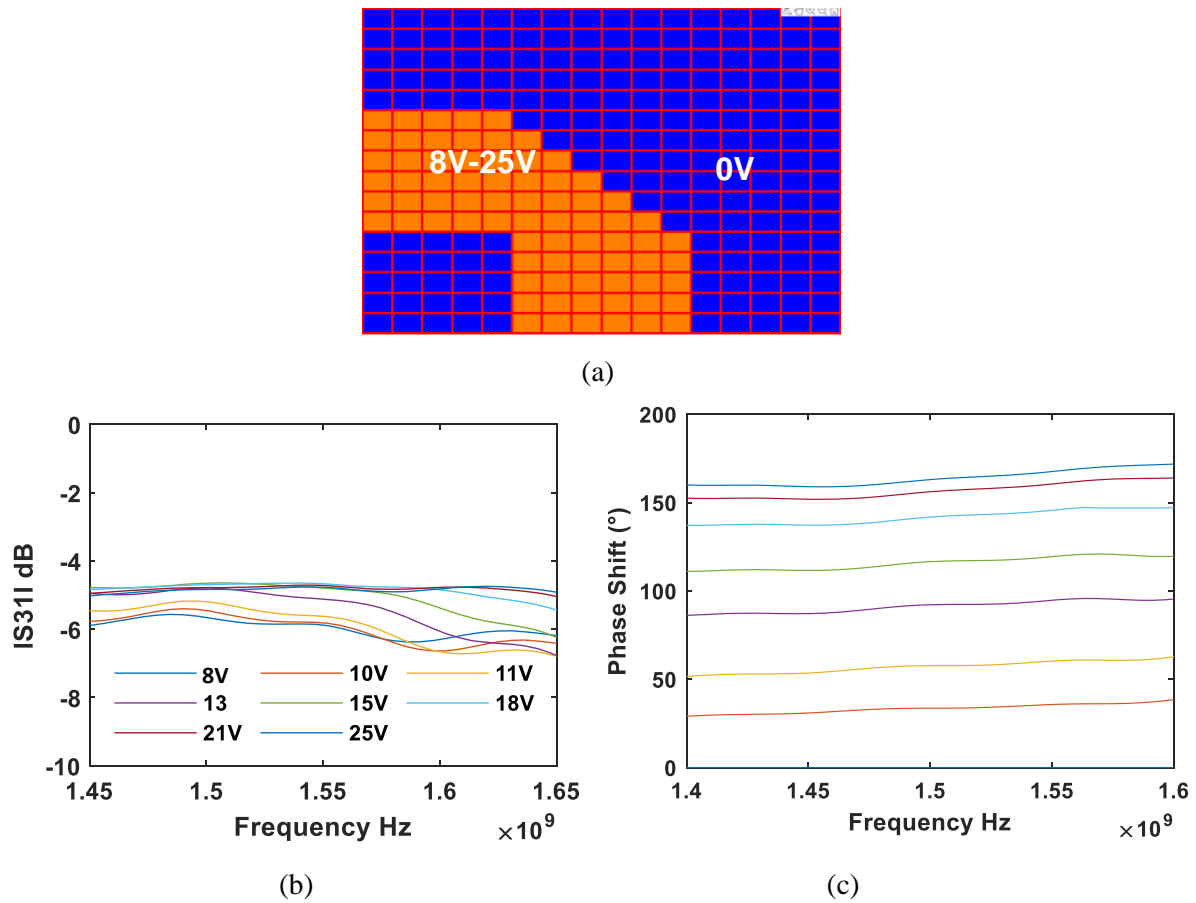


Fig. 3.20. Phase shifter obtained by changing the bias of ON cells (a) Bended waveguide structure, (b) $|S_{31}|$ in dB and (c) phase shift in degrees

TABLE 3.1. PERFORMANCE OF PHASE SHIFTERS USING FPMS

Cases	Insertion Loss (dB) (Min-Max)	Phase Shift (°)	Figure of Merit (°/dB)
Straight waveguide (8-25V)	3.99-5.2	180	39.22
Bended waveguide (8-25V)	4.65-6.62	160	28.42
Straight waveguide 25V bias using optimization	3.45-5.68	134	30.45
Bended waveguide 25V bias using optimization	3.02-6.1	100	20
[7]	0.9-1.4	135	96.42

3.5.3 Signal Routing and Programmable Attenuator

Since the isolation achieved with FPMS is very high when enough OFF cells are placed on the wave path, it can be used as attenuator as shown in Figure. 3.21 and 3.22. We can use any two ports to achieve a required isolation value. The isolation level for a straight waveguide-based attenuator varies from 10 dB to 70 dB at 2 GHz as shown in Figure. 3.21(b) by turning OFF the last columns of unit cells on the FPMS board. Similarly, the programmable attenuator can be achieved using a bended waveguide structure as shown in Figure 3.22(a). For this case, the isolation level varies from 10dB to 50dB only at 2GHz because less cells have been defined in the OFF state in that case. The average isolation is around 8.4 dB for each added column of OFF cells and as we increase the number of columns of OFF cells, isolation value increases. The return loss is almost same for all the cases i.e., 8.5dB. Figure 3.23 pictures the measured isolation for the straight and bended waveguides as the number of columns of OFF unit cells are placed in the path of wave propagation. If a high enough number of OFF cells are involved, isolation higher than 80dB can be reached.

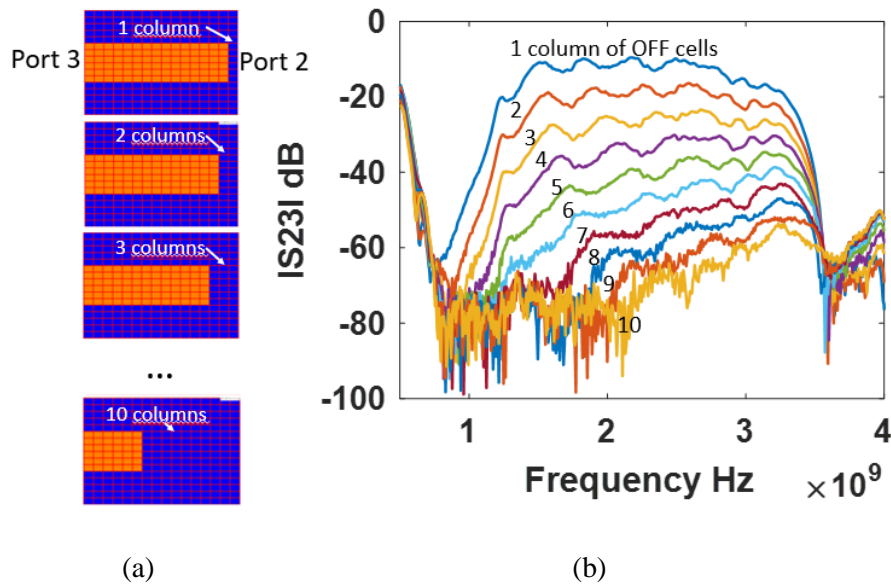


Fig. 3.21. (a) Straight waveguide based programmable attenuator when 1, 2, ... up to 10 columns of OFF cells are applied; (b) $|S_{23}|$ in dB for these different configurations.

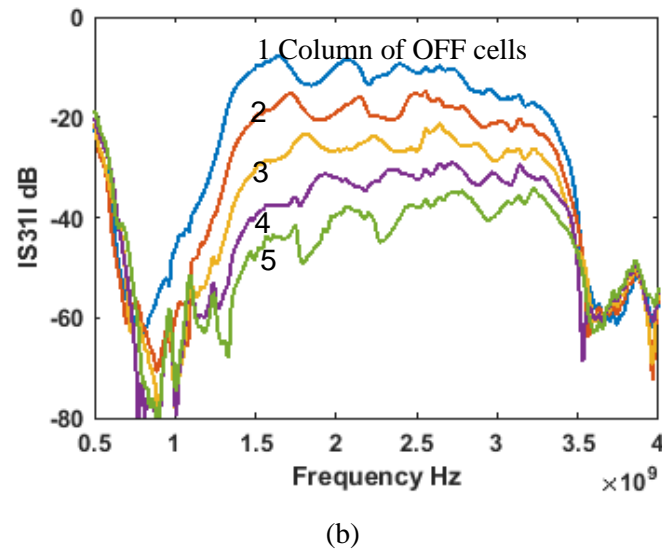
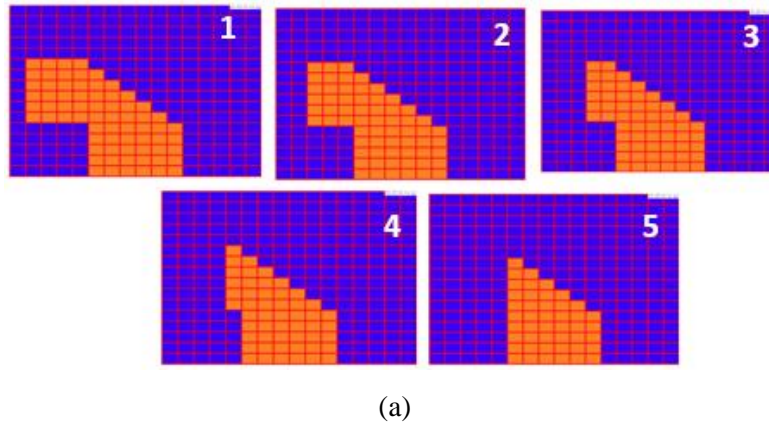


Fig. 3.22. Bended waveguide based programmable attenuator when 1, 2,... up to 5 columns of OFF cells are applied; (b) $|S_{23}|$ in dB for these different configurations.

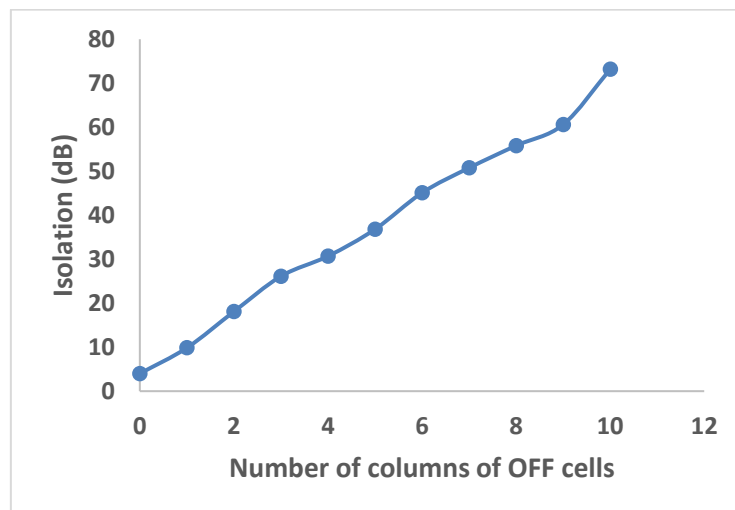


Fig 3.23. Isolation v/s number of columns of OFF unit cells

3.6 Discussions on FPMS

The capability of FPMS to realize different microwave components using a single hardware is successfully demonstrated in this chapter. From general point of view, Table 3.2 gives an overview of the reconfigurable devices that can switch from one role to another one (or to many others). To the best of our knowledge, the FPMS has demonstrated the most versatility compared to other propositions in the literature (except insertion losses) in comparison. The only comparable device is from [15] since same device can be configured to a large amount of roles. However, this is done by hard wiring the device, making it not possible to change its function on the fly. The obvious tradeoff is that such device cannot excel in every imaginable role compared to a dedicated and carefully designed component, but has demonstrated a possibility to combine roles (for example power division and phase shifting), especially when combined with a live optimization algorithm.

The performance of microwave components implemented using the FPMS still needs to be improved. One of the major drawback of FPMS is its high impedance mismatch which is caused by the existing transition between the SMA connectors and the FPMS bringing a low return loss around 8dB. It can be significantly reduced by re-modelling the transitions and it will be implemented in the 2nd generation of FPMS shown in the next chapter. Another drawback is the losses in the FPMS which are caused by several factors. The cells with negative permittivity that are used to confine the wave inside the FPMS cause significant amount of losses because of their loss tangent. Their negative permittivity value required to properly confine the wave should remain high but it decreases with increase in frequency (see Figure 2.6). Another major cause for higher loss is that the current FPMS is made up of FR4 substrates which have a very high dielectric loss tangent (0.02). This loss can be reduced by using a better PCB with a lower dielectric loss tangent.

Secondly, another key limitation is brought by the biasing states (ON/OFF) and the fact that the biasing of all the ON cells changes at the same time. A new generation of FPMS with a individual control of each cell biasing would greatly multiply the reconfigurability of this device. Finally having more ports and more cells create more room to combine the functions, i.e., having a power division + a filter + a phase shifter into a single board for example. But this would be at the price of a greater complexity in the wiring of the device.

All these limitations have been taken into account and have been improved in the upcoming next generation of FPMS. The next generation will also work on the higher frequency range. Right now, the upper limit of the operating frequency is determined by the self-resonant frequency of the unit cell. To raise this frequency, the best approach is to make the unit cell smaller. The optimization code developed for the current generation of FPMS is also compatible with the next generation of FPMS and any kind of similar devices.

The next chapter will deal with these potential improvements as well as testing the proposed algorithms with another highly reconfigurable passive component.

Table 3.2: Reconfigurable Multi-functional Microwave Components

Reference	[14]	[15]	[16]	[17]	[18]	FPMS (This work, [1], [2], [19], [20], [21])
Reconfigurable Method	p-i-n diode	Bonding wire	PCM	S/w & p-i-n diodes	Tuning resistance	Varactor diodes
Frequency range (GHz)	2-3	2-4	2-10	2.5-3.5	0.78-1.11	0.9-3
Insertion loss (dB)	2.8 to 3.4	3.7 to 4.7		1.6-2.7	3-7	3.99-6.62
General Comment		Not on the fly reconfigurability	No experimental demonstration	External control by FPGA		
Functions	Antenna	✓		✓		✓
	Bandpass filter	✓	✓		✓	✓
	Bandstop filter		✓			✓
	Coupler		✓		✓	
	Power Divider		✓		✓	✓
	Attenuator				✓	✓
	Phase Shifter					✓
	Signal Routing					✓

3.7 Conclusion

In this chapter, different reconfigurable microwave components are presented using the concept of field programmable microwave substrate (FPMS) in combination with a live optimization method based on actual measurement of the device S-parameters. The designs include power divider with tunable power dividing ratio, tunable notch, a phase shifter, switch and programmable attenuator. The optimization technique developed enables the S-parameter response of the device to be altered live according to the desired specifications, making it easier and faster to realize different microwave functions while achieving the best performance possible with the FPMS. By utilizing the real measured S-parameters instead of simulated ones from an equivalent model, the optimization method obtains highly precise results from the FPMS cell behavior and eliminates any disparities between the simulated and measured response of the components.

The chapter also outlines optimization approaches that aim to decrease the number of variables that require optimization. These strategies employ coarse and fine techniques to waveguides and three-port power divider.

The live optimization technique combined with the concept of FPMS, has successfully demonstrated the mentioned tunable RF functions, through a single FPMS board. The chapter was thus focused on power dividers with three ports that allow for dynamic reconfiguration, so that power from one port can be split between two ports with a specific amplitude ratio and desired phase difference. In the frequency range of 1.5 to 3 GHz, the switch exhibits a standard insertion loss of 5 dB. and ensures a minimum isolation of 50 dB between the isolated ports. For the phase shifter, various biasing voltages can result in a maximum phase shift of 180° . For a programmable attenuator, the level of isolation can range from 10dB to 70dB. The FPMS concept, along with the optimization technique, facilitates the rapid and effortless realization of various microwave functions by activating or deactivating unit cells on the FPMS board. Consequently, the potential for FPMS technology to attain a programmable microwave circuit design similar to that of FPGA in digital circuits is apparent.

The limitations of the current FPMS generation can be addressed in the next generation that will be discussed in the next chapter leading to improved performance of these components.

3.8 References

- [1] N. Jess, B. A. Syrett, and L. Roy, "The field-programmable microwave substrate," *IEEE Transactions on Microwave Theory and techniques*, vol 64, no. 11, pp. 3469–3482, Nov. 2016.
- [2] Hanyue Xu, Ying Wang, Farhan A. Ghaffar, and Langis Roy, "Reconfigurable Microwave Filters Implemented Using Field Programmable Microwave Substrate", *IEEE Transactions on Microwave Theory and techniques*, vol. 69, no. 2, pp 1344-1354, Feb 2021.
- [3] M.W.Gutowski, "Biology, physics, small worlds and genetic algorithms", *Leading Edge Computer Sciences Research*, pp. 165-218, 2005.
- [4] Ali Dia, Christophe Durousseau, Cyrille Menudier, Ludovic Carpentier, Olivier Ruatta and Stephene Bila, "Shape Optimization Methods for the Design of Microwave Circuits and Antennas", *2nd URSI AT-RASC, Gran Canaria, 28 May – 1 June 2018*
- [5] J. A. Ruiz-Cruz, M. M. Fahmi, and R. R. Mansour, "Compact four J. A. Ruiz-Cruz, M. M. Fahmi, and R. R. Mansour, "Compact four port rectangular waveguide switches based on simple short circuit loads," in *IEEE MTT-S Int. Microw. Symp. Dig.*, Jun. 2011, pp. 1-4.
- [6] K. Y. Chan, R. Ramer, R. R. Mansour, and R. Sorrentino, "Design of waveguide switches using switchable planar bandstop filters," *IEEE Microw. Wireless Compon. Lett.*, vol. 26, no. 10, pp. 798–800, Oct. 2016.
- [7] Po-Sheng Huang, Shuan-An Wei, Shan-Fon Hong, Tzu-Chiao Lin, Pai-Yu Chen and Hsin-Chia Lu, "Phase Shifters Based on Surface Mount Phase Leading Bandpass Unit Cells Using Low Temperature Cofired Ceramic(LTCC)," *42nd European Microwave Conference 29 Oct -1 Nov 2012, Amsterdam, The Netherlands*.
- [8] C.-S. Lin, S.-F. Chang, C.-C. Chang, and Y.-H. Shu, "Design of a reflection-type phase shifter with wide relative phase shift and constant insertion loss," *IEEE Trans. Microw. Theory Techn.*, vol. 55, no. 9, pp. 1862–1868, Sep. 2007
- [9] C.-S. Lin, S.-F. Chang, and W.-C. Hsiao, "A full-360 reflection-type phase shifter with constant insertion loss," *IEEE Microw Wireless Comp. Lett.*, vol. 18, no. 2, pp. 106–108, Feb. 2008.

- [10] Xiu Tiao Ye, Wen Tao Li, Can Cui, and Xiao Wei Shi, “A Continuously tunable unequal power divider with wide tuning range of dividing ratio”, *IEEE Microw. Wireless Compon. Lett.*, vol. 28, no. 7, pp. 567–569, July, 2018.
- [11] K.-K. M. Cheng and P.-W. Li, “A novel power-divider design with unequal power-dividing ratio and simple layout,” *IEEE Trans. Microw. Theory Techn.*, vol. 57, no. 6, pp. 1589–1594, Jun. 2009.
- [12] H.-S. Tae, K.-S. Oh, H.-L. Lee, W.-I. Son, and J.-W. Yu, “Reconfigurable 1x4 power divider with switched impedance matching circuits,” *IEEE Microw Wireless Compon Lett*, vol.22, no.2, pp.64-66, Feb.2012.
- [13] H. Fan, X. Liang, J. Geng, R. Jin, and X. Zhou, “Reconfigurable unequal power divider with a high dividing ratio,” *IEEE Microw. Wireless Compon Lett*, vol.25, no.8, pp.514-516, Aug.2015.
- [14] Alejandro L. Borja, Yasin Kabiri, Angel Beleaguers and James R. Kelly, “Programmable Multifunctional RF/Microwave Circuit for Antenna and Filter Operation,” *IEEE Transactions on Antenna and Wave Propagation*, vol 66, no.8 pp.3865-3876, Aug 2018
- [15] David A. Connelly, and Jonathan D. Chisum, “Dynamically Reconfigurable Microwave Circuits Leveraging Abrupt Phase Change Material”, *IEEE Transactions on Microwave Theory and techniques*, vol. 68,no. 10, pp 4188-4205, Oct 2020.
- [16] Yo-Shen Lin, Pei-Shan Lu, and Yu-Cheng Wu,, “A Novel Configurable Microwave Passive Component Based on Programmable Bridged-T Coil Array”, *IEEE Transactions on Microwave Theory and techniques*, vol.69, no. 6,pp. 3001-3014, Jun. 2021
- [17] Lei Sang, Ziyang Liu, Shuaitao Li, Wen Huang, Ping Li and Hao Tu “A Programmable Microwave Components Reconfigurable Between Four Functions” *IEEE Transactions on components, packaging and manufacturing technology*, vol. 13, no. 1, january 2023
- [18] Jonathan M. Knowles, Hjalti H. Sigmarsson, and Jay W. McDaniel, “Design of a Symmetric Lumped-Element Bandpass Filtering Attenuator (Filtenuator)”, 2022 IEEE 22nd Annual Wireless and Microwave Technology Conference (WAMICON).

[19] Aarefa Saifee, Christophe Duroiseau, Aurelien Perigaud, Nicolas Delhote, Fahad Farooqui, Ying Wang and Langis Roy “Reconfigurable Microwave Components Implemented using Field Programmable Microwave Substrate”, IEEE MTT-S International Conference on Electromagnetic and Multiphysics Modeling and Optimization 2022.

[20] Aarefa Saifee, Christophe Duroiseau, Aurelien Perigaud, Nicolas Delhote, Fahad Farooqui, Ying Wang and Langis Roy “Reconfigurable Microwave Components Based On Optimization of Field Programmable Microwave Substrate”, IEEE- MTT-S International Microwave Symposium (IMS), 2023. (Accepted)

[21] David René-Loxq , Olivier Lafond , Mohamed Himdi , Langis Roy, and Farhan Ghaffar, “Reconfigurable Half-Mode SIW Antenna Using Uniaxial Field Programmable Microwave Substrate Structure” IEEE Transactions on antennas and propagation, vol. 70, no. 11, November 2022

Chapter 4.

Field Programmable Microwave Substrate 2.0

4.1 Introduction

This chapter presents the next generation of Field Programmable Microwave Substrate i.e. FPMS 2.0 which is designed to work for higher frequency range. Increasing the frequency leads to smaller circuit implementation. This is an important advantage since the size of the components are limiting factor in the many wireless systems. It has been also developed to overcome the limitations of the first generation of FPMS. For example:

- FPMS 2.0 allows us individual control of each unit cell biasing,
- it has better SMA connectors to PCB transitions which reduce the losses and provide a better return loss.
- it is made up of Rogers 5880 substrate which has relatively very low dielectric loss tangent ($\tan\delta = 0.001$) compared to the previously used FR4 ($\tan\delta = 0.02$).
- 10.5-14.5GHz band operation
- Furthermore, it has four ports instead of three previously that can be used to combine different functions into a single board.

In the next sections, we will discuss the design of the unit cell for the FPMS 2.0 and the characteristics of the varactor diode used in the unit cell. Then, the different functions that are possible such as phase shifter, power divider and band stop filter will be simulated using the FPMS 2.0 equivalent model without using optimization algorithms as a first step.

4.2 Unit cell of FPMS 2.0

This section presents the design of a new unit cell of FPMS 2.0 developed for higher frequency band in close collaboration with the IETR (University of Rennes). The simulation of new unit cells (UCs) in 11-14GHz band has been carried out using CST Microwave Studio. These new cells have been implemented on multilayers PCB technology and are made from Rogers 5880 dielectric substrates which provide the possibility of increasing the frequency and limiting losses compared to the the previous FPMS. This substrate is characterized by a low dielectric constant ($\epsilon_r = 2.2$) and low loss tangent ($\tan\delta = 0.001$).

Fig. 4.1 shows the new UC design for the higher frequency band. The unit cell contains a varactor switch, a DC block resistor and RF block self-inductance. In order to obtain a reconfigurable board, we need to have the ability to control each unit cell independently (we want at least to have an on/off configuration but a total control of each unit cell could be optimal). To fulfill this objective, the unit cells must be isolated from a DC point of view. Thus, a multilayer technological assembly is developed that consists of 4 metallic layers and 3 dielectric ones. A via hole crosses all the multilayer structure to bias the varactor diode placed on the bottom of the structure. Some annular slots engraved in the first and third metallic layers and the reduced size of the second layer allow to isolate the cells relatively to each other in order to be able to control each UC independently for the FPMS global concept. The microwave signal is sent between the first and third layer, like a parallel plate waveguide, and the second layer connected to the first layer via the diode provides the control of the dielectric constant. The size of each cell is 2.5mm square in this case. It is corresponding to $0.125\lambda_g$ at 10GHz with a dielectric constant of 2.2.

The unit cells are designed on Rogers RT/Duroid 5880 substrate to minimize the loss as one of the main objectives of this generation. The thickness of the substrate is chosen as 0.005" (0.127 mm). Numerous simulations and optimization have been carried out by the colleagues of IETR over the cells to achieve negative dielectric constant to create an OFF state as with the first generation.

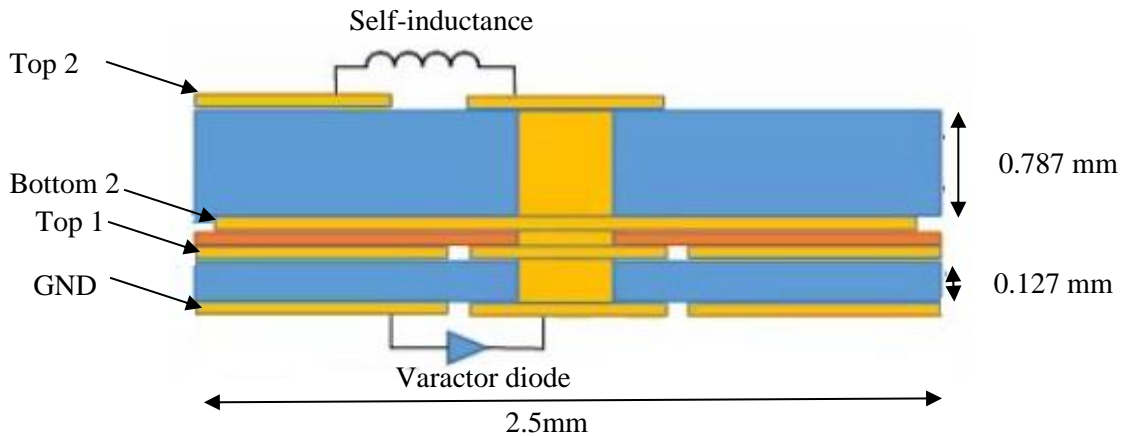


Fig. 4.1. New Unit Cell design (cross section).

The new varactor diode (MA46580-1209 MACOM Varactor) is implemented in the designs to improve the working frequency up to 10GHz. It has series resistance of 0.88Ω and low parasitic capacitance as compared to the previously used varactor (1.8Ω) which improves the losses. The characteristics of varactor diode is shown in Fig. 4.2. When the varactor diode is biased with different voltages, it provides range of capacitance from 0.14pF to 1.1pF. The extracted dielectric and magnetic constant of unit cell for different capacitance values as a function of frequency is shown in Fig. 4.3(a). When the varactor diode is biased with highest voltage, it provides lowest capacitance value (0.14pF) for ON state and

when it is biased to lowest voltage, it provides highest capacitance value (1.1pF) for OFF state. The maximum capacitance value possible for ON state for this new unit cell is 0.4pF at 4V. Above this voltage, the dielectric constant starts to be negative in the 10.5 to 14.5 GHz range that will be the operating window for our different tests. When the voltage is minimum ($C=1.1\text{pF}$), the dielectric constant is most negative, -9.03 at 11 GHz as seen in Fig. 4.3(b). At this frequency, if the ON cells use a capacitance value between 0.14 and 0.4pF, the possible positive dielectric constant can be tuned between 2.5 and 3.6. If C is still increased, higher positive values can be reached but a resonant effect will quickly limit the useable bandwidth.

According to the extracted dielectric constant for different capacitance values, the behavior of unit cells is different for the following three bands:

- Between 10.5GHz – 14.5GHz: The dielectric constant of unit cell is negative for $C=1.1\text{pF}$ (OFF state) and positive for $C=0.14\text{pF}$ (ON state). So this band will provide a proper waveguide effect if positive unit cells are sandwiched between negative unit cells (see Fig 4.4(a)) and it will be used for every other figure of this chapter. The isolation from port 1 (or port 3) towards ports 2 (or port 4) is maximum as seen in Fig. 4.4 (b).
- Between 14.5GHz – 23GHz: The dielectric constant of unit cell for $C=1.1\text{pF}$ is positive but it is smaller as compared to the dielectric constant of unit cell for $C=0.14\text{pF}$. This band will also provide a waveguide effect but the isolation between different ports will not be as good as the previous case as shown in Fig 4.4(b).
- Between 23GHz – 25GHz: The dielectric constant of unit cell for $C=1.1\text{pF}$ is positive and negative for $C=0.14\text{pF}$. In this band energy will be reflected to port 1 and a high return loss (S_{11} and S_{22}) will occur as seen in Fig. 4.4(b).

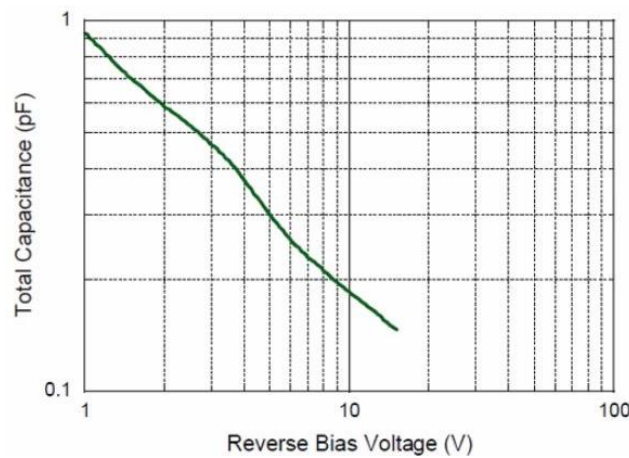
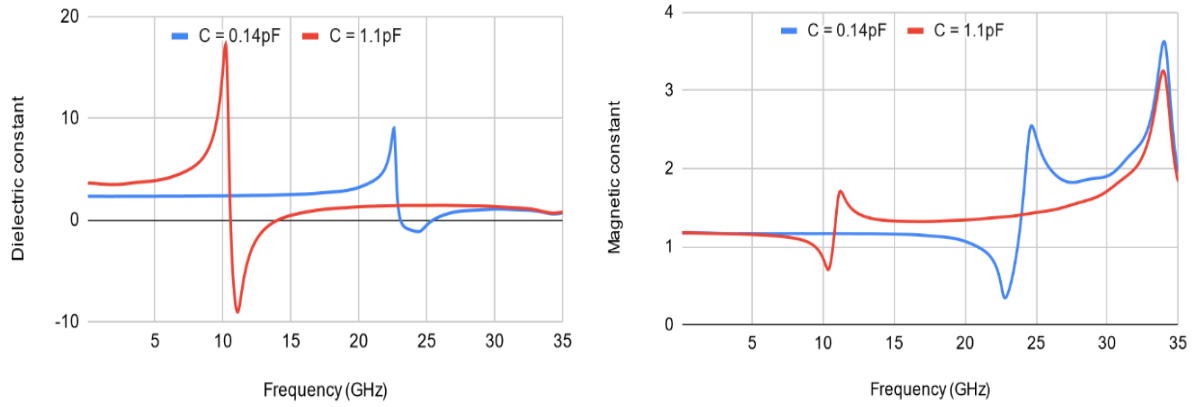
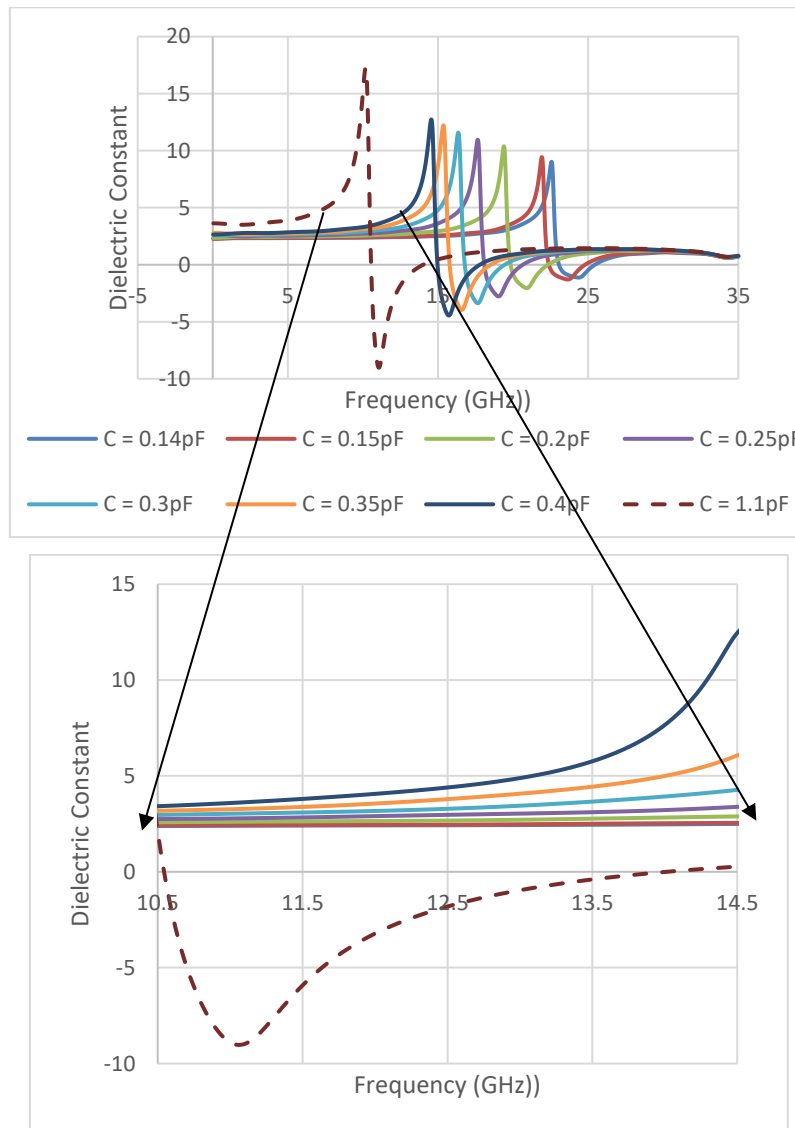


Fig. 4.2. Characteristics of varactor diode used in the new UC.



(a)



(b)

Fig. 4.3. (a) Extracted dielectric and magnetic constant for different capacitance values of varactor and (b) Range of possible dielectric constant.

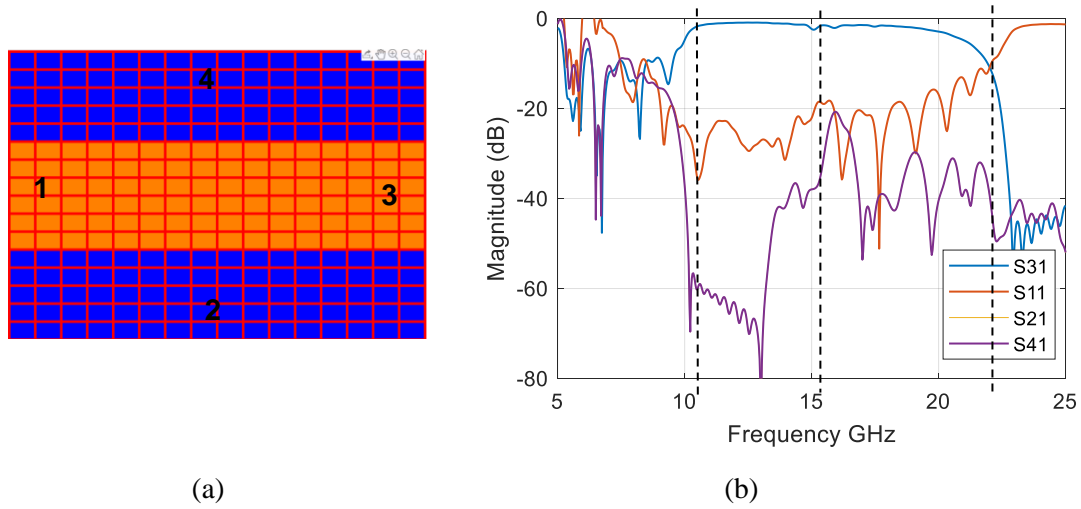


Fig. 4.4. (a) Six cells wide waveguide and (b) simulated S-parameters using CST

In most of the following tests, the 10.5 to 14.5 GHz window will be considered as the most performant operating band of FPMS 2.0 even if it is possible to use it up to 20 GHz roughly from a practical point of view.

4.3 FPMS 2.0

FPMS 2.0 is made up of 256 new unit cells (described in previous section) arranged in a 16x16 matrix structure as shown in Fig. 4.5. It depicts the top view of every layer incorporated in the new unit cell design. In terms of size this structure is 40mm by 40mm (each cell is 2.5mm square). It is corresponding to $2\lambda_g$ at 10GHz with a dielectric constant of 2.2. With including the transitions, the total size of the board becomes 58mm by 58mm.

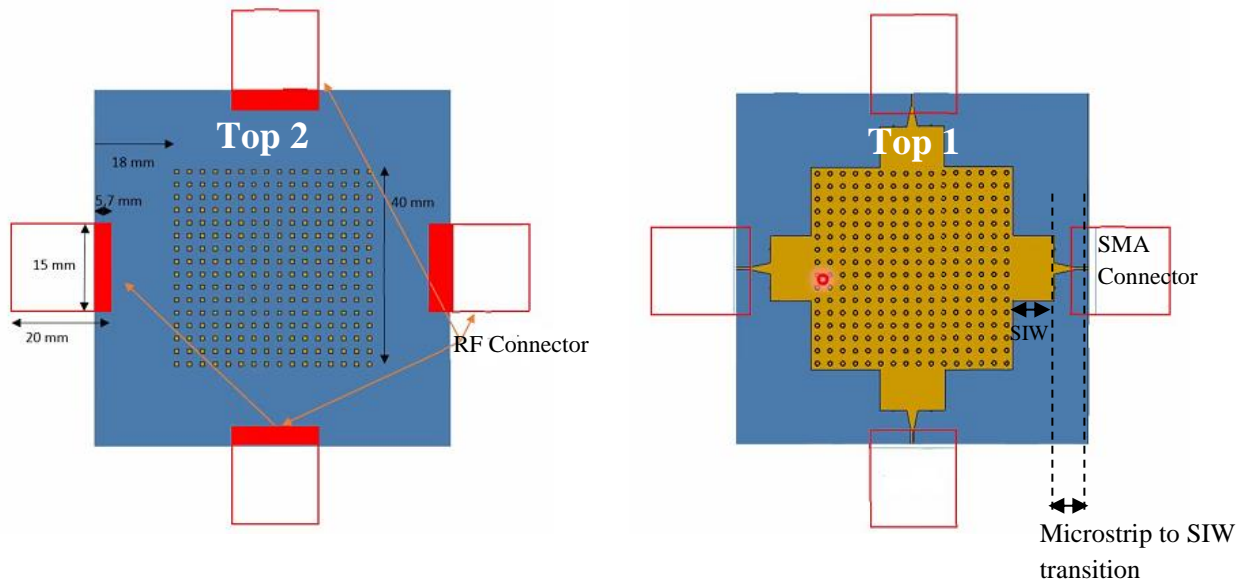


Fig. 4.5. CST Model of FPMS2.0

We have first simulated a 16x16 FPMS structure to implement waveguides. We control each cell by changing the capacitance of the diode model. To simplify the first simulation, we only used the two extreme values of capacitance provided by the varactor diode, $C = 0.14\text{pF}$ corresponding to a positive dielectric constant configuration of the UC and $C = 1.1\text{pF}$ corresponding to a negative dielectric constant configuration. Two different six unit cells wide waveguides are tested using CST, one is straight that goes through the total length of the FPMS 2.0 as discussed in the previous section (see Fig. 4.4) and the second one is a bended waveguide as shown in Fig. 4.6. Similar to the straight waveguide, for the bended waveguide also isolation is very poor beyond 14.5GHz due to the fact that both ON and OFF cells have positive dielectric constant. The E-field distribution in straight waveguides at different frequencies are shown in Fig. 4.7. As expected, when we are out of the 10.5 – 14.5 GHz window where the OFF cells have a negative dielectric constant, the waveguide mode is less confined in the ON cells and obviously leaks towards the other ports (ports 2 and 4) as seen in Fig. 4.7. For the straight waveguide, the insertion loss is between 2 to 3 dB and the return loss between 10.5 and 14.5 GHz is above 20 dB. For the bended waveguide, it becomes worse by around 2 dB, which is anticipated at such high frequencies due to the bend in the path of the wave. Thus, these results are considered well within acceptable range as compared to 1st generation of FPMS with 4dB insertion loss and 8.5dB return loss for the same waveguide structure. This configuration will be a good starting point for future optimizations.

Since the CST simulations take 2 hours per simulation on a regular computer therefore an equivalent model shown in Appendix 5 has been developed in ADS to run faster such simulations. First, the straight and bended waveguide structures are simulated using ADS and have been compared to CST simulations. The comparison between the ADS and CST softwares is quite satisfactory as shown in Fig. 4.8. Therefore, for the rest of the chapter we will use ADS simulations.

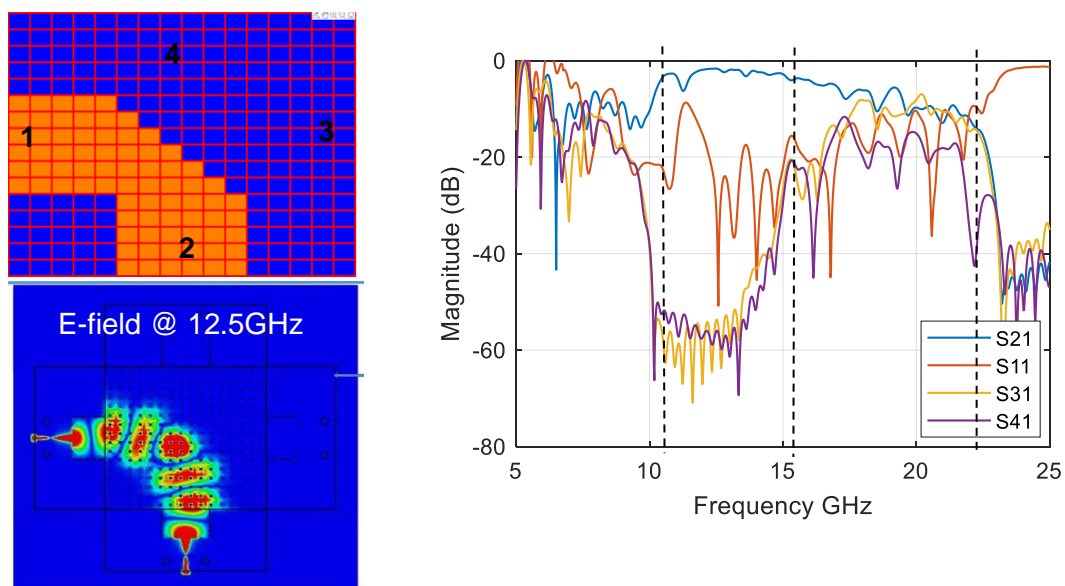


Fig. 4.6. Bended waveguide simulation using CST

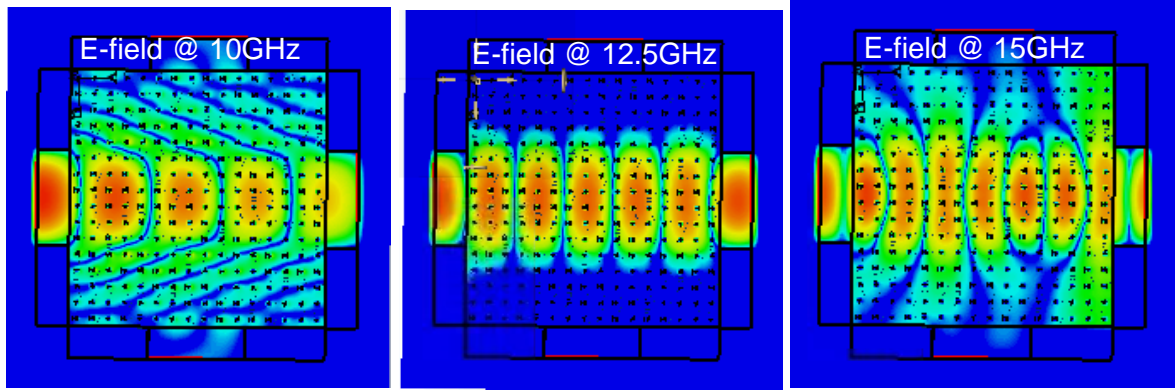


Fig. 4.7. E-field distribution of straight waveguide

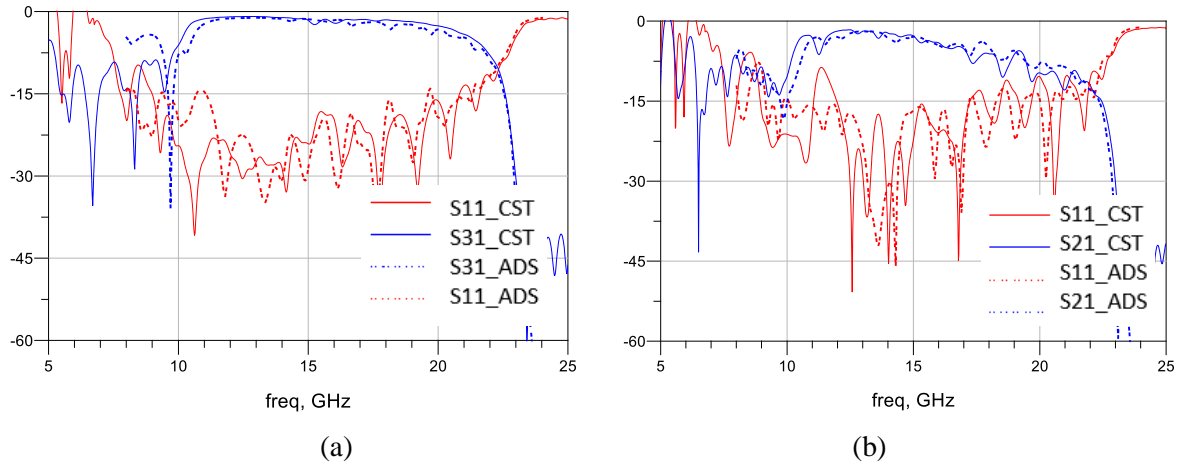


Fig. 4.8. CST and ADS results comparison (a) Straight waveguide and (b) Bended waveguide.

The effect of different widths of a straight waveguide is depicted in Fig. 4.9. The lower cut off frequency of the waveguide decreases as we increase the width which is obvious and the upper cut off frequency remains same for all the cases (around 23 GHz) as it is limited by the frequency when the ON cells ($C=0.14\text{pF}$ in this case) start to have a negative dielectric constant (see again Fig. 4.4(b)). Out of the three cases, return loss is highest for the six cells wide waveguide since the device and its SMA to SIW transitions were optimized for this configuration.

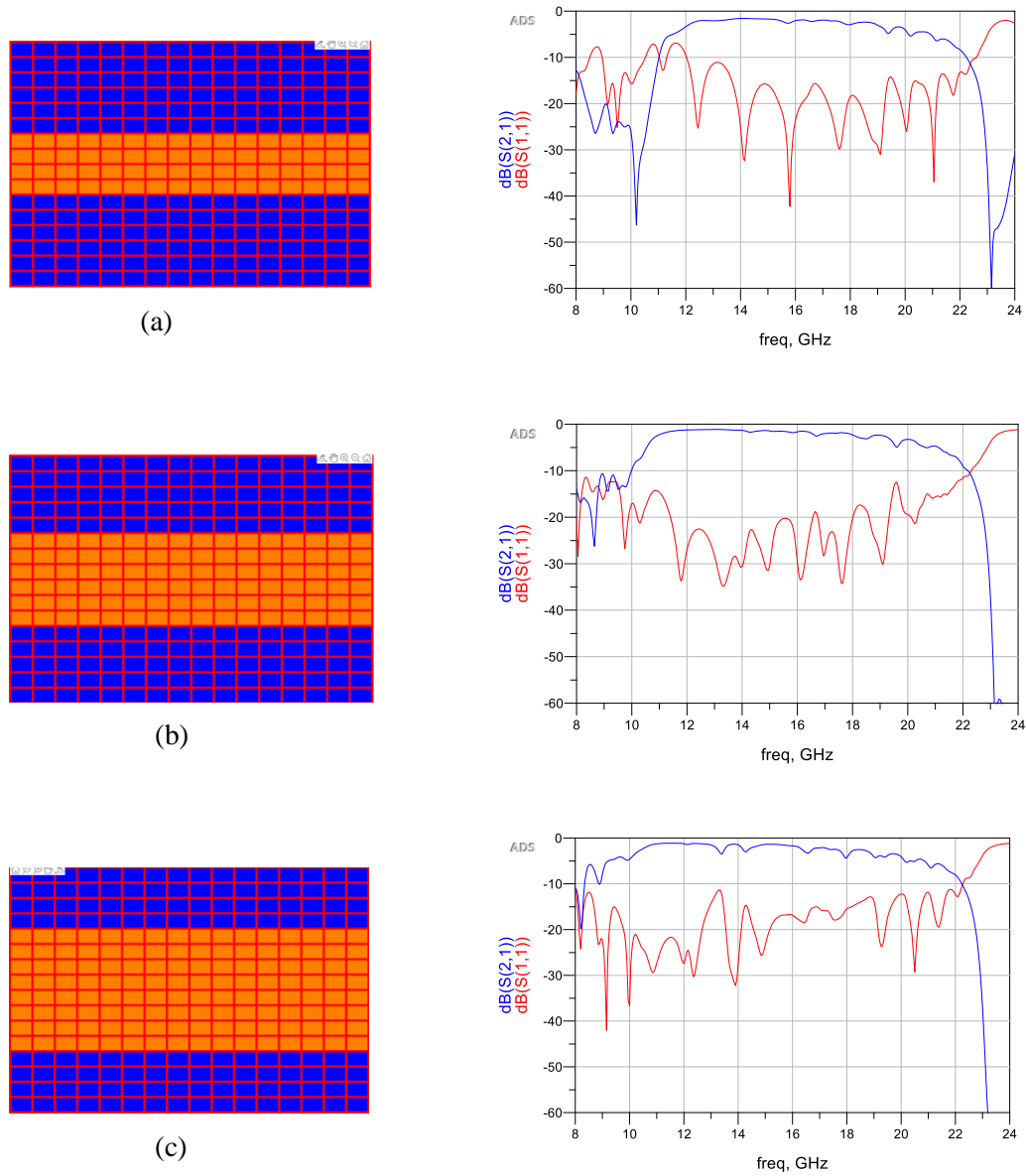


Fig. 4.9. Straight waveguide (a) 4 cells wide, (b) 6 cells wide and (c) 8 cells wide.

In the next section, we will present the different microwave functions that can be realized using FPMS 2.0 and compare its performances with the previous generation of FPMS.

4.4 Different Microwave Functions using FPMS 2.0

This sections presents the various microwave functions achievable through FPMS 2.0 that were made using the first generation of FPMS in Chapter 2 & 3.

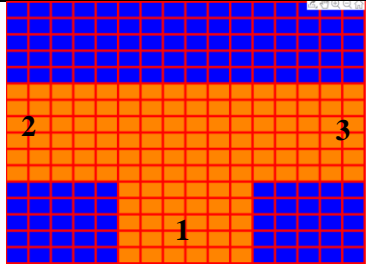
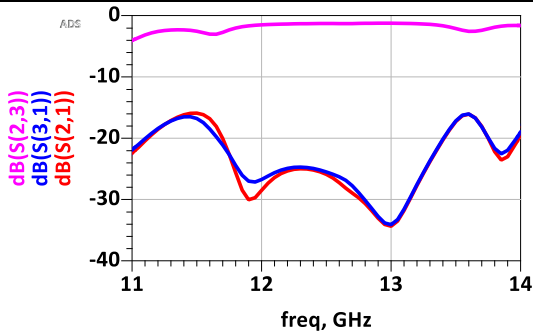
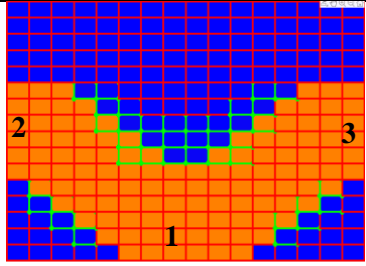
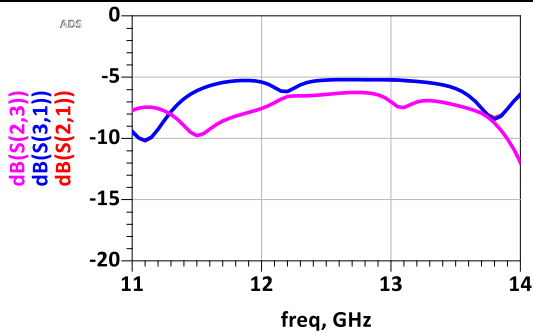
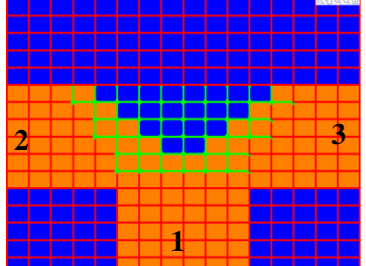
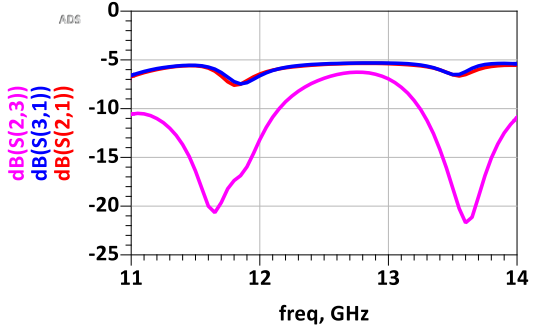
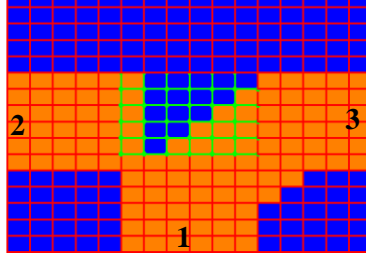
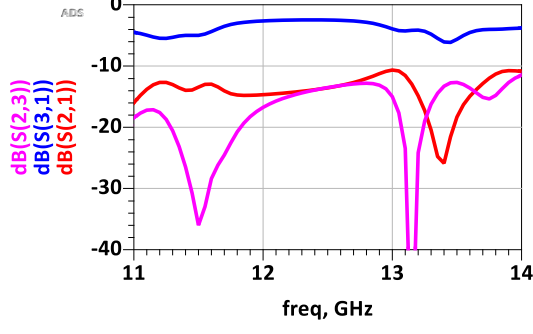
Power Divider

First, we have tested the different power divider configurations optimized in the previous chapter (even, balanced and unbalanced) using the 2nd generation of FPMS and obtained the results presented in Table 4.1. The initial case is the starting point for all these tests and the other cases are derived from this one. The insertion loss for power divider built with FPMS 2.0 is nearly reduced to half as compared to the 1st generation of FPMS. For example, the balanced power divider configuration implemented with 1st generation of FPMS has insertion loss of around 10dB but with FPMS 2.0 it is around 6dB. For the even power distribution case, $|S_{23}|$ is slightly lesser than $|S_{21}|$ and $|S_{31}|$ but these initial results are obtained without using any optimization algorithm. These results are promising starting points to create such functions with the FPMS 2.0. From our previous experience, the equivalent model for these simulations only give an approximate, yet satisfactory behavior of the whole structure for these early stage tests. Considering the individual tuning capability of each cell of this generation, we think that such power divider can be further improved using the live optimization as discussed in Chapter 3 once the FPMS 2.0 board will be made.

Switch

Next, we have tested the switching capacity of FPMS 2.0. since, it has 4 ports, we get six ON and OFF states as presented in the table in Appendix 4. For all the configurations, the insertion loss when the two ports are connected i.e the ON state is 2dB and the isolation is greater than 30dB from 11 GHz to 14 GHz. The isolation value is much higher (60 to 100dB) when the operating band, starting at 11 GHz, is reduced to 13GHz and 12 GHz respectively. The return loss for all these cases is around 15dB. The performance of this switch is much better as compared to the first generation in terms of insertion loss. The insertion loss for the first generation is 4dB whereas it is 2dB with FPMS 2.0.

Table 4.1: Power divider configuration and simulated results

Power Divider	Configuration	Simulated S-parameters
Initial		
Even		
Balanced		
Unbalanced		

Phase Shifter

Then, we move to phase shifting capability of FPMS 2.0. Here, we have changed the capacitance values of ON cells of a straight six cells wide waveguide from 0.14pF to 0.4pF to realize a phase shifter. The simulated S-parameters of the phase shifter built with FPMS 2.0 is shown in Fig. 4.10. The min and max

value of the insertion loss is 1.27 dB and 4.42 dB respectively. The average insertion loss of the phase shifter is 1.15 dB and total phase shift is 220° at 12.5 GHz which gives the figure of merit $191^\circ/\text{dB}$. It is much higher than $39.22^\circ/\text{dB}$ which was obtain with the first generation of FPMS thanks to the lower insertion loss of this new generation. The return loss is better than 20dB at 12.5GHz and better than 11dB from 11 to 14GHz.

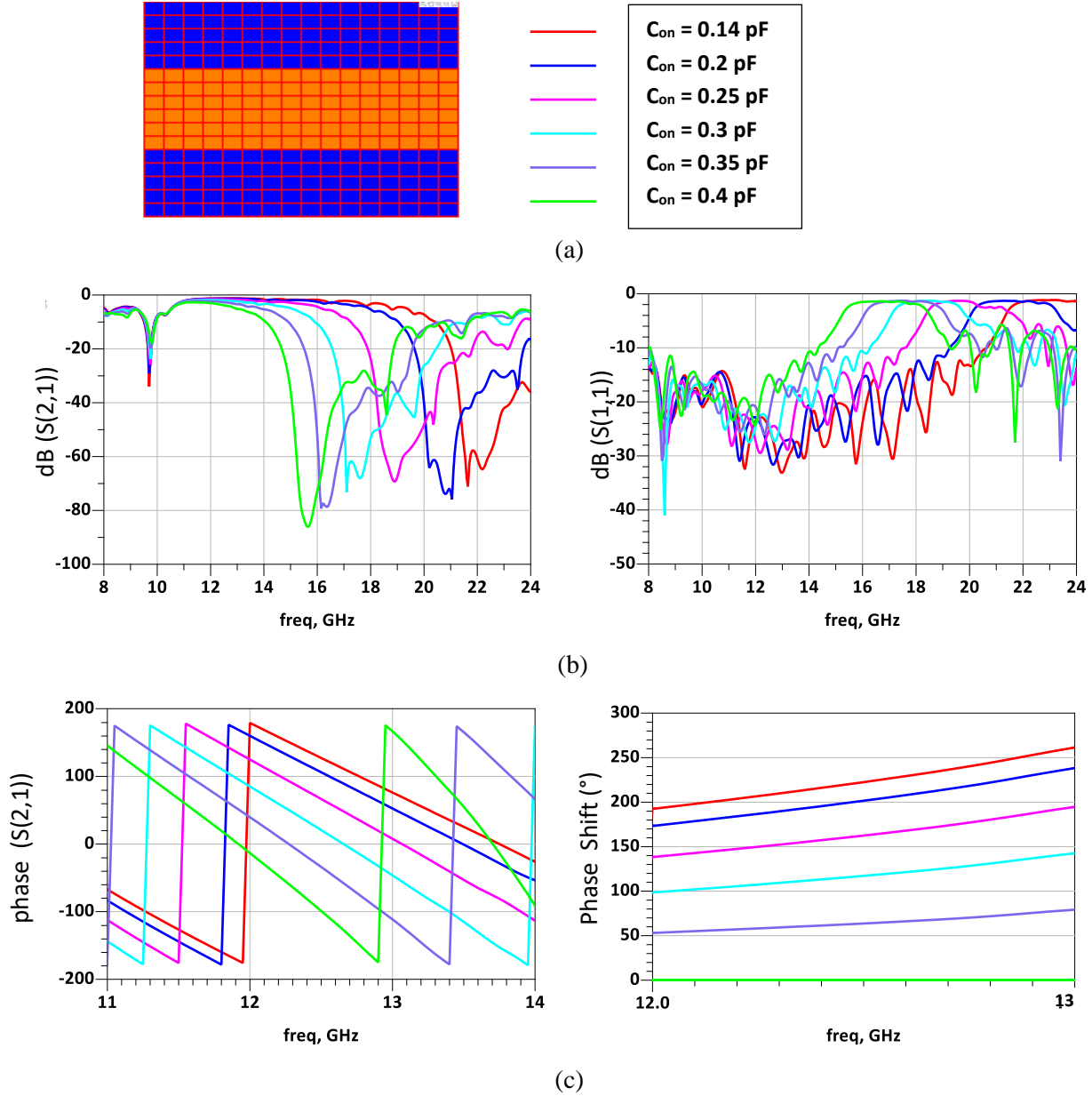


Fig. 4.10. Phase Shifter (a) Straight waveguide structure, (b) insertion loss and return loss and (c) Phase of S_{21} and phase shift in degrees.

Attenuator

Then, we have tested the isolation achieved using the 2nd generation of FPMS. Using the same way as before, we have turn OFF the last column of unit cells step by setp as shown in Fig. 4.11(a). The simulated S-parameters of attenuator are shown in Fig. 4.7(b). The frequency range to achieve a good

isolation is between 11 GHz to 14 GHz. The isolation value varies from 20 dB to 100 dB at 11.35 GHz and gets lower as we move towards 14GHz as shown in Fig. 4.11(b). This behavior is clearly because the evolution of the OFF cells equivalent dielectric constant as studied in section 4.2 (see Fig.4.2). The dielectric constant of an OFF cells has a minimal value at 11.35 GHz and starts increasing towards 0 around 14GHz. The OFF cell thus is not as good when reflecting the input wave as the frequency increases.

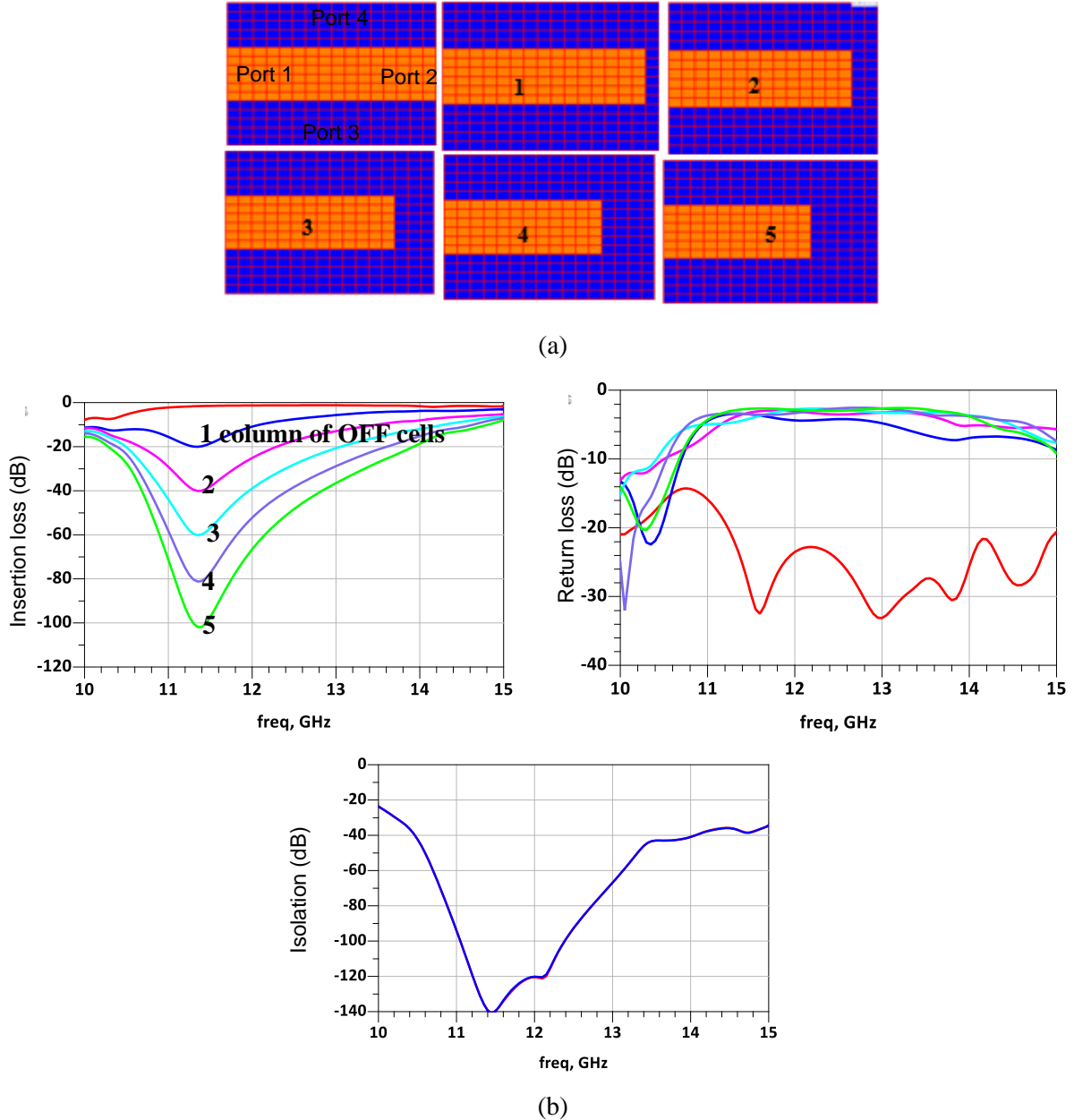


Fig. 4.11. (a) Straight waveguide based attenuator when 1,2,3,4,5 column of OFF cells are applied and (b) simulated insertion loss, return loss and isolation (between port 1 & 3 or port 1 & 4) in dB.

In the next section we will now present some other microwave functions implemented using FPMS 2.0 that were previously not possible with the first generation of FPMS.

4.5 New Components from FPMS 2.0

FPMS 2.0 has some distinctive features apart from working in higher frequency range and lesser losses, such as it has more number of ports and most importantly, we can individually bias each unit cell of FPMS2.0 by any value defined by the characteristics of the varactor diode. This section will present some of the the components that can be realized using these properties of FPMS 2.0.

Two bended waveguides

Since this new generation of FPMS has four ports, we can simultaneously built two bended waveguide structures as shown in Fig. 4.12(a). The simulated S-parameters of the two bended waveguides are shown in Fig. 4.12(c). The insertion loss and return loss are same for both the waveguide. The isolation between port 1 & 2, port 1 & 4, port 3 & 2 and port 3 & 4 between frequency 11GHz to 13 GHz is better than 20dB and is shown in Fig 4.12(b). This isolation is maximum at 11.35GHz with S_{34} and S_{14} equal to -52dB and -65dB respectively. This is consistent to what was seen in the previous section when 2 to 3 rows of OFF cells are used to isolate a signal between two ports. If more isolation is required in the future, a bigger marix will be needed to create more OFF cells between the isolated ports. A live optimization of this case will be interesting to improve the return loss of the bended waveguides.

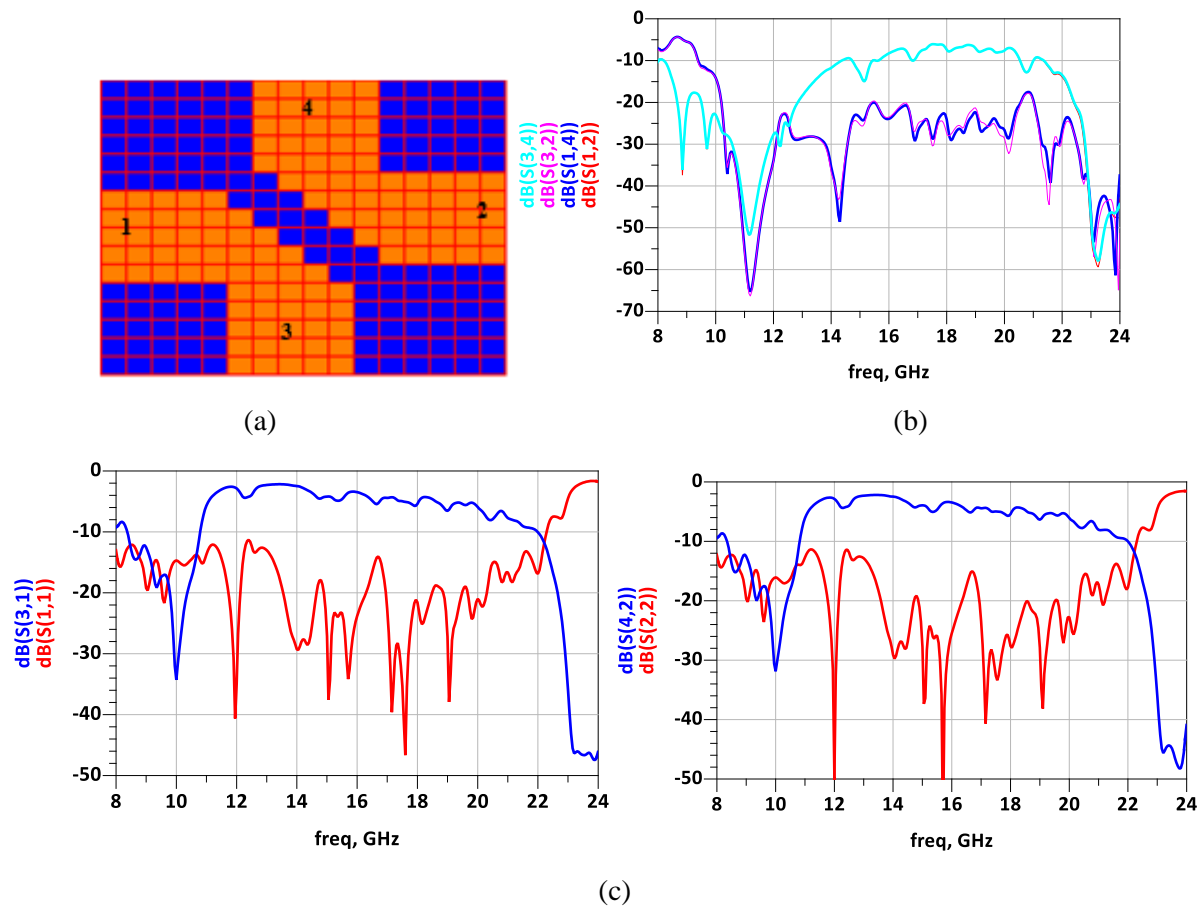


Fig. 4.12.(a) Two bended waveguide, (b) Isolation and (c) Simulated insertion and return loss

Band stop filter

This new generation of FPMS allows us to individually tune all the unit cells, which means each ON cell can now have different capacitance value and therefore different positive dielectric constant. Using this advantage of FPMS 2.0, we have built a band stop filter with one column in the middle of the waveguide structure having different capacitance value. One can manually tune the capacitance of these unit cells or use the optimization algorithms. First, we have manually tuned the capacitance to create a stop band around different frequencies. We can increase the value of the capacitance for the middle column of cells from 0.14pF (minimum value) to 1.1pF (maximum value). After tuning we have found band stop effect at 12 GHz, 13 GHz and 14 GHz with capacitance values of 0.92pF, 0.74pF and 0.6pF respectively. The band stop filter and its simulated S-parameters are shown in Fig. 4.13(a). Based on what was studied in section 4.4 using two columns of OFF cells will make the band stop more reflective and still tunable in frequency as well as shown in Fig. 4.13(b). We have then the capability to tune the reflection coefficient by using more or less columns.

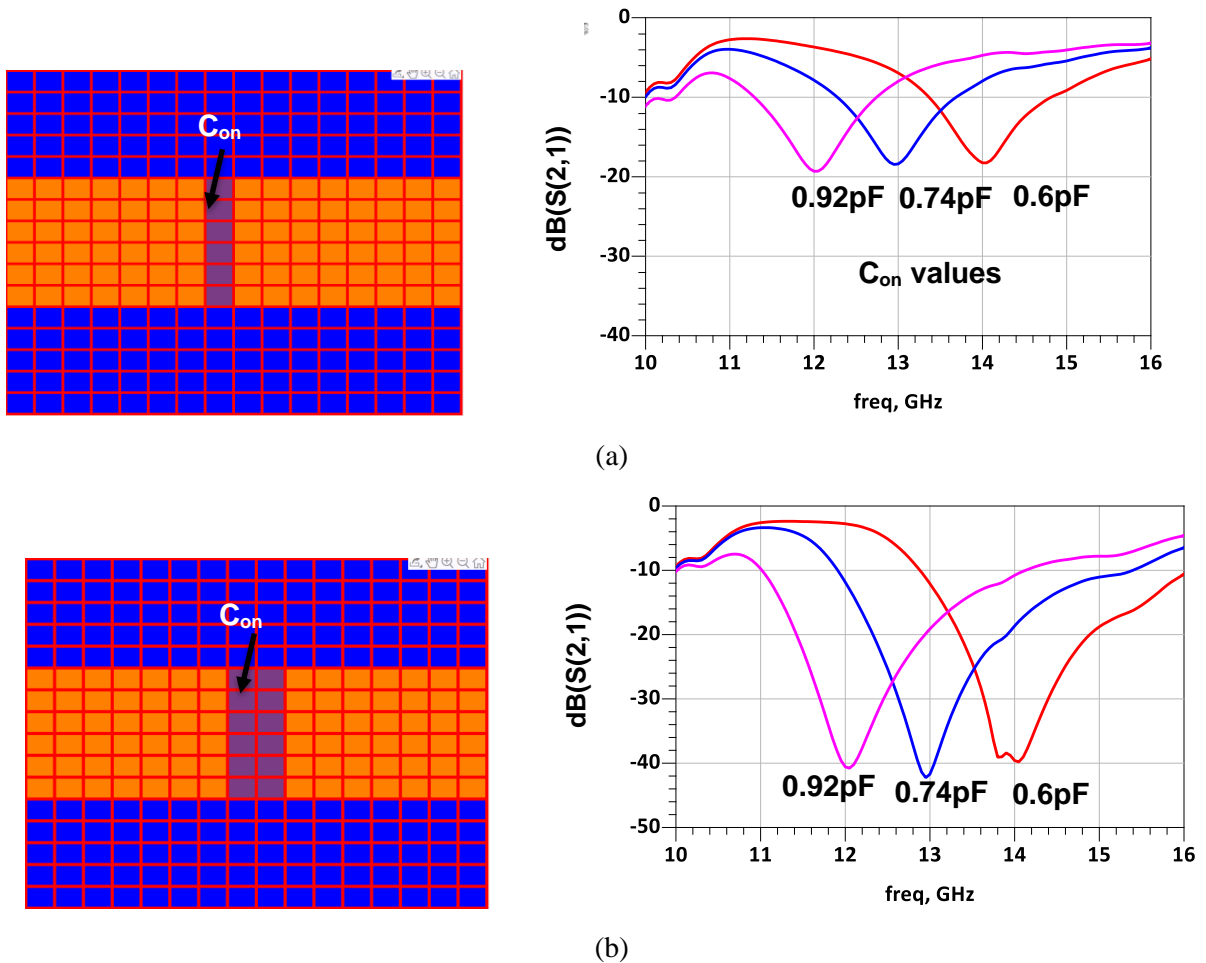


Fig. 4.13. Band stop filter and simulated S-parameters at different frequencies for (a) one column and (b) two columns of cells with variable capacitance.

Next, we have tried to realize a tunable band stop filter by tuning its central frequency or bandwidth by creating two independent notches at different frequencies. It can be achieved by considering two or more columns of unit cells in the waveguide structure and changing their capacitance values individually. The two columns with variable capacitance values placed side by side and its simulated S-parameters are shown in Fig. 4.14(a). The capacitance values of the two columns are denoted by C_{1on} and C_{2on} which are 0.95pF and 0.32pF for this case. Then, we have fixed the capacitance value C_{1on} and tune the C_{2on} (0.32 to 0.72pF) to obtain the results shown in Fig. 4.14(b). We can observe that the second notch at high frequency that is driven by C_{2on} can indeed be tuned without changing the first notch location. In the case where C_{2on} equals 0.72pF, a two pole band stop behavior can be created around 12.5 GHz with a reflection coefficient better than -20dB on a ~2GHz bandwidth. Using such mechanism, we can modify the band stop bandwidth and this effect with the previous tested cases.

If the two columns with variable capacitance values are not placed side by side and distance between them keeps increasing, there is no major difference on the simulated positions of the two notches as presented in Table 4.3. A noticeable change can be seen however in the S_{21} between 13 and 17 GHz and will have to be taken into care of once the live optimization will be applied on this device. The band pass behavior in this frequency range may be exploitable to create tunable band pass filters with this device.

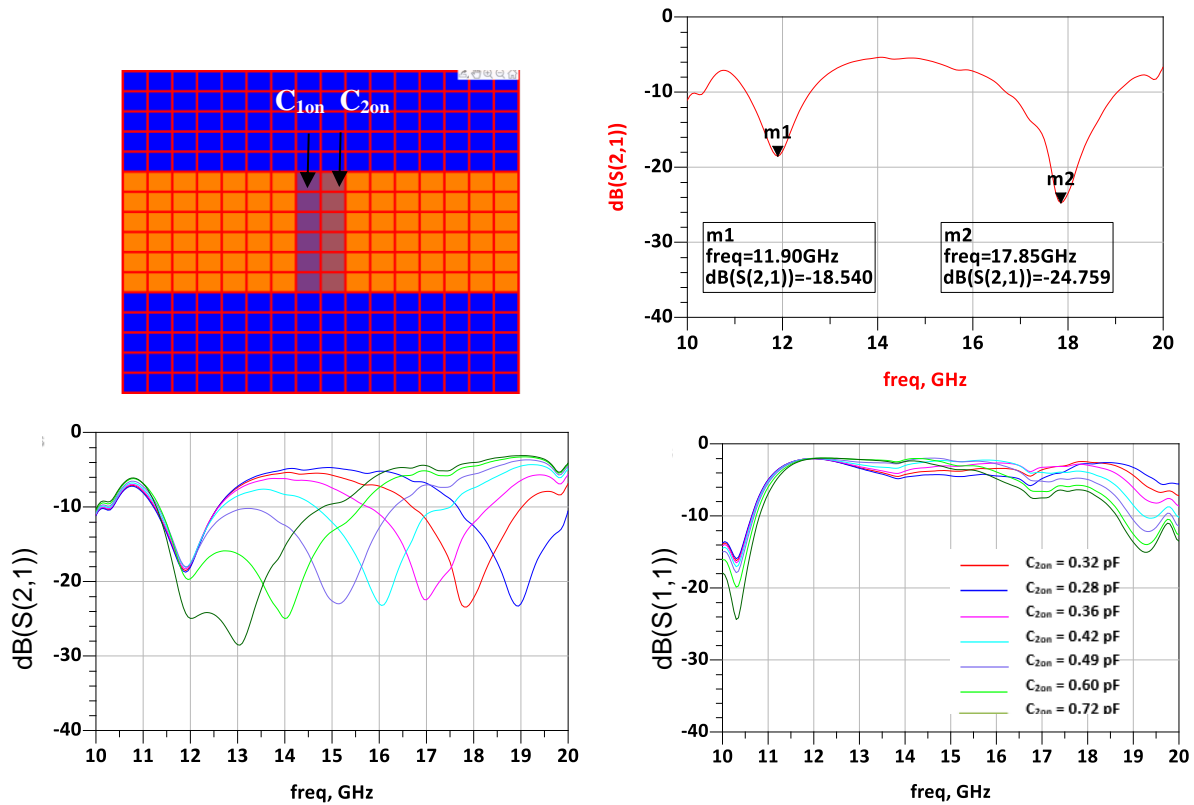
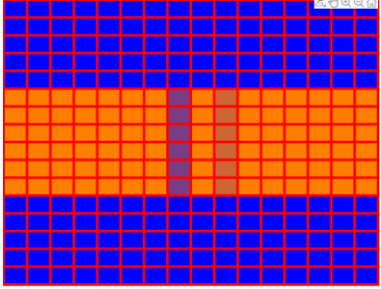
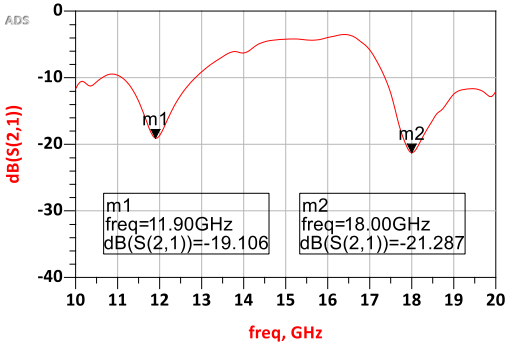
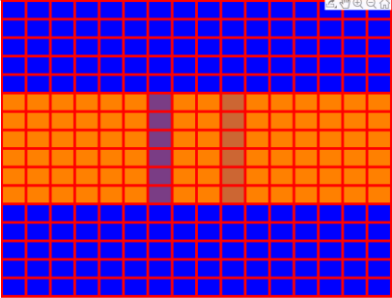
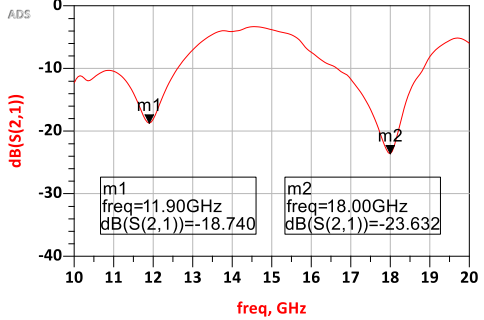
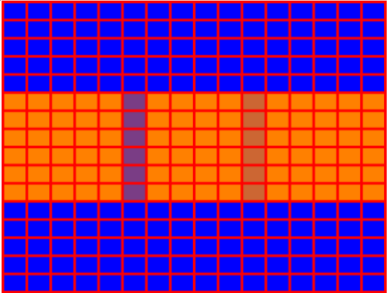
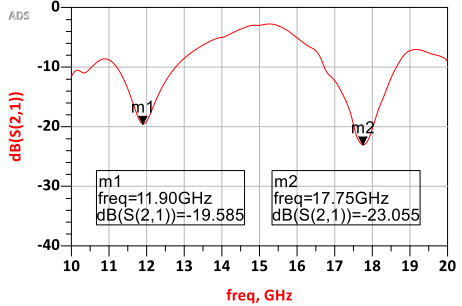
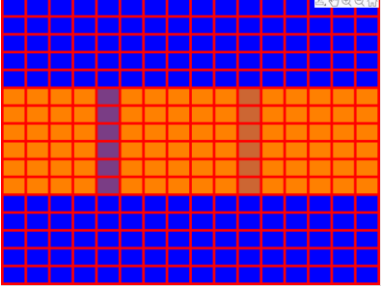
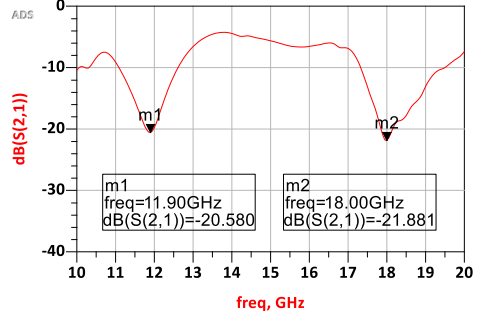
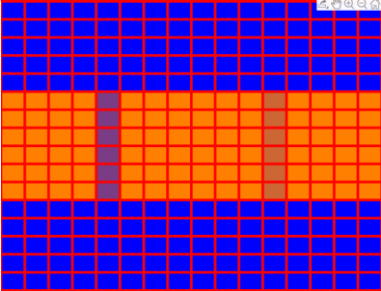
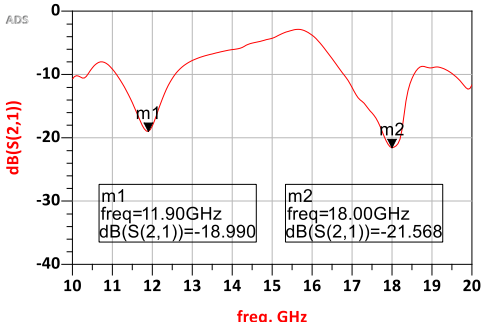


Fig. 4.14 Band stop filter and its simulated S-parameters for two columns of cells with different capacitance values.

Table 4.2: Band stop filter and simulated S-parameters

Band stop filter	Simulated S-parameters
	 <p>ADS</p> <p>$dB(S(2,1))$</p> <p>freq, GHz</p> <p>m1 freq=11.90GHz $dB(S(2,1))=-19.106$</p> <p>m2 freq=18.00GHz $dB(S(2,1))=-21.287$</p>
	 <p>ADS</p> <p>$dB(S(2,1))$</p> <p>freq, GHz</p> <p>m1 freq=11.90GHz $dB(S(2,1))=-18.740$</p> <p>m2 freq=18.00GHz $dB(S(2,1))=-23.632$</p>
	 <p>ADS</p> <p>$dB(S(2,1))$</p> <p>freq, GHz</p> <p>m1 freq=11.90GHz $dB(S(2,1))=-19.585$</p> <p>m2 freq=17.75GHz $dB(S(2,1))=-23.055$</p>
	 <p>ADS</p> <p>$dB(S(2,1))$</p> <p>freq, GHz</p> <p>m1 freq=11.90GHz $dB(S(2,1))=-20.580$</p> <p>m2 freq=18.00GHz $dB(S(2,1))=-21.881$</p>
	 <p>ADS</p> <p>$dB(S(2,1))$</p> <p>freq, GHz</p> <p>m1 freq=11.90GHz $dB(S(2,1))=-18.990$</p> <p>m2 freq=18.00GHz $dB(S(2,1))=-21.568$</p>

In order to make these tunable notches more reflective, we again double the number of columns with variable capacitance values and get the results as shown in Fig. 4.15. As expected, the S_{21} values at 11.9 and 17.9 GHz change from -18.5 and -24.7 dB to -39.9 and -58.3 dB respectively for these two stop bands with a distinct control of their characteristics.

We can also increase the number of poles in a single band stop filter by adding one more column whose capacitance value can be controlled as depicted in Fig. 4.16. If we tune C_{1on} , C_{2on} and C_{3on} individually (see Fig. 4.16), we can create a band stop filter with a reflection coefficient better than -30dB between 13 and 15 GHz.

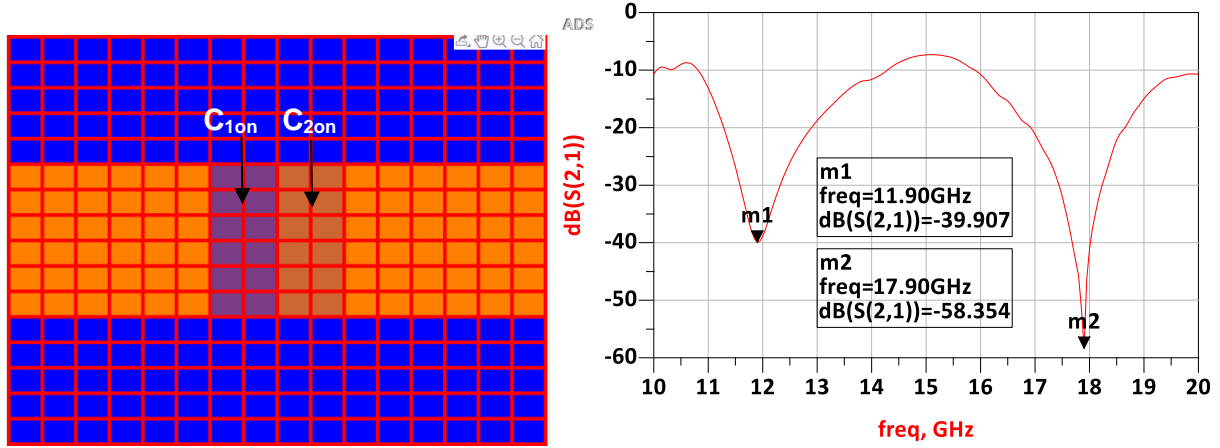


Fig. 4.15. Band stop filter with four columns of cells with variable capacitance values.

Obviously, a combination of all those different cases can be made, giving valuable clues of the capability of this FPMS 2.0 to create a single fully tunable band stop filter and/or different tunable notches with an individual control of their characteristics. With the real prototype and the developed optimization algorithms, it should be possible to tune their frequency, bandwidth, order and level of reflection on the fly.

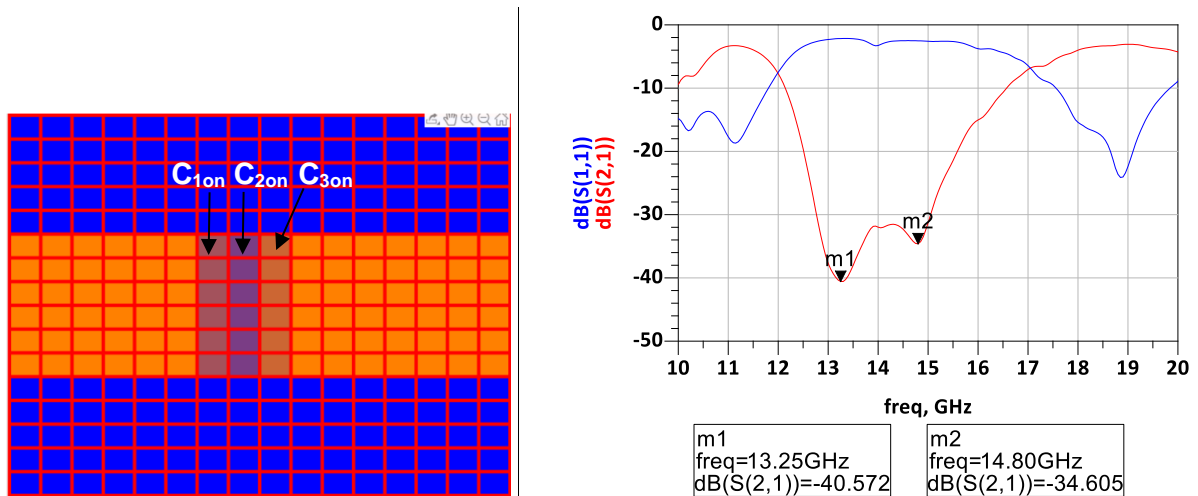


Fig. 4.16. Third order band stop filter with three columns of cells with variable capacitance values.

4-Ports Power Divider

A 4-port power divider using FPMS 2.0 is simulated as shown in Fig 4.17. The simulated results clearly show that power distribution is symmetrical between all the ports and the insertion loss can be improved if the capacitance values of the middle unit cells of FPMS 2.0 is changed. This improvement is achieved just by manual adjusting; it can be better once the optimization techniques will be applied on the manufactured prototype but is an encouraging starting point.

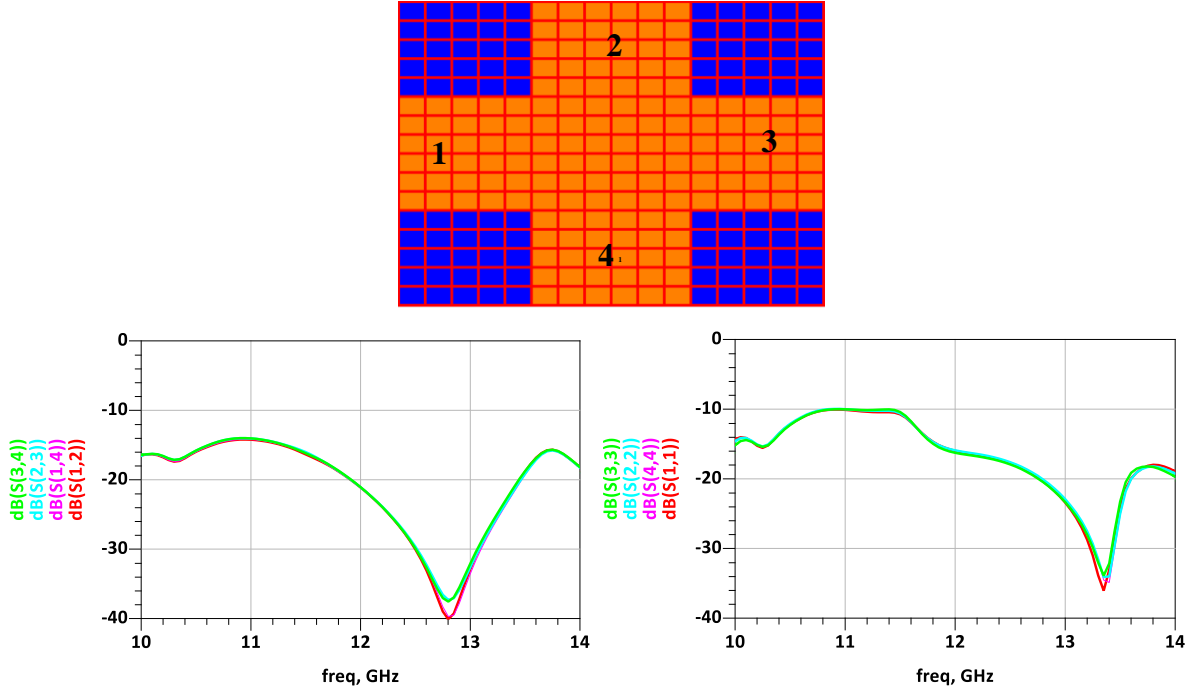


Fig. 4.17. 4-Ports Power Divider initial configuration with simulated S-parameters

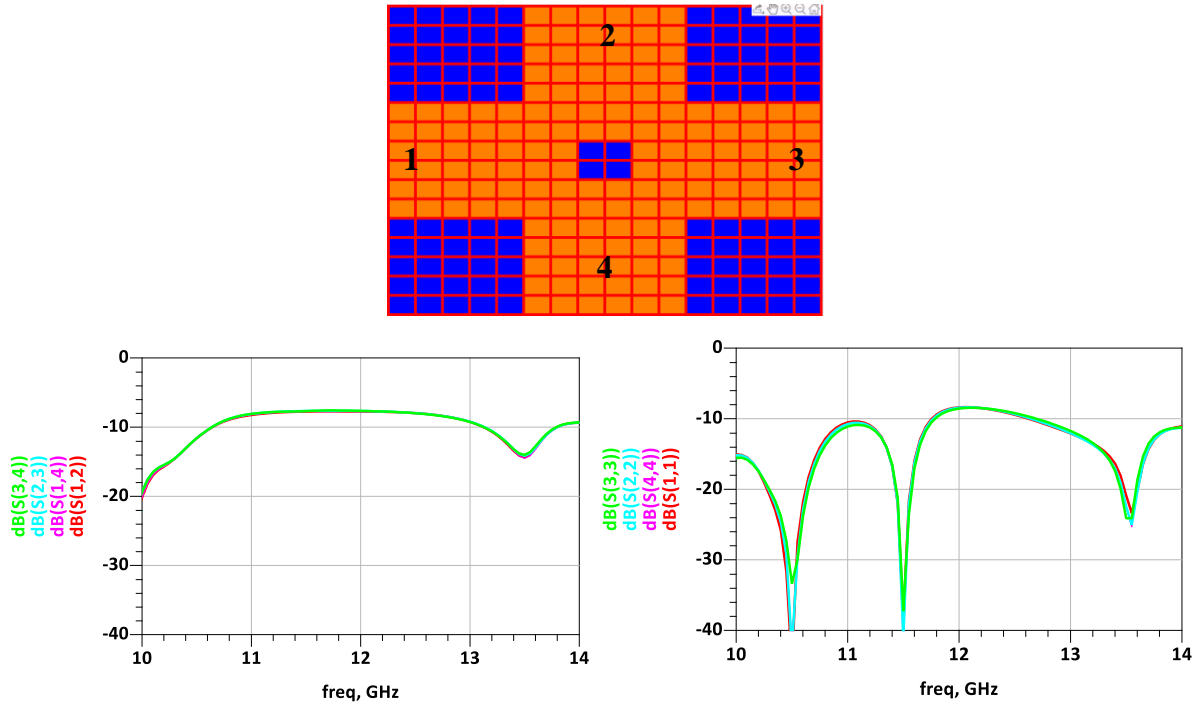


Fig. 4.18. 4-Ports Power Divider configuration after manual tuning with simulated S-parameters.

The individual tuning of each unit cell in FPM 2.0 has a great potential to investigate various other capabilities and this aspect will be addressed in future work.

4.6 Comparison between FPMS 2.0 with previous devices

The capability of FPMS 2.0 to realize different microwave components at this early stage of testing shows promising results. In order to give an overview, Table 3.2 from Chapter 3 is updated here by adding FPMS 2.0 potential to realize reconfigurable devices (see Table 4.4).

The major drawback of first generation of FPMS was high insertion losses and it is improved in FPMS 2.0 that too with higher frequency band. The individual tuning capability of each cell and more number of ports gives scope to explore some more function using FPMS 2.0 which is left for future work. Considering the first results seen here, creating band pass filters looks feasible between two stop bands for example since it is possible to individually control their characteristics. It still has to be tested especially to see the level of insertion and return losses that can be accessible. With the four ports and the capability to individually reconfigure the propagation between ports, reconfigurable couplers and their numerous variants such as frequency-reconfigurable, power-dividing ratio (PDR)-reconfigurable frequency- and PDR-reconfigurable and phase-reconfigurable couplers could be tested. Ideally, multifunctional fusion reconfigurable couplers that can integrate multiple functions into a single device such as frequency-reconfigurable filtering or PDR-reconfigurable balanced couplers [11] is potentially an investigation area where the FPMS can play a role.

Table 4.3: Reconfigurable Multi-functional Microwave Components

Reference	[1]	[2]	[3]	[4]	[5]	FPMS (This work, [6], [7], [8], [9], [10])	FPMS 2.0
Reconfigurable Method	p-i-n diode	Bonding wire	PCM	S/w & p-i-n diodes	Tuning resistance	Varactor diodes	Varactor diodes
Frequency range (GHz)	2-3	2-4	2-10	2.5-3.5	0.78-1.11	0.9-3	11-14
Insertion loss (dB)	2.8 to 3.4	3.7 to 4.7		1.6-2.7	3-7	3.99-6.62	2-4
General Comment		Not on the fly reconfigurability	No experimental demonstration	External control by FPGA			4 ports, individual tuning
Functions	Antenna	✓		✓	✓	✓	✓ *
	Bandpass filter	✓	✓		✓	✓	**
	Bandstop filter		✓			✓	✓
	Coupler		✓		✓		**
	Power Divider		✓		✓	✓	✓
	Attenuator				✓	✓	✓
	Phase Shifter					✓	✓
	Signal Routing					✓	✓

* Work in progress by IETR

** Not tested yet

4.7 Conclusion

In this chapter, we have presented the next generation of Field Programmable Microwave Substrate i.e. FPMS 2.0 which has been designed to work in higher frequency band. FPMS 2.0 has been made up of Rogers 5880 dielectric substrate which has relatively low dielectric loss tangent (0.001) as compared to the FR4 (0.02) used in the first generation of FPMS that improves the performance of all the functions by decreasing the losses. The unit cells of FPMS 2.0 is designed in a way to have individual biasing control that was not possible with the first generation of FPMS. The simple waveguide structure has been implemented using FPMS 2.0 which has simulated insertion loss of 2 dB and return loss less than 15dB from 11 GHz to 14GHz. Then, different other components such as power divider, switch, phase shifter and attenuator are realized using FPMS 2.0. All of them had better performances in terms of losses which was one of our main goal. After that, we have realized some new functions using FPMS 2.0 such as two bended waveguide at the same time and a 4-port power divider that uses four ports. A

different way to realise a bandstop filter by having different capacitance values of the ON cells is demonstrated with a strong capability to tune its central frequency, bandwidth and reflection coefficient individually. There are numerous other possibilities that can be explored with FPMS 2.0 and these will be investigated in future work. At this stage and compared to existing highly reconfigurable devices from the literature (see Table 4.4), the FPMS in its generation 2 may be the most reconfigurable device existing so far at this frequency range (10.5 to 14.5 GHz) with such insertion losses (2 to 4 dB). The experimental tests ahead along with their optimization is however a critical milestone and will help gathering measured metrics of its true performances.

4.8 References

- [1] Alejandro L. Borja, Yasin Kabiri, Angel Beleaguers and James R. Kelly , “Programmable Multifunctional RF/Microwave Circuit for Antenna and Filter Operation,” *IEEE Transactions on Antenna and Wave Propagation* , vol 66, no.8 pp.3865-3876, Aug 2018
- [2] David A. Connelly, and Jonathan D. Chisum, “Dynamically Reconfigurable Microwave Circuits Leveraging Abrupt Phase Change Material”, *IEEE Transactions on Microwave Theory and techniques*, vol. 68,no. 10, pp 4188-4205, Oct 2020.
- [3] Yo-Shen Lin, Pei-Shan Lu, and Yu-Cheng Wu,, “A Novel Configurable Microwave Passive Component Based on Programmable Bridged-T Coil Array”, *IEEE Transactions on Microwave Theory and techniques*, vol.69, no. 6,pp. 3001-3014, Jun. 2021
- [4] Lei Sang, Ziyang Liu, Shuaitao Li, Wen Huang, Ping Li and Hao Tu “A Programmable Microwave Components Reconfigurable Between Four Functions” *IEEE Transactions on components, packaging and manufacturing technology*, vol. 13, no. 1, january 2023
- [5] Jonathan M. Knowles, Hjalti H. Sigmarsson, and Jay W. McDaniel , “Design of a Symmetric Lumped-Element Bandpass Filtering Attenuator (Filtenuator)”, 2022 IEEE 22nd Annual Wireless and Microwave Technology Conference (WAMICON).
- [6] N. Jess, B. A. Syrett, and L. Roy, “The field-programmable microwave substrate,” *IEEE Transactions on Microwave Theory and techniques*, vol 64, no. 11,pp. 3469–3482, Nov. 2016.
- [7] Hanyue Xu, Ying Wang, Farhan A. Ghaffar, and Langis Roy, “Reconfigurable Microwave Filters Implemented Using Field Programmable Microwave Substrate” , *IEEE Transactions on Microwave Theory and techniques*, vol. 69,no. 2, pp 1344-1354, Feb 2021.
- [8] Aarefa Saifee, Christophe Duroiseau, Aurelien Perigaud, Nicolas Delhote, Fahad Farooqui, Ying Wang and Langis Roy “Reconfigurable Microwave Components Implemented using Field Programmable Microwave Substrate”, *IEEE MTT-S International Conference on Electromagnetic and Multiphysics Modeling and Optimization* 2022.

- [9] Aarefa Saifee, Christophe Duroiseau, Aurelien Perigaud, Nicolas Delhote, Fahad Farooqui, Ying Wang and Langis Roy “Reconfigurable Microwave Components Based On Optimization of Field Programmable Microwave Substrate”, IEEE- MTT-S International Microwave Symposium (IMS), 2023. (Accepted)
- [10] David René-Loxq , Olivier Lafond , Mohamed Himdi , Langis Roy, and Farhan Ghaffar, “Reconfigurable Half-Mode SIW Antenna Using Uniaxial Field Programmable Microwave Substrate Structure” IEEE Transactions on antennas and propagation, vol. 70, no. 11, November 2022
- [11] X. Tan and Y. Zhang, "Tunable Couplers: An Overview of Recently Developed Couplers With Tunable Functions," in IEEE Microwave Magazine, vol. 24, no. 3, pp. 20-33, March 2023, doi: 10.1109/MMM.2022.3226550.

Conclusion

In this thesis, we presented a reconfigurable device named Field Programmable microwave substrate (FPMS) that is capable of performing different microwave functions in a couple of seconds. Lots of work have been done for achieving tunability through different mechanisms as discussed in Chapter 1 but these methods are dedicated to a single microwave function. There are very less number of available devices that is capable of switching its role from one microwave function to another. Therefore, research needs to be done for the multi-functional reconfigurable microwave devices. It can save huge amount of time and cost in several applications including wireless communication.

Chapter 2 discusses the unit cell of FPMS and its components in detail, as well as the dielectric and magnetic constants and their relation to the biasing voltages of varactors. The operating frequency range of the FPMS is determined to be 0.9 to 3 GHz, and ON and OFF cells can be created to provide local positive and negative equivalent dielectric constants for creating waveguides and filters. A MATLAB-based optimization tool is introduced to enhance the performance of complex functions realized with the FPMS, using various optimization algorithms to simulate and optimize components. Successful simulations of diverse high-frequency devices are achieved using genetic algorithms with less than 30 iterations, but the time needed for optimization is related to the number of cells to optimize.

Chapter 3 presents different reconfigurable microwave components using the concept of the field programmable microwave substrate (FPMS) and a live optimization method based on actual measurement of the device S-parameters so that there is no discrepancy between simulation and measurement results. The designs include power dividers with tunable power dividing ratio, tunable notch, phase shifter, switch, and programmable attenuator. The optimization technique developed allows the S-parameter response of the device to be altered in real-time, achieving the best performance possible with the FPMS. A live optimization technique combined with the FPMS concept has successfully demonstrated the capability to achieve various tunable RF functions through a single FPMS board. The chapter also outlines optimization approaches that aim to decrease the number of variables that require optimization. The limitations of the current FPMS generation can be addressed in the next generation for improved performance of these components, leading to the potential for FPMS technology to attain a programmable microwave circuit design similar to that of FPGA in digital circuits.

Finally, the last chapter describes the development of the next generation of Field Programmable Microwave Substrate (FPMS) called FPMS 2.0, which is designed to operate in higher frequency bands. FPMS 2.0 is made of Rogers 5880 dielectric substrate, which has a low dielectric loss tangent, improving

the performance by decreasing losses. The unit cells of FPMS 2.0 have individual biasing control, which was not possible in the previous generation. Several components such as power dividers, switches, phase shifters, and attenuators have been realized using FPMS 2.0, showing better performance in terms of losses. New functions such as two-bended waveguides and a 4-port power divider have been demonstrated. A band stop filter with individually tunable central frequency, bandwidth, and reflection coefficient has also been realized. The chapter concludes by stating that there are numerous other possibilities to explore with FPMS 2.0, which will be investigated in future work. With the next coming prototype of the FPMS 2.0, we hope to be able to demonstrate a truly reconfigurable device that accomplish more than half a dozen of microwave analog functions and the possibility to tune their frequency behavior with an optimization assisted software.

Perspectives

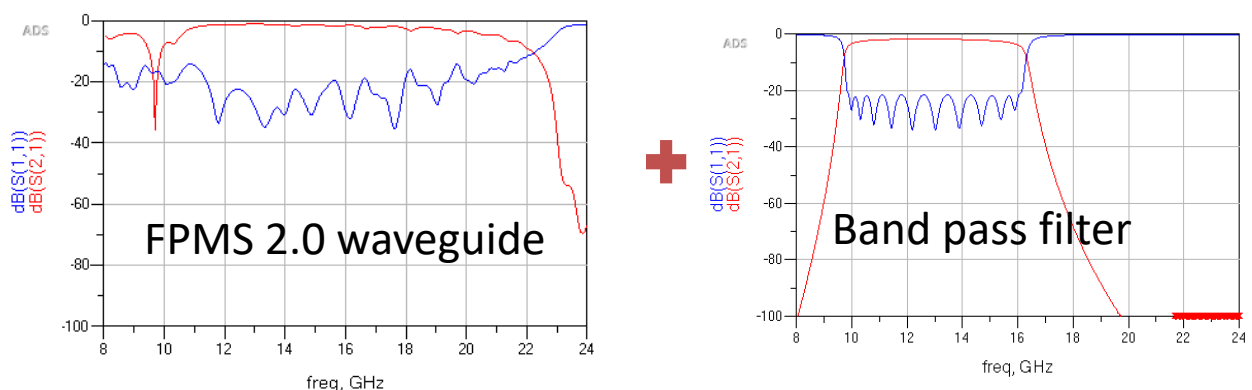
The main contribution of this thesis is to develop a reconfigurable device that is capable to perform multiple functions. There are several ways to improve the performance of these device. Some of them are as follows.

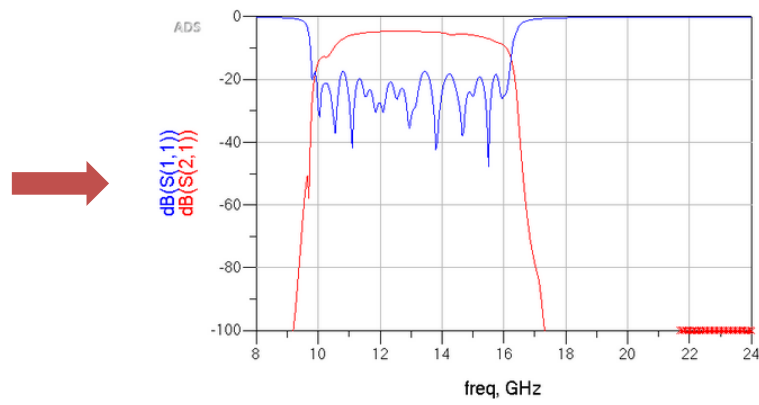
- **Short Term:**

The FPMS 2.0 board is currently under fabrication process. All the simulation results presented in Chapter 4 has to be measured on the actual board once it becomes available and the live optimization technique should be implemented on it to improve the performance of the device.

- **Medium Term:**

In the FPMS 2.0, different frequency bands can be useful for different function. We can also integrate a band pass filter in the same PCB for selection of operating band for better isolation. There is also a scope to include Artificial Intelligence in the optimization step as we can create huge database using FPMS.





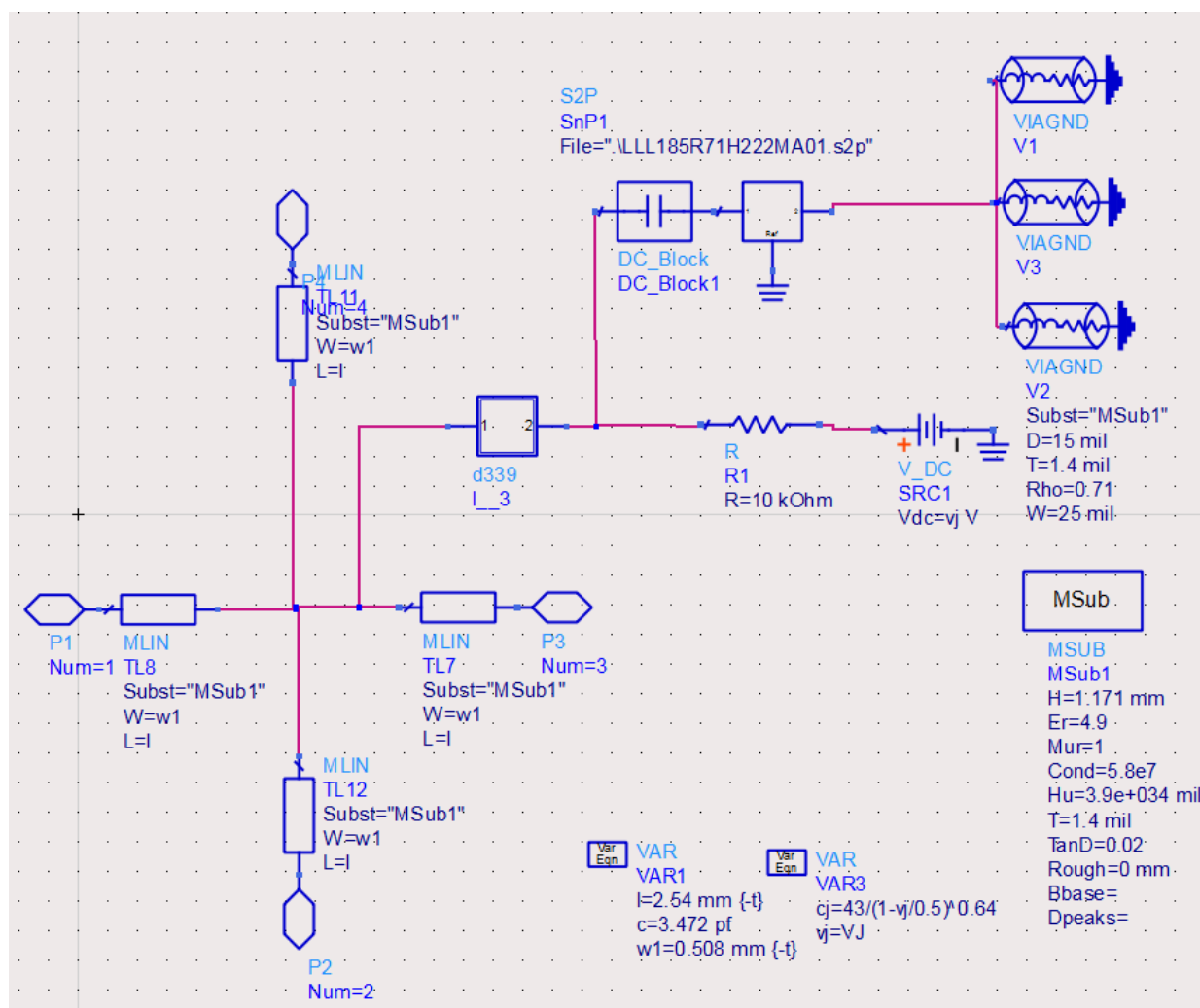
- **Long Term:**

To further improve the performances and for higher frequency band, we have to move to the 3rd generation of FPMS with no longer surface mounted varactors but every component should be embedded within the circuit. It can also have an embedded amplifier for better losses.

Appendices

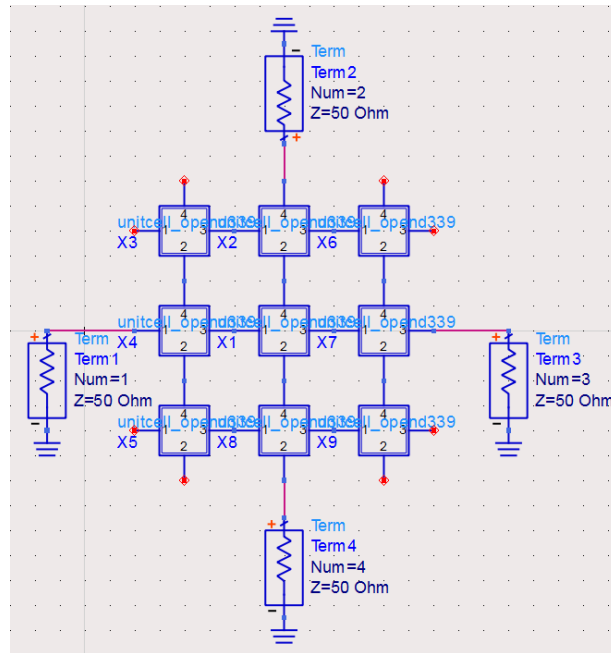
Appendix 1. ADS Equivalent Model of FPMS Unit Cell	141
Appendix 2. Netlist.log File Description.....	142
Appendix 3. MATLAB Graphical Interface	144
Appendix 4. Switch using FPMS 2.0	147
Appendix 5. ADS Schematic of unit cell of FPMS 2.0.....	149

Appendix 1. ADS Equivalent Model of FPMS Unit Cell



ADS Schematic of Unit cell

Appendix 2. Netlist.log File Description



3x3 Matrix of FPMS Unit Cells

```
Options ResourceUsage=yes UseNutmegFormat=no EnableOptim=no
TopDesignName="layout_lib:cell_3:schematic" DcopOutputNodeVoltages=yes
DcopOutputPinCurrents=yes DcopOutputAllSweepPoints=no DcopOutputDcopType=0
```

```
define d339 ( N__5 N__3 )
```

```
;parameters
```

```
L:L1 N__5 N__6 L=0.67 nH Noise=yes
```

```
L:L2 N__6 N__2 L=0.55 nH Noise=yes
```

```
L:L3 N__7 N__3 L=0.55 nH Noise=yes
```

```
C:C1 N__6 N__7 C=110 fF
```

```
"d1":DIODE1 N__2 N__7 Mode=1 Noise=yes
```

```
model d1 Diode Is=2.82 pA Rs=1.8 Ohm N=1.407 Tt=120 nsec Cjo=12.19 pF
Vj=38.53 M=12.6 Fc=0.5 Bv=32 Ibv=5 uA AllowScaling=0 Tnom=27 Xti=3 Eg=1.16
```

```
end d339
```

```
define unitcell_opend339 ( P1 P2 P3 P4 )
```

```
parameters VJ=0
```

```
V_Source:SRC1 N__10 0 Type="V_DC" Vdc=vj V SaveCurrent=1
```

```
d339:I__3 N__13 N__3
```

```
VIAGND:V1 N__17 Subst="MSub1" D=15 mil T=1.4 mil Rho=0.71 W=25 mil
```

```
R:R1 N__3 N__10 R=10 kOhm Noise=yes
```

```
VIAGND:V3 N__17 Subst="MSub1" D=15 mil T=1.4 mil Rho=0.71 W=25 mil
```

```
Short:DC_Block1 N__3 N__15 Mode=1
```

```

MLIN2:TL8 P1 N__13 Subst="MSub1" W=w1 L=1 Wall1=2.5e+028 mm Wall2=2.5e+028
mm Mod=1
MLIN2:TL7 N__13 P3 Subst="MSub1" W=w1 L=1 Wall1=2.5e+028 mm Wall2=2.5e+028
mm Mod=1
VIAGND:V2 N__17 Subst="MSub1" D=15 mil T=1.4 mil Rho=0.71 W=25 mil

cj=43/(1-vj/0.5)^0.64
vj=VJ

l=2.54 mm notune{ 1.27 mm to 3.81 mm by 0.05 mm }
c=3.472 pf
w1=0.508 mm notune{ 0.254 mm to 0.762 mm by 0.01 mm }
MLIN2:TL11 P4 N__13 Subst="MSub1" W=w1 L=1 Wall1=2.5e+028 mm
Wall2=2.5e+028 mm Mod=1
MLIN2:TL12 N__13 P2 Subst="MSub1" W=w1 L=1 Wall1=2.5e+028 mm
Wall2=2.5e+028 mm Mod=1
model MSub1 MSUB H=1.171 mm Er=4.9 Mur=1 Cond=5.8e7 Hu=3.9e+034 mil T=1.4
mil TanD=0.02 Rough=0 mm DielectricLossModel=1 FreqForEpsrTanD=1.0 GHz
LowFreqForTanD=1.0 kHz HighFreqForTanD=1.0 THz RoughnessModel=2
#uselib "ckt" , "S2P"
S2P:SnP1 N__15 N__17 0
File="U:\AAREFA\Model\layout_wrk\layout_wrk\data\LLL185R71H222MA01.s2p"
Type="touchstone" InterpMode="linear" InterpDom="" ExtrapMode="constant"
Temp=27.0 CheckPassivity=0
end unitcell_opend339
S_Param:SP1 CalcS=yes CalcY=no CalcZ=no GroupDelayAperture=1e-4
FreqConversion=no FreqConversionPort=1 StatusLevel=2 CalcNoise=no
SortNoise=0 BandwidthForNoise=1.0 Hz DevOpPtLevel=0 \
SweepVar="freq" SweepPlan="SP1_stim" OutputPlan="SP1_Output"

SweepPlan: SP1_stim Start=0.05 GHz Stop=5 GHz Step=0.01 GHz

OutputPlan:SP1_Output \
    Type="Output" \
    UseEquationNestLevel=yes \
    EquationNestLevel=2 \
    UseSavedEquationNestLevel=yes \
    SavedEquationNestLevel=2

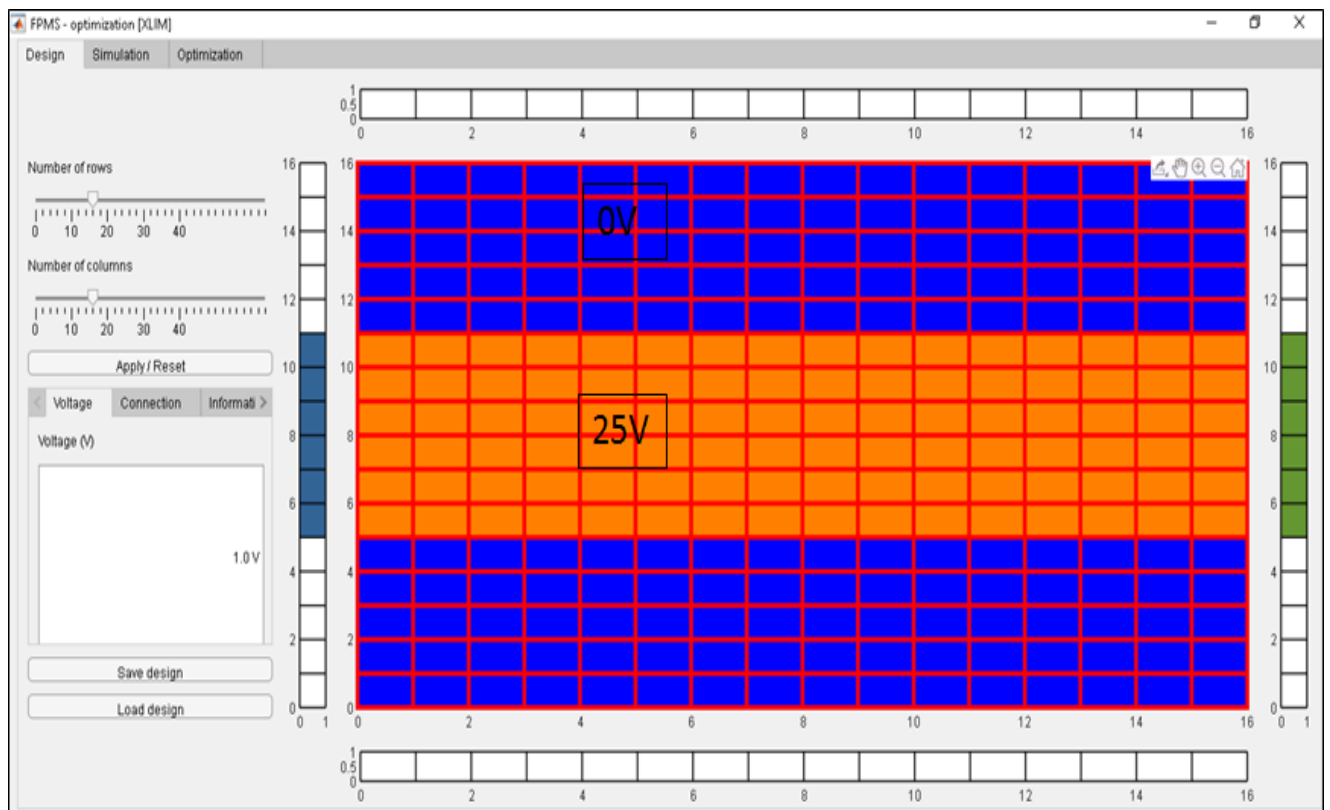
#load "python","LinearCollapse"
Component Module="LinearCollapse" Type="ModelExtractor"
NetworkRepresentation=2
Port:Term4 N__18 0 Num=4 Z=50 Ohm Noise=yes
Port:Term3 N__1 0 Num=3 Z=50 Ohm Noise=yes
Port:Term1 N__21 0 Num=1 Z=50 Ohm Noise=yes
Port:Term2 N__3 0 Num=2 Z=50 Ohm Noise=yes

unitcell_opend339:X1 N__25 N__11 N__10 N__8 VJ=V3
unitcell_opend339:X8 N__22 N__18 N__14 N__11 VJ=V1
unitcell_opend339:X7 N__10 N__15 N__1 N__17 VJ=V4
unitcell_opend339:X9 N__14 N__19 N__2 N__15 VJ=V1
unitcell_opend339:X2 N__28 N__8 N__27 N__3 VJ=V1
unitcell_opend339:X4 N__21 N__23 N__25 N__26 VJ=V2
unitcell_opend339:X5 N__6 N__0 N__22 N__23 VJ=V1
unitcell_opend339:X3 N__20 N__26 N__28 N__5 VJ=V1
unitcell_opend339:X6 N__27 N__17 N__4 N__7 VJ=V1

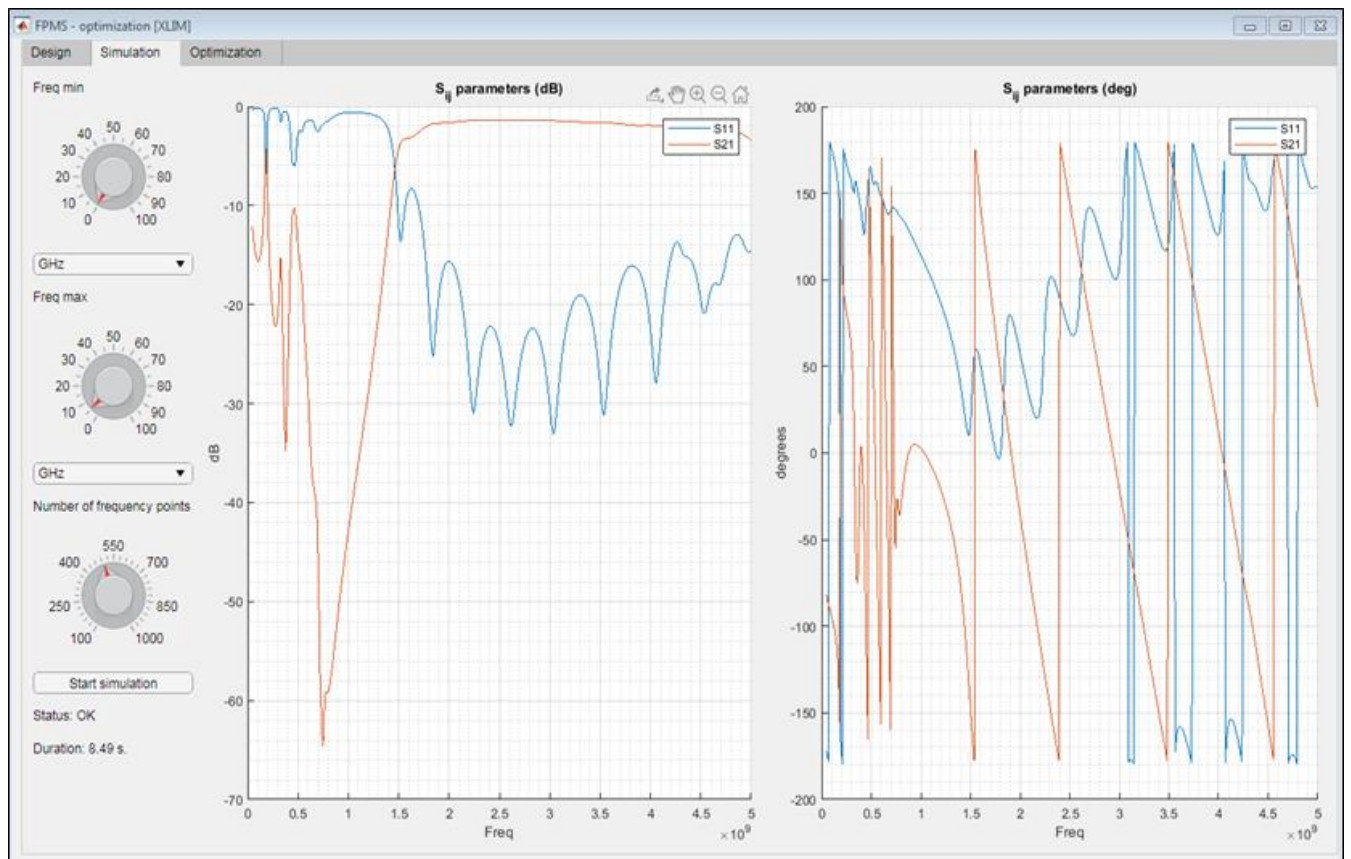
V1=0 tune{ 0 to 25 by 0.2 } noopt{ 0 to 25 }
V2=15 tune{ 0 to 25 by 0.2 } noopt{ 0 to 25 }
V3=25 tune{ 0 to 25 by 0.2 } noopt{ 0 to 25 }

```

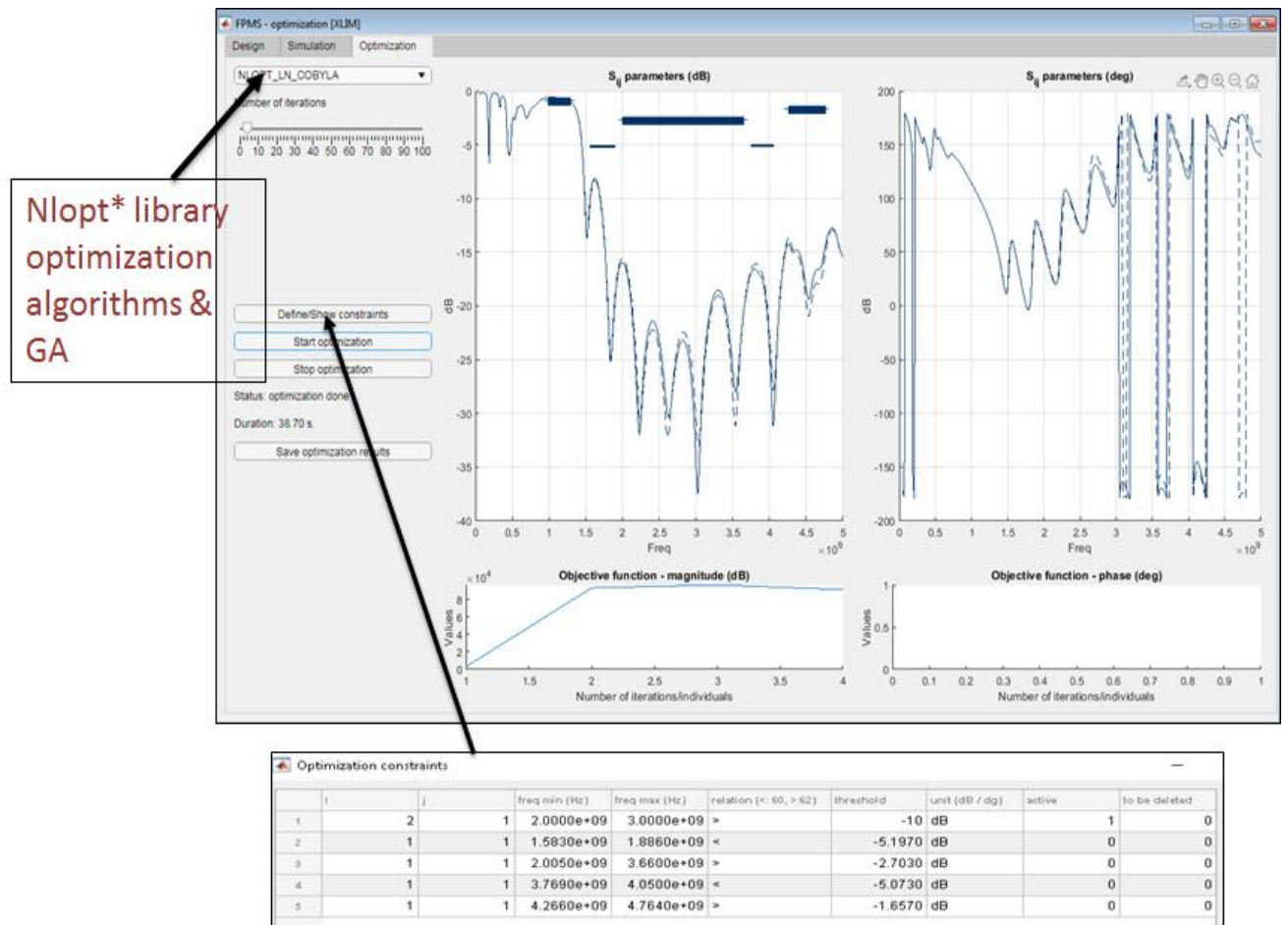
Appendix 3. MATLAB Graphical Interface



Design Panel



Simulation/ Measurement Panel

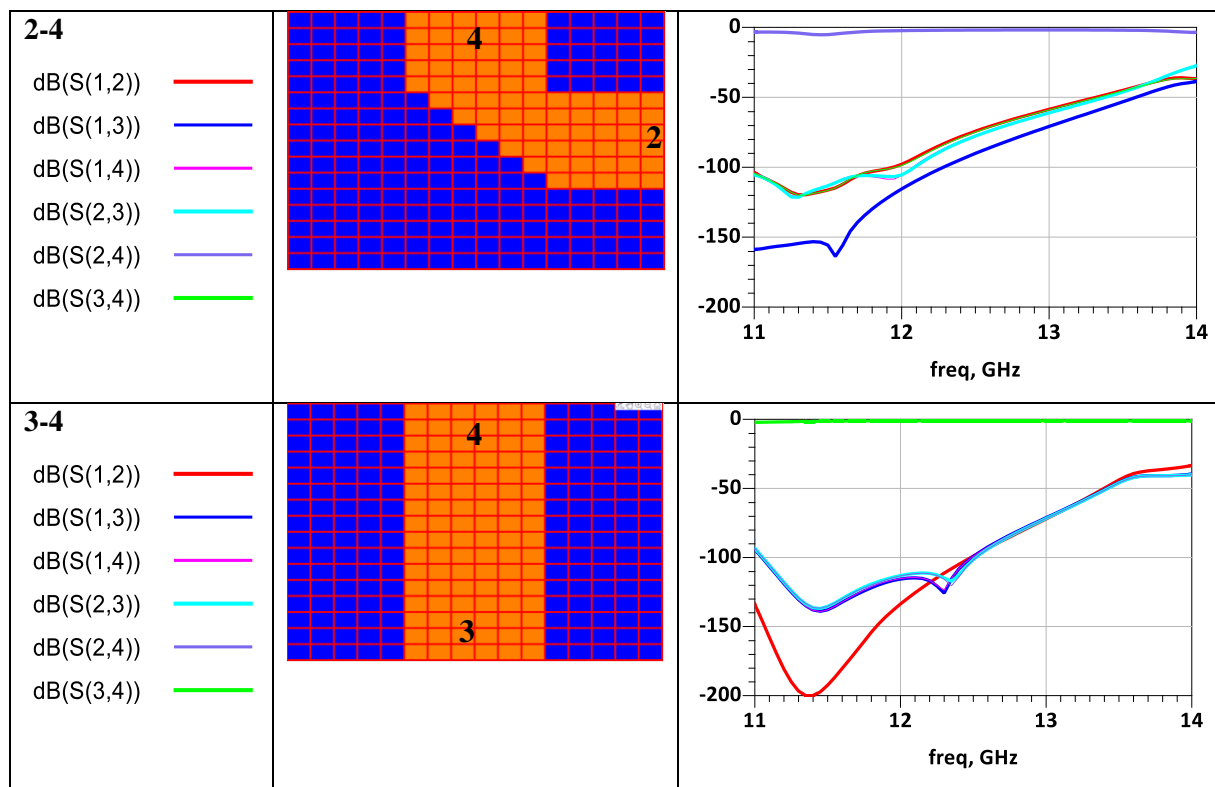


Optimization panel

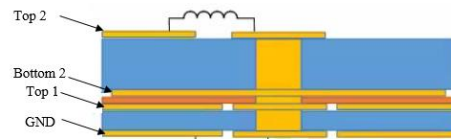
Appendix 4. Switch using FPMS 2.0

Table : Switch configuration and simulated S-parameters

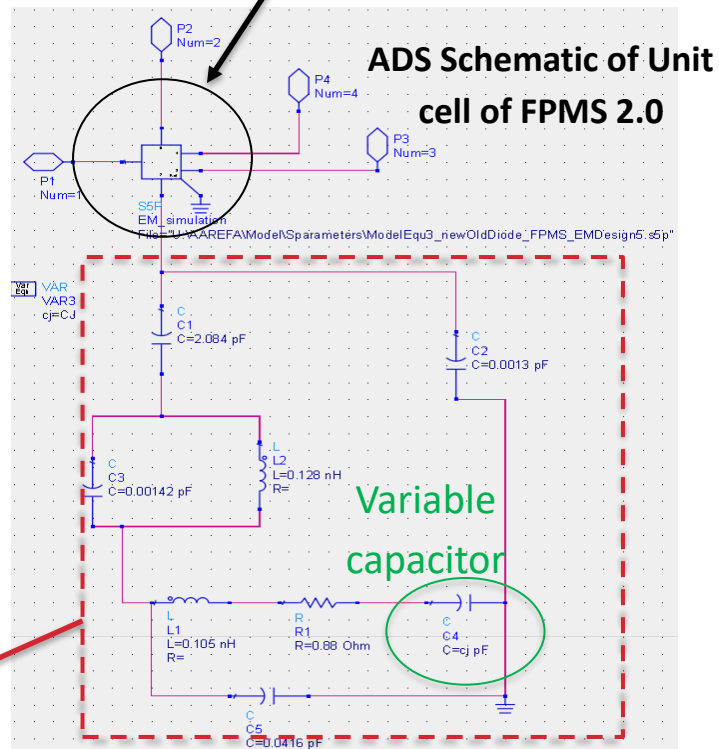
Port Connected	Configuration	S-parameters
1-2 dB(S(1,2)) — red dB(S(1,3)) — blue dB(S(1,4)) — magenta dB(S(2,3)) — cyan dB(S(2,4)) — purple dB(S(3,4)) — green		
1-3 dB(S(1,2)) — red dB(S(1,3)) — blue dB(S(1,4)) — magenta dB(S(2,3)) — cyan dB(S(2,4)) — purple dB(S(3,4)) — green		
1-4 dB(S(1,2)) — red dB(S(1,3)) — blue dB(S(1,4)) — magenta dB(S(2,3)) — cyan dB(S(2,4)) — purple dB(S(3,4)) — green		
2-3 dB(S(1,2)) — red dB(S(1,3)) — blue dB(S(1,4)) — magenta dB(S(2,3)) — cyan dB(S(2,4)) — purple dB(S(3,4)) — green		



Appendix 5. ADS Schematic of Unit cell of FPMS 2.0



CST EM simulation of
parallel plate



Composants Micro-ondes Accordables utilisant la technologie Field Programmable Microwave Substrate

Le substrat hyperfréquence programmable (Field Programmable Microwave Substrate - FPMS) a été utilisé dans cette thèse pour réaliser différentes fonctions hyperfréquences à partir d'une seule carte matérielle. Le FPMS est constitué de petites cellules unitaires, dont la constante diélectrique peut être modifiée de valeurs positives à négatives par l'application d'une tension de polarisation. Différents composants reconfigurables mis en œuvre à l'aide du FPMS, tels que un diviseur de puissance, un déphaseur, un atténuateur, etc. sont démontrés. En outre, une technique d'optimisation en direct est développée pour améliorer les performances de ces dispositifs avec le FPMS. La prochaine génération de FPMS 2.0 a été proposée dans le but de réduire les pertes et de régler individuellement chaque cellule le composant. Les tests préliminaires prouvent que le FPMS 2.0 a un grand potentiel en tant que dispositif reconfigurable qui peut exécuter ou combiner plusieurs fonctions micro-ondes à la fois.

Mots-clés : Field Programmable Microwave Substrate (FPMS), reconfigurable devices, optimization

Reconfigurable Microwave Components made using Field Programmable Microwave Substrate

The Field Programmable Microwave Substrate (FPMS) has been used in this thesis to realize different microwave functions from a single hardware board. FPMS has been made up of small unit cells, the dielectric constant of which can be changed from positive to negative values by applying a biasing voltage. Different reconfigurable components implemented using FPMS such as power divider, phase shifter, attenuator etc. are demonstrated. Moreover, live optimization technique is developed to reach the best performance of these devices possible with the FPMS. The next generation FPMS 2.0 has been proposed with the objective to reduce losses and individual tuning of each unit cell. The early stage tests proves that the FPMS 2.0 has a great potential as reconfigurable device that can perform or combine several microwave functions.

Keywords: Field Programmable Microwave Substrate (FPMS), reconfigurable devices, optimization

